Dynamics and Self-organization of Crowded Active Systems

Dissertation

For the award of the degree

""Doctor of Philosophy""

of the University of Göttingen

within the doctoral program

in physics

of the Georg-August University School of Science (GAUSS)

by

Leila Abbaspour

from

Maku, Iran

Göttingen, 2021

Thesis Committee

Members of the Examination Board

"Nobody ever figures out what life is all about, and it doesn't matter. Explore the world. Nearly everything is really interesting if you go into it deeply enough."

— Richard P. Feynman.

This thesis is dedicated to my dear Amir and my beloved parents Firouzeh and Ali to their endless love, support and encouragement.

Abstract

The perplexing and intriguing world of biological systems has inaugurated a new research field in statistical physics: out-of-equilibrium systems, known as *active matter* that mimic systems in the biological world around us from a statistical mechanical point of view. These systems exhibit captivating collective dynamics such as self-sustained pattern formation. Self-organization of motors and microtubules within the cell, swarming colonies of bacteria, and starling murmuration are some fascinating patterns in nature that organize themselves independently, without external control. Numerous computational, theoretical, and experimental models have been developed to unravel the physics of active matter system.

In this thesis, we employ several agent-based minimal models to study self-propelled particles to explore the key parameters that play a significant role in their dynamics and self-organization.

We develop a hexagonal lattice model to study the dynamics of passive "tracers" in the presence of active crowders where the tracer is pushed by the active particles, which leads to enhanced diffusion. We show that the degree to which this diffusion is enhanced depends crucially on the activity and the density of the crowders. Furthermore, we show that a decrease in the diffusion coefficient of passive particles is an explicit consequence of the local accumulation of active crowders in the system.

We employ Brownian dynamics simulation for spherical particles in continuous space to explore the strong velocity correlation in a mixture of active and passive

particles in the absence of explicit alignment interaction. We decouple the effect caused by a high density of the medium from the one caused by the persistent activity of the self-propelled particles and show that a dopant of active particles can produce a strong velocity correlation in a sufficiently dense system of passive particles.

We extend Brownian dynamics simulation to long, semiflexible active filaments to explore the various dynamical states in the system. We show that the self-propulsion force and the bending stiffness are two indispensable parameters in the systems that control the size and shape of the emergent clusters and the dynamical steady states in the system. Moreover, we add a direction reversal mechanism to the polymers to mimic the stochastic direction switching motion of filaments. The stochastic direction reversal rate is the third crucial parameter that controls the emergence of clusters and spirals in the system and provides an additional mechanism to either unwind spirals or to resolve clusters.

We employ our overdamped Brownian dynamic simulation to study the self-buckling of an individual active filament to infer essential parameters for studying the pattern formation of colonies of filamentous *Cyanobacteria* in the next chapter. We confirm that a critical length of *Cyanobacteria* is required for self-buckling which is in perfect agreement with the theoretical model that was developed recently in Dr. S. Karpitschka's lab.

Finally, by using inferred parameters from our self-buckling simulation, we investigate the pattern formation of filamentous *Cyanobacteria* at high density. Using the critical length from the self-buckling study as well as a length below and above this critical length, the polar and nematic long-range order in the system is investigated. The active filaments without stochastic direction reversal show a longer-range polar and nematic order in the system. We then incorporate the direction reversal mechanism: Increasing the reversal rate decreases the polar order in the system, but simultaneously

increases the nematic order. Remarkably, the critical aspect ratio for the given reversal rates exhibits the strongest polar order in the tangential direction of the filament and the strongest nematic order in both normal and tangential directions of the filaments.

.

Table of contents

Chapter 1

Introduction

1.1 Active Matter

Active matter system is of a novel class of soft matters that has drawn a lot of interest in recent years. Active matter is ubiquitous in nature across many scales: cytoskeletal filaments [1–3], motile cells [4–6], fish schools [5], and bird flocks [7–9]. These systems are inherently out of equilibrium and consist of a large number of active "agents", each of which continuously and autonomously harvests energy (from within their own body or from their surroundings) to fuel their systematic movement. One fundamental difference between these kinds of systems and driven systems (*i.e.* granular matter, sheared complex fluids, etc.) is that for active matter systems both driving and dissipation occur at the level of the constituent particles, whereas for driven systems the dissipation happens at the scale of the constituents but driving is implemented at the scale of the whole system, in most cases through the boundaries.

Active materials have exotic characteristics that make them fundamentally different from the everyday materials we deal with: fabric, plastics, liquids, metals, and glasses etc. For example, they can execute tasks such as self-motility [10–12], self-organization [2, 10, 12], and self-healing [13, 14] to name a few.
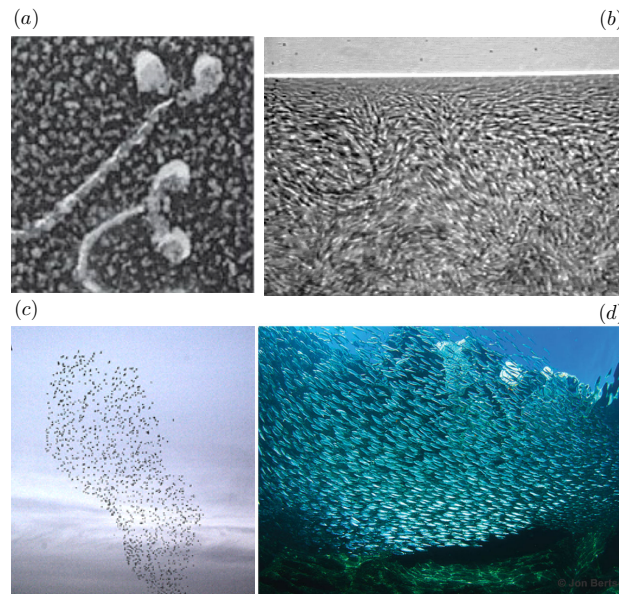
Figure 1.1 – *(a) High-resolution electron microscopy of Myosin taken from [26] (b) Bacterial "turbulence" in a sessile drop of Bacillus subtilis viewed from below through the bottom of a petri dish taken from [6] (d) Image of a sardine school showing some polar order taken from [10] (c) Photographs of starlings taken from [8]*

Beyond biological systems, active matter has also been a source of inspiration for artificial systems. Scientists have made great efforts to develop artificial systems that can adapt and mimic the dynamical properties of biological active materials, for instance, engineered synthetic colloids which are capable of converting energy into motion [15, 16] like a bacterium or phoretic microswimmers [17–19] that have proven to be essential for some systems [20] . Apart from the material design aspect, these artificial systems are poised to transform material science by designing micro- and nano-machines capable of autonomous movement, using the energy sources in the environment to mimic the capabilities of living organisms [21, 22]. In addition, artificial swimmers have been associated with a wide range of practical applications, ranging from drug delivery [23], cancer therapy [24] to soil remediation [25]. Now, to have a better understanding of these kinds of out-of-equilibrium soft matter systems we will categorize them into different classes in the next section.

1.2 Classification of Active Matter

There are different approaches of categorizing active matter systems into sub-classes. The two most commonly used ones, based on fundamental principles of physics, are the classification of active matter systems considering (a) conservation laws of the dynamics and (b) the geometry of the constituent particles. Here we describe them with appropriate details.

1.2.1 Classification based on conservation laws

In this subsection, we divide the active matter systems into two different sub-classes by considering the conservation of momentum, and for this, friction will be the most relevant factor. The sub-classes are termed as (a) wet and (b) dry. In general, a given active material lies between these limiting cases (a) and (b) with the relative magnitudes of frictional and dissipative damping controlling its position in the wet-dry spectrum. Hence, just using friction, one would be able to differentiate and categorize between these two sub-classes.

1.2.1.1 Wet active matter

Typically, wet active systems are embedded in an ambient fluid (which dampens the active system through viscous friction) and the constituent particles can interact via the ambient fluid *i.e.* through *hydrodynamic* interaction. Therefore, if solvent-mediated hydrodynamic interactions are important in a given active system it is characterized as wet active matter. In this case, the dynamics of the suspending fluid must be included in the model, and a description of the suspension of active particles and the surrounding fluid must be developed together while preserving the overall momentum. For instance, while considering the physics of micro-swimmers in bulk fluid, the hydrodynamic flow fields generated by the microswimmers should be taken into account as well as damping

effect of the surrounding fluid on the relative motion of the neighboring particles. Hence, the total momentum (which is the sum of the momentum of the constituent particles and the ambient fluid) of the system is conserved.

Inclusion of the description of the surrounding fluid is not a simple extension. In most cases, the introduction of the fluid description and the coupling of the density and orientational degrees of freedom of the active particles to the fluid flow lead to complex spatio-temporal dynamics. Typically, the hydrodynamic interactions are long-ranged and combining them with the incompressibility of the fluid fundamentally changes the physics of the problem and causes the appearance of turbulence-like vortical structures [10, 27, 28] and topological defects [10, 29–31].

However, there are also many active materials that have alternative forms of dissipation, such as wall friction which is the friction between the active particles and a substrate without the above-mentioned complexity, as will be discussed in the next sub-section.

1.2.1.2 Dry active matter

In systems where active materials are in contact with a substrate, or are confined between two closely spaced walls, or move through a porous medium, the drag force due to the friction of the substrate outweighs the friction due to the ambient fluid (if there is any). This is a consequence of the coupling and decoupling of the components of the system to the confining medium. The momentum of the active system is not conserved and the substrate acts as a momentum sink.

The reason to ignore the aspect of the conservation of momentum is typically the fact that hydrodynamic interactions are of less importance in such systems. The suppression of hydrodynamic interactions can be due to several effects, such as fluctuations, volume exclusion, and other short-range interactions. Examples of systems that lie in the dry

spectrum include the Vicsek model for mimicking migrating animal herds [32] and assemblies of vibrating granular rods [33–35]. In this thesis, all works were performed in different types of dry systems.

1.2.2 Classification based on the geometry of the constituent particles
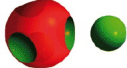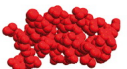
	symmetry	convex particles		non-convex particles	
isotropic	full symmetry	spheres			
uniaxial apolar	rotational symmetry around axis $\hat{u}$	rods	platelets	dumbbells	rings
uniaxial polar		Janus particles	cones	pears	bowls
biaxial	discrete rotational or inflection symmetry	cubes / tetrahedra polyhedra		trimers / chiral particles special colloidal molecules	
		boards / pyramides		tetrapods octapods multipods	stars
		regular patchy particles		lock-and-key particles	
	no symmetry	irregular patchy particles		general colloidal molecules	

Figure 1.2 – *Classification of colloidal particles with respect to their shape, image is taken from [36]*

Another popular way of classifying active matter systems is based on the shape of the constituent particles [36]. It is quite known that the shape of the particles strongly influences their motion and the formation of a pattern by a group of such particles.

Both biological and artificial self-propelled particles often have a significant shape asymmetry and they can give rise to a variety of new phenomena due to this shape symmetry/ asymmetry (see figure. 1.2). We therefore classify active systems based on their geometry, isotropic or anisotropic.

1.2.2.1   Isotropic

The simplest and at the same time completely symmetrical, *i.e.*, isotropic, shape is that of a sphere. This is the typical form for colloids studied in both experimental [37, 38] and theoretical [17, 18, 39, 40] soft matter physics because firstly, they are easy to make and, secondly, due to the lack of 'shape' degrees of freedom, their behavior are relatively easy to model and understand. Spheres have only translational degrees of freedom, hence, they can only form perfectly isotropic state and the crystalline state [41]. Note that, the self-propelled sphere still has an orientation, but in this case the activity is responsible for the anisotropy, not the geometry of the particles. In chapters 2 and 3, the geometric shape of the active or passive particles is isotropic.

1.2.2.2   Anisotropic

Anisotropic particles have a non-spherical structure and are typically, either *uniaxial* or *biaxial.* They exhibit very different static and dynamical behavior than the spherical particles.

- **uniaxial** particles have an axis of symmetry denoted by a unit vector $\hat{u}$. They have rotational symmetry with respect to $\hat{u}$ and this is the only degree of freedom of their orientation in two spatial dimensions. Moreover, uniaxial particles can be divided into polar and apolar particles. Polar particles have head-tail symmetry, otherwise they are called apolar. A good example of the simplest anisotropic particles are rod-shaped particles [42, 43], which are an excellent model system

for studying liquid crystals [44] and polymer systems [45–47]. In this thesis, we used a rod-shaped model in Chapters 4 and 5 to mimic the dynamics of bacteria and study their dynamical steady-state and self-organization with and without external cues.

- **biaxial** particles either have discreet symmetries or no symmetry. Unlike uniaxial particles, here we can no longer describe their orientational degrees of freedom with a unit vector. Instead, we must use two perpendicular unit vectors or Euler angles [48]. Examples are: Cube [49], Tetrahedron [50], etc (see figure. 1.2).

1.3 Modeling Active Matter Systems

Being diverse and complex, active matter systems pose a real challenge in terms of modeling them using simple models. In this section, we focus on such modeling approaches of active matter systems and give an overview of the main features of different existing models. We also elaborate on where they are applicable/not applicable. As mentioned before, there are several methodological approaches to describe active matter. For a pedagogical discussion, we divide the possible descriptions into two categories: (a) particulate or agent-based models (b) hydrodynamic or continuum models.

1.3.1 Agent-based models

In the agent-based modeling approach, one seeks to understand the macroscopic dynamical or mechanical properties of the system based on the interactions at the level of the constituent elementary objects (known as 'agent'). For example, while modeling a polar active fluid using such an agent-based approach, the agents/particles are typically considered as self-propelled entities moving at a certain speed along

a body-fixed orientation (polarity axis), also undergoing rotational diffusion. The interaction between the agents can be steric, aligning, etc., based on the target system one seeks to mimic. This can include Weeks-Chandler-Andersen [51](WCA) or similar soft repulsive contact interaction, which results in the explicit alignment of the polarity axes (of both polar and nematic type). The equations for describing such agent-based models can be in discrete space and time (lattice-based model) [39, 52, 53] or in a continuous space-time domain (which is also discretized for the purpose of numerical integration) [54, 55]. In Chapter 2, we discuss a lattice-based model and in chapters 3-6 we will use continuum models.

The prototypical example of the agent-based approach is the case of active Brownian particles or ABP which has been developed to understand the collective behavior of active colloids or self-propelled microbes. Below, we briefly discuss the salient features of the ABP model.

Active Brownian particles (ABP) have served as phenomenological models for studying the motion of self-propelled agents. Such agents in a biological context, *e.g.* bacteria or other microbes, absorb chemical energy from the environment or from within its own body and convert it into persistent motion to perform tasks necessary for their survival. Now, in the ABP model, this self-propulsion or persistent motion is modelled via a propulsion velocity v_0 with constant magnitude and a direction that diffuses over time. For simplicity the frictional damping is modelled as $-\gamma\mathbf{v}$, where $\mathbf{v}$ is the velocity of the particle. The equation of motion can be written using the Langevin approach as,

$$m\ddot{\mathbf{r}} = -\gamma\mathbf{v} + \sqrt{2D}\boldsymbol{\zeta}(t) + f_0\hat{\mathbf{n}} \qquad (1.1)$$

where $\boldsymbol{\zeta}(t)$ is a vectorial Gaussian white noise with $\langle\zeta_i(t)\zeta_j(t')\rangle = \delta(t - t')\delta_{ij}$ and $D = k_B T/\gamma$ (using Einstein relation, in which k_B is the Boltzmann constant and

T is the temperature). Note that the first two terms are used for representing the friction and noise for a standard Brownian particle. The third term represents a propulsion force in $2d$, with a constant magnitude f_0 and a direction along which the propulsion acts. $\hat{\mathbf{n}}$ can be represented as $(\cos(\theta), \sin(\theta))$ where θ is the angle along which propulsion works. The dynamics of this angle is modelled by simple rotational diffusion,

$$\dot{\theta} = \sqrt{2D_R}\eta(t) \tag{1.2}$$

where $\eta(t)$ is mean zero unit variance Gaussian white noise and D_R is the rotational diffusion coefficient. In the *overdamped* limit (ignoring inertia) one can rewrite the equation of motion as,

$$\mathbf{v} = \sqrt{2k_B T/\gamma}\boldsymbol{\zeta}(t) + v_0\hat{\mathbf{n}} \tag{1.3}$$

along with the Eq. 1.2 where $v_0 = \frac{f_0}{\gamma}$. We have used this model in Chapter 3 to describe the dynamics in a mixture of active and passive particles.

1.3.2 Hydrodynamics approach

A hydrodynamic approach provides a continuum description of an active or passive system in terms of the dynamics of the so-called slow variables, as these variables change gradually over in both space and time. Typical examples of slow variables in condensed matter systems are broken symmetry variables near the phase transition, and density of conserved quantities. Using this approach, one can derive a set of equations that describe the coarse-grained behavior of the slow variables of the system. This derivation can be derived in multiple ways: (i) by coarse-graining the corresponding microscopic dynamics, (ii) from conservation laws and symmetry principles. In the process of establishing a general set of equations for a continuum system, the first task

is to define a set of hydrodynamic variables. The general equations are based on an expansion of the aforementioned variables and their spatial derivatives, with the only constraint being the conservation laws and symmetries of the underlying microscopic dynamics.

There are numerous examples of such hydrodynamic descriptions of active matter. The two most famous examples in soft matter systems are the hydrodynamic theories for the dynamics of passive fluids and momentum non-conserving active fluids, which are known as the Navier-Stokes and Toner-Tu equations [56], respectively. For the former, the hydrodynamic variables are the density and the velocity field of fluid whereas for the latter, an additional polarity field of the active fluid is needed. These kinds of descriptions typically fail at length scales of the order of the particle size or smaller but are very useful to explore the behavior of the system at large length and time scales.

1.4   Collective Behaviour

Active systems are idealized systems studied to better understand the mechanism behind the collective behavior seen in various biological systems. Examples of collective behavior in living active matter systems range from mammalian herds to flocking of birds, and to pattern formation in bacterial colonies, which all stem from the far-from-equilibrium dynamics and the complex interactions between the constituents. These examples show that this type of collective behavior can be observed at the micron-scale as in bacterial swarms as well as at over kilometers in animal herd. Similarly, their timescale can also vary from microseconds to days. Note that this kind of ordered dynamic structure or patterns forms in noisy environments and most importantly without leaders or external fields that dictate any behavior.

In active systems, there are two predominant types of collective behavior. It has

been found that motile creatures usually congregate and form flocks to exhibit swarming behavior. Examples include swarm behavior in birds, tetrapods, and fish. Or, they may simply accumulate where they move more slowly. At high densities, they may also slow down for biochemical or steric reasons, leading to motility-induced phase separation (MIPS) between dense and dilute phases.

The simplest single-particle-level model that elicits collective behavior of flocking is the Vicsek model, proposed by Vicsek *et al.* [32, 57], which introduces an explicit polar interaction among motile entities. In contrast, motility-induced phase separation results in clustering without explicit alignment interaction and is due only to the high density of the motile entities. We will elaborate on these two collective behaviors and discuss how they emerge with and without explicit alignment interaction, in the next subsections.

1.4.1 Physics of clustering: motility-induced phase separation

One of the indispensable ingredients that make matter "active" is its motility. A prototypical example of active matter is therefore just a collection of self-propelled particles. Motility in these systems leads to a number of nontrivial physical phenomena which have no equivalent in a passive counterpart. One of the fascinating phenomena recently discovered is motility-induced phase separation which refers to the spontaneous phase separation in the system that arises due to the self-trapping of self-propelled particles when both their density and motility are high enough.

To understand this phenomenon, one can assume a population of swimmers in d dimensions, running for a time τ with velocity v between two successive tumbles. The hydrodynamic equation for a population of run and tumble swimmers can be written as [11, 58] :
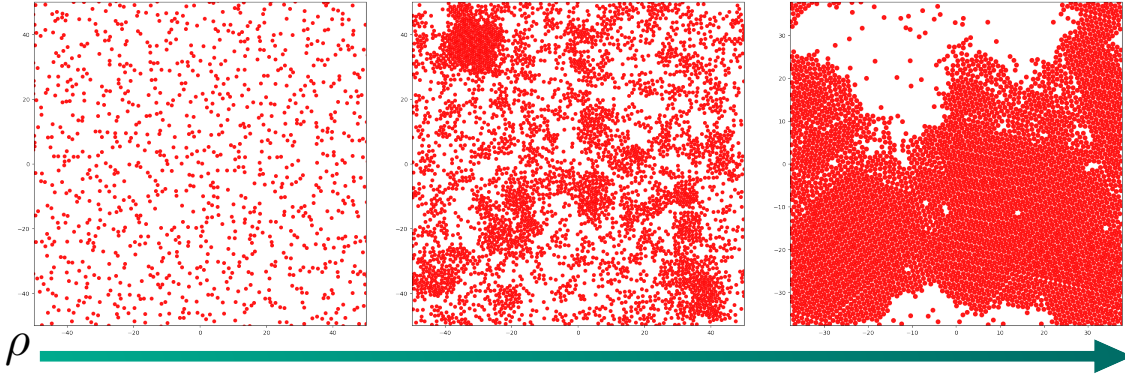
Figure 1.3 – *With increasing density, the velocity of the active particles slows down due to self-trapping and phase separation occurs in the system.*

$$\partial_t \rho = \frac{v^2 \tau}{d} \nabla^2 \rho = D_{\text{eff}} \nabla^2 \rho \tag{1.4}$$

where ρ is the density field and $D_{\text{eff}} = \frac{v^2 \tau}{d}$. Note that the velocity of the swimmer is considered to be constant in this particular case. In the situation where velocity can vary in space or $v = v(\mathbf{x})$, we can rewrite 1.4 as [11]

$$\partial_t \rho = \frac{\tau}{d} \nabla . [v \nabla (\rho v)]. \tag{1.5}$$

This equation is the most crucial one to understand the physics of self-trapping and has some notable aspects. Solving this for steady-state ($\partial_t \rho = 0$), we get $\rho = \frac{1}{v(\mathbf{x})}$, which means that the self-propelled particles accumulate (*i.e.* the density is higher) where they move more slowly, as one can see in figure. 1.3, with increasing density phase separation occurs in the system. This is an important feature of interacting active Brownian particles which has no counterpart in a passive system and leads to so-called motility induced phase separation (MIPS). Note that this phase separation is a consequence of no-equilibrium dynamics and does not arise from attractive interaction.

MIPS implies a persistent heterogeneity in the density of self-propelled particles and it can develop spontaneously when the effective velocity of the active particles goes

down due to the increased density of particles in the system. In Chapter 2, we will show how the active particles affect the dynamics of the passive particles in a mixed system and how this emergent heterogeneity can in turn affect the effective diffusion coefficient of passive particles.

The orientation of the self-propulsion forcing of these self-trapped particles in the clusters is completely random as this clustering occurs without an explicit alignment interaction in the system. However, recently Caprini *et al.* [59] and Henkes *et al.* [60] have shown that MIPS is accompanied by a spontaneous alignment of the velocity of the particles in the dense phase of an active solid system. In addition, Szamel *et al.* [61] reported a strong velocity correlation (only parallel to the velocity) of self-propelled particles at high density of an active fluid system as well. They found that the average size of domains with aligned velocities grows with the square root of the persistence time of the self-propulsion force. In Chapter 3, we generalize this idea to a mixture of active and passive particles instead of a purely active system. We also answer the question of whether we can obtain such a strong velocity correlation in a dense passive system by doping it with a small fraction of active particles.

As mentioned earlier, during MIPS, clusters form without explicit alignment interaction and this mechanism helps us to capture the collective behavior in living or artificial active matter, such as colonies of bacteria or active Janus colloids. Outside the domain of such examples, there is a huge class of active matter with explicit alignment interactions between the agents, such as in flocks of birds or fish schools. In order to understand their collective behavior, one must define an explicit alignment interaction between the propulsion forces acting on each active particle. The most famous model for studying such a system is the Vicsek model [32], which we will discuss in more detail in the next subsection.

1.4.2   Physics of flocks: The Vicsek model

An important ingredient for the formation of swarms is a mechanism for alignment of the constituent particles or agents, usually with respect to the direction of neighbors. As mentioned before, the canonical model that introduces such explicit alignment among self-propelled particles is the *Vicsek model*, which provides a model for the swarming of self-motile particles.
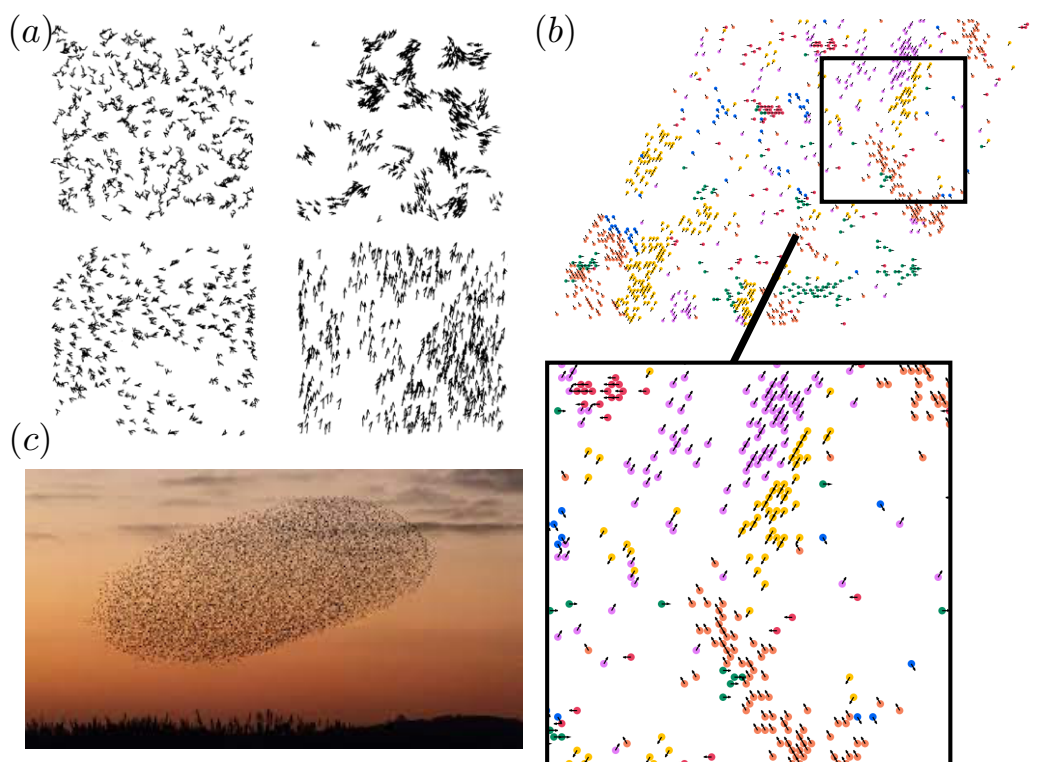
Figure 1.4 – *Panel (a) Different patterns of collective movement generated by the classic Vicsek model (The image is taken form [32]). Panel (b) The Vicsek model is implemented in a hexagonal lattice model (different colors show the direction of the active particles in a hexagonal lattice) Panel(c) Flocking of birds*

The original version of the Vicsek model [32] was defined in two dimensions, and was based on the following set of rules. Each self-motile entity in the system is described as a point-particle (no exclusion or steric interaction) with a direction θ_i at time t; the self-motile entity moves along this direction with velocity v_0 with a discrete time step

of size $\Delta t = 1$. At each time step and for each particle i, there is an alignment rule that applies to the particles as follows: (i) In the first step, one calculates the average direction of all particles inside a circle of radius r whose center is the particle position $r_i(t)$; (ii) then the direction of particle θ_i is set equal to the angle corresponding to this average direction, and in addition, some noise is added playing the role of rotational diffusion. It stochastically changes the final direction of an angle $\Delta\theta$ by a randomly chosen value in $[-\eta, \eta], \eta \in [0, \pi]$.

At each time step Δt, the equation leading to such an explicit alignment updates the direction θ_i, the velocity $\mathbf{v_i}$, and the position $\mathbf{r_i}$ as follows:

$$\theta_i(t + \Delta t) = < \theta(t) >_r + \Delta\theta \tag{1.6}$$

$$\mathbf{v_i}(t + \Delta t) = (cos(\theta_i(t + \Delta t)), sin(\theta_i(t + \Delta t))) \tag{1.7}$$

$$\mathbf{r_i}(t + \Delta t) = \mathbf{r_i}(t) + \mathbf{v_i}(t + \Delta t)\Delta t. \tag{1.8}$$

where $\Delta\theta$ is the noise in the orientational dynamics of the system and plays the role of thermal fluctuation and $< \theta >_r$ denotes the average direction of the velocities of the particles inside a circle of radius r.

The Vicsek model has drawn the attention of many physicists in the field of statistical mechanics and condensed matter as this model is able to show a transition between order and disorder far from equilibrium, only by changing the noise strength η. If the strength of the noise is low, the particles tend to align their direction of motion (similar to the ferromagnetic phase seen in equilibrium below T_c), causing the system to enter into an ordered swarm state. With increasing η, on the other hand, the order decreases and after a point, the noise dominates and the particles move independently

of one other; at that high noise value, there is no swarm. The order parameter which can describe this out-of-equilibrium phase transition is defined as :

$$< |\mathbf{v}| > = \frac{|\sum_{i=1}^{N} e^{i\theta_i}|}{N} \rightarrow \begin{cases} 1, & \eta \rightarrow 0 \\ 0, & \eta \rightarrow 1. \end{cases} \qquad (1.9)$$

In the thermodynamic limit or $N \rightarrow \infty$, this shows a discontinuous transition. So in some respect, it is analogous to a first-order phase transition seen in equilibrium. In particular, near the criticality, the coexistence of two different phases is observed, which leads to the formation of bands or stripes moving perpendicular to its "axis" within a disordered background.

It is useful to remember that in a passive analog of the Vicsek model the particles (or the spins) within the system are not able to move and can only align, corresponding to the Vicsek model with $v = 0$. This model falls into the same universality class as the XY spin model, which has a Kosterlitz-Thouless phase transition due to the unbinding of topological defects without any symmetry-breaking transition from order to disorder. This is the so-called "Mermin-Wagner theorem", according to which spins with continuous symmetry, like the vectors of the XY model, can only undergo a transition from order to disorder in a spatial dimension $d > 2$. On the other hand, the Vicsek model can exhibit spontaneous symmetry breaking and an order-disorder transition in $d = 2$, as it is driven out of equilibrium by activity (self-propulsion). This means that if the system is out of equilibrium the Mermin-Wagner theorem can be violated and one can see a long-range order even in dimension less than or equal to two.

The Vicsek model introduces an explicit alignment interaction between particles that underpins the collective motion of active particles in the system. However, the alignment interaction can also be generated by the geometry of the particles in the

system rather than invoking them by hand. Elongated particles, such as active polymers, tend to align with each other as a result of collisions. When a binary collision occurs, momentum transfer increases in the longitudinal direction, causing the two elongated particles to align and move along each other. Depending on whether the collision is parallel or anti-parallel (head to head or head to tail), they may form a stable group of two, move together for a extended period of time, or just walk side by side until they lose contact with each other. The average cluster size grows over time as other active particles also can come and join them during additional collisions. There are many physical parameters that can hinder or facilitate the formation of clusters in the systems. Examples include the density of self-propelled rod-shaped particles, their bending stiffness, activity and aspect ratio [62].

In Chapter 4, we will discuss the formation of clusters at a low density of active filaments and examine the effects of physical parameters such as their bending stiffness, activity, and reversal rate. In Chapter 5, we extend the study to a dense system of active polymers to understand the collective behavior of filamentous bacteria observed in experiments with gliding cyanobacteria to shed light on their orientational order by varying the reversal rate, bending stiffness, and activity and compare the results with the experimental data. Hence in both chapters, we study and analyze collective behavior generated by activity and particle anisotropy, which results in aligning interactions with invoking explicit Vicsek like interactions.

1.5   Scope of this thesis

In this thesis, we perform a computational study of dense systems of active particles and their complex dynamics and self-organization. We start with studying the influence of active particles in a passive/active mixture and then we investigate the pattern formation dynamics in suspensions of elongated particles.

In **chapter 2**, we investigate the dynamics of passive tracers in an active system and also in a mixture of active and passive systems and show that the effective diffusion coefficient of passive tracers increases before the motility phase separation of active particles in the system and it diminished when the phase separation of active particles emerges in the system.

In **chapter 3**, we study the velocity correlation of a dense passive system in the presence of a small fraction of active particles (dopants). We show that a very small fraction of active particles is sufficient to demonstrate a strong velocity correlation in the system, as long as the density of the embedding passive medium is high enough. We finally analyze how the velocity correlation in the system is affected by activity parameters.

In **chapter 4**, we consider a system of active filaments at low density. We created a state diagram of the self-organization of active filaments by modulating the self-propulsive force and the bending stiffness of the filaments. Later, we added a reversal mechanism to the filament's driving direction to mimic the reversal seen in gliding cyanobacteria and study the state diagrams as a function of self-propelling force and bending stiffness for different reversal rates to understand the role of reversal.

In **chapter 5**, we performed simulations using flexible and self-propelled filaments to understand the physics of buckling and to determine the bending stiffness and activity of the bacteria. We also compared our results with the experimental observation for a system of gliding filamentous cyanobacteria. By incorporating the measured parameters in our non-equilibrium simulations we analyzed the pattern formation in the next chapter.

In **chapter 6**, we used the parameters from the comparison of buckling simulations and experiment, to explore the pattern formation observed in a dense colony of filamentous cyanobacteria. We demonstrate that there is a long-range nematic order

in the system. We also observe that the polar order of the filamentous cyanobacteria decreases with increasing reversal rate, which is their spontaneous response to the changes in light intensity.

In **chapter 7**, we summarize all the results presented in different chapters and put them in a bigger context of Self-organization in active matter. We then finish the thesis by discussing the future directions for this research and how current thesis can be used as a guide to this aim.

Chapter 2

Enhanced diffusion of a tracer particle in a lattice model of a crowded active system [1]

2.1 Abstract

Living systems at the sub-cellular, cellular, and multi-cellular level are often crowded systems that contain active particles. The active motion of these particles can also propel passive particles, which typically results in enhanced effective diffusion of the passive particles. Here we study the diffusion of a passive tracer particle in such a dense system of active crowders using a minimal lattice model incorporating particles pushing each other. We show that the model exhibits several regimes of motility and quantify the enhanced diffusion as a function of density and activity of the active crowders. Moreover, we demonstrate an interplay of tracer diffusion and clustering

---

[1]This chapter is based on a published paper , "Enhanced diffusion of a tracer particle in a lattice model of a crowded active system " by L. Abbaspour and S. Klumpp in **Physical Review E** 103, 052601, 2021. Author contributions: L. Abbaspour performed simulations, data analyses and wrote the manuscript, S. Klumpp supervised the project and wrote the manuscript.

of active particles, which suppresses the enhanced diffusion. Simulations of mixtures of passive and active crowders show that a rather small fraction of active particles is sufficient for the observation of enhanced diffusion.

2.2 Introduction

The behavior of individual particles within a crowded environment is influenced by the complex collective behavior of the surrounding particles [63–66]. Indeed, many biological systems are densely packed. Molecular systems in the cytoplasm of cells [63, 67], colonies of bacteria [4], bio-films [68], and tissues [69] are a few examples. Often, the crowded environment contains active particles that are driven out of equilibrium due to the local injection and dissipation of energy. On the molecular scale these active particles may be molecular motors pulling cargoes through cytoplasm and 'stirring it' [70–72] or enzymes exhibiting enhanced diffusion [18, 73], on the cellular scale, these could be self-propelled cells swimming in a suspension or moving through a tissue or a colony of cells [74, 75]. This means that detailed balance is not fulfilled in these systems, so they cannot be described by equilibrium statistical mechanics.

The observation of individual 'probe' or 'tracer' particles within such a system provides a method to quantify crowding effects as well as to probe for the degree of crowding if this is difficult to determine directly. Such probes include the diffusion of the tracer particle [76, 77] as well as specific chemical reactions or conformational changes such as the compaction of a polymer chain as measured by FRET-probes at the two ends of the polymer [78, 79].

Diffusion of molecules and particles in complex environments has been studied on a range of length scales and the complex environment can give rise to dynamic phenomena such as anomalous diffusion [80, 81]. Specifically, diffusion of a passive tracer particle in an active system has been studied in various experimental and theoretical model

systems. Notably, Wu and Libchaber [82] studied the trajectories of polystyrene beads in a suspension of swimming bacteria and observed enhanced diffusion of the beads. Such enhanced diffusion has been studied extensively, both theoretically [83–90] and experimentally [85, 91–97]. Extensions of the simplest system include 3 dimensional systems [96], the presence of obstacles [94] and confinement, and effective interaction between passive particles [98].

Interactions between particles in suspension can be complex and generally involve hydrodynamic interactions in addition to simple excluded volume and particle-particle collisions. Therefore, simplified minimal models systems can help to advance our understanding of the role of active processes. Both continuum models [54] and lattice models [52, 53] have been used for that purpose. Enhanced diffusion of a tracer in a crowded active system has been observed in models with and without hydrodynamic interactions [85, 99].

Specifically, lattice models provide a conceptually simple and often computationally inexpensive approach to study complex phenomena based on particle-particle interactions. In the case of active particle systems, lattice approaches have been used to study clustering and phase separation [87, 100–103]. Specifically, modifications of the dynamic rules can easily be implemented to investigate whether results are generic or specific to given dynamics.

Following this approach and applying it to tracer diffusion, here we study a minimal lattice model incorporating particle-particle collisions as well as different diffusion coefficients of different particle types to investigate the effect of activity and density of crowders on tracer diffusion, neglecting hydrodynamic interactions. Importantly, the collision rule we introduce goes beyond the simple exclusion rule often used in lattice models and allows for the pushing of one particle by another particle attempting to move to the first one's lattice site. We quantify the enhanced diffusion as a function
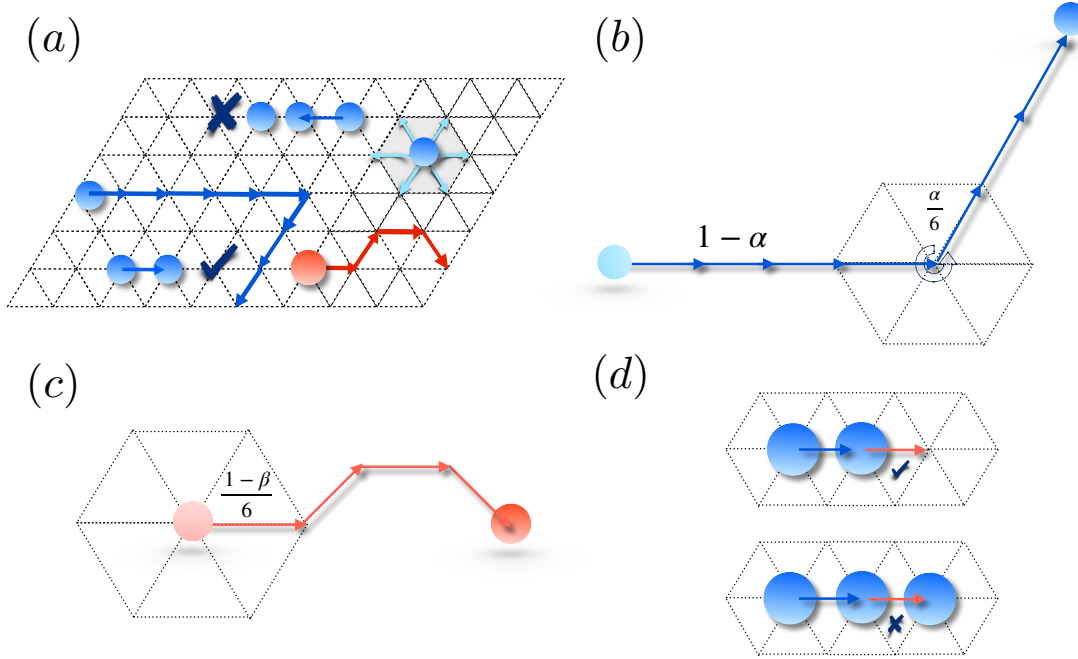
Figure 2.1 – *Lattice model of a dense system of active particles (blue) containing a passive tracer particle (red). a) Overview of the model on a hexagonal lattice. b) Active particles perform run and tumble motion and move persistently in the same direction with probability $1-\alpha$ and randomize that direction (tumble) with probability α (i.e., $\alpha/6$ for each direction). c) The passive tracer particle (red) performs a simple random walk, its diffusion coefficient is modulated by the parameter β. d) Collision rules among particles.*

of these parameters and relate the observed tracer diffusion to clustering of active particles. Finally, we generalize our analysis to the case of a binary mixture of active and passive particles. Our results indicate how the interplay between activity and density of crowders can lead to significant enhancement of the diffusion of a tracer, but also limits that enhancement through clustering of the active particles.

2.3 Model

We consider a hexagonal lattice (see Fig. 2.1(a)) in two dimensions, consisting of $M = 256 \times 256$ sites, with periodic boundary conditions (effects of the system size are discussed in Appendix A). There are in total n particles on the lattice, of which

$N_a = \chi_A N$ are active and can self-propel following a simplified run and tumble motion, and the rest are passive and exhibit diffusive behaviour. We define ρ as the number density of the system, which is defined as the total number of particles divided by the number of lattice sites.

For updating the position of all particles at each time step, n random actions take place in the system. A particle may be picked more than once in one single time step, giving rise to fluctuation of its speed. On average, however, all particles are picked equally often.

The active particles have run-and-tumble dynamics, where they move persistently in one direction (initially chosen at random), and then reorient with a tumbling probability α, resulting in long directed runs with abrupt turns. At each time step, the active particle moves in the same direction as in its last step with probability $1 - \alpha$, and tumbles to choose a new direction with probability $\alpha/6$. For instance, for $\alpha = 0.001$, the active particle takes, on average, 1000 persistent steps in the same direction, and then tumbles and chooses one out of the six possible directions with equal probability (see Fig. 2.1(b)). In the case of passive particles we set $\alpha = 1$: the particle reorients at each time step and therefore steps to each site with a probability of $1/6$. Since our aim is to study the effect of active particles on the overall motion of a passive particle, we put (at least) one passive 'tracer' in the system, which in general has a different Brownian diffusion coefficient set by a parameter β. The tracer steps to each neighbour site with probability $(1 - \beta)/6$, with $0 \leq \beta \leq 1$ as shown in Fig. 2.1(c). When $\beta = 0$, the tracer has the same dynamics as a ordinary passive particle, meaning it can move in each time step. As β increases, the tracer diffuses more slowly and in the limiting case of $\beta = 1$, it can only move by being pushed by its neighbors.

We now define collision rules among the particles. We use a modified exclusion rule, which in addition to ensuring that each site is occupied by at most one particle

also allows for particles pushing each other. In each stepping attempt of a particle, we check whether the target site on the lattice is empty or occupied. If it is empty, then the particle is allowed to update its position, as described above. If the site is occupied, then there are two possibilities depending on the second neighbor site of the particle in the same direction. If the latter site is empty, the stepping particle pushes the particle in the target site to the second neighbor site and moves to the target site itself. Otherwise, the update is rejected (see Fig. 2.1(d)). Note that there is no alignment interaction between particles in the pushing process. All simulations described in the following were run for 10^6 time steps with 1000 realizations of each condition.

2.4   Results

2.4.1   Tracer in a purely active system

2.4.1.1   Mean square displacement

We first discuss the results for a passive tracer particle in the presence of only active crowders (i.e., $N_a = N$ or $\chi_A \approx 1$). We considered densities in the range of $0.01 \leq \rho \leq 0.4$ and the tumbling probability of active particles between $0.0001 \leq \alpha < 1$.

We begin our analysis by evaluating the mean square displacement (MSD) of the tracer particles. We note that for Brownian motion, the MSD is given by, $\left\langle (\Delta r)^2 \right\rangle = 2dDt$, where Δr is the displacement of a particle in a given time interval of t, d is the spatial dimension (which is 2 in our case), D is the diffusion coefficient, and $\langle \cdot \rangle$ denotes an ensemble average. So-called anomalous diffusion is characterised by an MSD $\left\langle (\Delta r)^2 \right\rangle \sim t^\gamma$, where $\gamma \neq 1$ is a real positive number that classifies the different types of diffusion: sub-diffusion for $0 < \gamma < 1$, $\gamma = 1$ is a typical diffusion process and, super-diffusion for $\gamma > 1$ (where $\gamma = 2$ gives rise to ballistic motion).
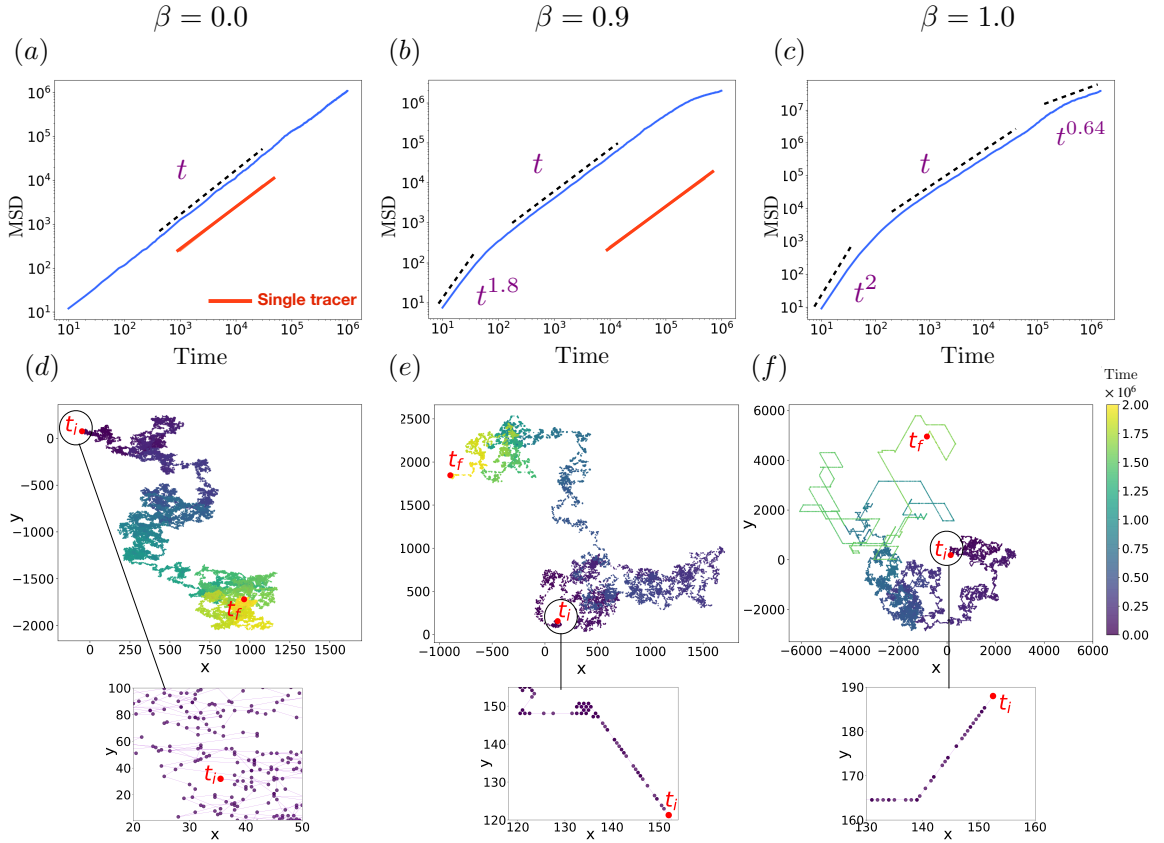
Figure 2.2 – *Diffusion of tracer particles with different diffusion coefficients in a system of active crowders. (a-c) The mean square displacement (thick blue lines) shows diffusive motion for $\beta = 0$ and anomalous diffusion for $\beta = 0.9, 1$. The red lines indicate the diffusive motion of the tracer in an otherwise empty lattice in (a) and (b), in (c) the tracer would not move in that case. The dashed lines indicate the scaling behavior of the different regimes, by showing the power laws fitted to the mean square displacement. (d-f) show trajectories (t_i and t_f indicate initial and final time, respectively in the trajectory plots), the figures in the last row show the zoomed view of the trajectories at the early stages. Each column corresponds to the value of β indicated above it. The other parameters are $\rho = 0.025$, $\alpha = 0.0001$.*

In Figs. 2.2(a)-(f), we have plotted the MSD and corresponding trajectories as a function of time for the three cases of $\beta = 0$, 0.9, and 1. In all three cases, the density and the tumbling probability of crowders are the same: $\rho = 0.025$ and $\alpha = 0.0001$. For a purely passive Brownian tracer with $\beta = 0$ (Figs. 2.2(a) and (d)), the tracer shows normal diffusion, with an MSD that is linear in time throughout the simulation. The trajectory is erratic at both long and short time (Figs. 2.2(d) and its inset, respectively).

It is useful to compare the diffusion coefficient of the tracer in this system to that of a passive tracer in the absence of active crowders. A general expression for the diffusion coefficient of a single passive particle on an arbitrary isotropic lattice is $D_0 = (\kappa/2d)a^2\lambda$, where a is the lattice spacing (distance between neighboring lattice sites), d is the spatial dimension, κ is the coordination number (the number of neighbour sites allowed for a jump), and λ is the stepping rate to the nearest neighbour site [104]. In our model $a = 1$ (i.e., all lengths are expressed in units of the lattice spacing), $\kappa = 6$, $d = 2$, and $\lambda = \frac{1-\beta}{6}$, leading to

$$D_0 = \frac{1 - \beta}{4}. \tag{2.1}$$

Thus, for $\beta = 0$ we find $D_0 = 1/4$. The corresponding MSD of a particle on an otherwise empty lattice is shown as the red line in Fig. 2.2(a). A comparison of the MSD without active crowders (red line) and the MSD in their presence (blue line) shows that the diffusion of our tracer particle is strongly enhanced by the active crowders.

For $\beta = 0.9$ and $\beta = 1$, by contrast, we can identify several diffusive regimes (indicated by the dashed lines, which show the scaling in the different regimes with behavior $\sim t^\gamma$ and γ obtained by fitting). A slow tracer with $\beta = 0.9$ initially undergoes super-diffusion (Fig. 2.2(b)) as it remains in front of an active particle over an extended period of time (see Fig. 2.3(a)). The tracer inherits the direction of an individual active particle which drives it forward. This effect can also be seen in the inset of Fig. 2.2(e), in which this directed motion yields a straight line. The observed diffusion exponent
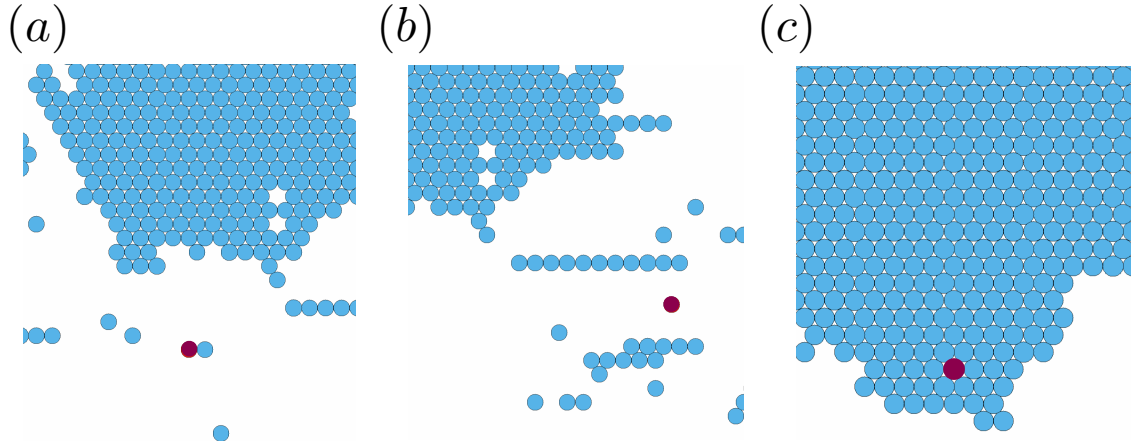
Figure 2.3 – *Snapshots of the simulation for $\rho = 0.1$ and $\alpha = 0.0001$: the active particles are shown in blue and the tracer particle in purple. a) The tracer (purple) is next to an active particle (blue), which pushes it. b) The tracer is trapped in empty space. c) The tracer is trapped by active particles.*

γ at short time is found to be 1.8, which is close to the ballistic regime with $\gamma = 2$. After a longer time, diffusive motion is recovered, with erratic trajectories similar to those for $\beta = 0$. The data also suggest that there may be a subdiffusive regime for very long times, see below.

Finally, Figs. 2.2(c) and (f) show the case where the passive tracer does not move by itself and only moves when pushed by an adjacent active particle. Initially, the tracer fully inherits the direction and the speed of the active particle that pushes it (Fig. 2.2(f) inset). Since there is only self-propulsion, γ is exactly 2. For an intermediate time, diffusive behaviour is recovered. Then after some time, the motion becomes remarkably less random, exhibiting long directed paths and pauses, as depicted in the trajectory in Fig. 2.2(f). Correspondingly, the exponent of the MSD is reduced to $\gamma \sim 0.64$, indicating a sub-diffusive behaviour. Inspection of snapshots of the lattice (Figs. 2.3(b) and (c)) show that during the pauses, the tracer is either trapped in an empty region of the lattice and thus cannot be moved, or in a cluster of active particles, within which it is also immobilized. This observation indicates that, in this case, the environment
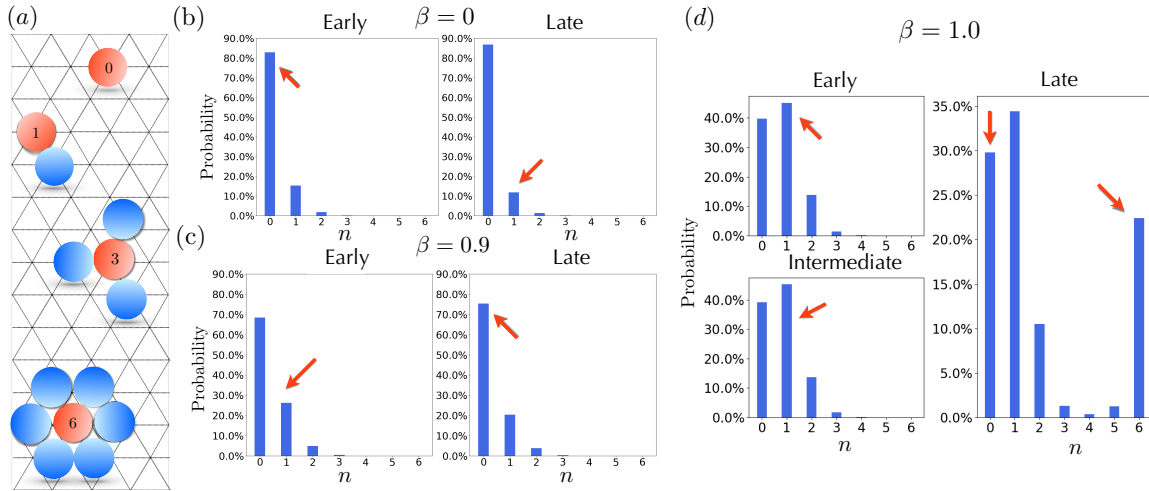
Figure 2.4 – *Trapping analysis. a) The sketch shows the tracer (red) surrounded by different number of active particles (blue). (b), (c) and (d) show the probability that n, neighbor sites are occupied (for $n = 0, \ldots 6$). The red arrows indicate the numbers of occupied neighbors most relevant for the different regimes in the MSD plots in Fig. 2.2. The probabilities were determined by averaging over 1000 simulation steps (starting at time 0 for the early state, at time 1000 for the intermediate state and 1000 steps before time 10^6 for the late state) as well as over 1000 realizations of the simulation (with random initial conditions).*

in which the tracer diffuses through changes from a homogeneous environment, to coexistence of a dilute phase and clusters of active particles. Cluster formation will be discussed in more detail below.

2.4.1.2 Neighbour site occupation and trapping

To quantify the effect of trapping on the motion of a tracer, we define a trapping parameter n, which characterizes the occupation of the six nearest neighbour sites of the tracer (see Fig. 2.4 (a)). Thus, $0 \leq n \leq 6$, with $n = 0$ indicating that the tracer has no neighbouring particle and $n = 6$ is the fully trapped state. When $n = 0$, the tracer with $\beta = 1$ is essentially trapped by the empty space and becomes immobile, while tracers with $\beta = 0$ and $\beta = 0.9$ diffuse on their own. In the fully occupied state ($n = 6$), the tracer is immobile for all the cases. $n = 1$ results in persistent directed motion of the tracer if the neighboring active particle moves to the site of the tracer

and $1 - \beta < 1 - \alpha$, as the active particle then pushes the tracer for multiple steps.

For the two cases $\beta = 0$ and $\beta = 0.9$, the histograms of n do not vary significantly over time, with the probability of having no neighbors being the largest (Figs. 2.4(b) and (c)). As expected, the probability of having a single neighbor ($n = 1$) is higher for $\beta = 0.9$ than $\beta = 0$, in agreement with the observed directed motion. For $\beta = 1$, $n = 1$ is the most probable configuration at all times. However, the histogram remarkably broadens over time and becomes bi-modal at long times, with $n = 0$ and $n = 6$ occurring (almost) equally frequently. This means that the three most likely configurations are those that lead to directed motion ($n = 1$), trapping in empty space ($n = 0$) or trapping in a cluster ($n = 6$), which together explain the range of motion observed in Fig. 2.2(f). This trapping appears to be the reason for the subdiffusion observed in this case for the long-times regime. By contrast, no such trapping is clearly seen for the case $\beta = 0.9$. We therefore hypothesize that the apparent transition to subdiffusion at long times in this case may be due to more transient trapping of the tracer, e.g. between just two active particles moving into opposite directions.

2.4.1.3 Effective diffusion coefficient at large times

We have observed above that diffusion of the tracer is enhanced in the bath of active particles compared to the tracer on its own. To study this further, in Fig. 2.5, we plot the diffusion coefficient at large times as a function of density, focusing on the case $\beta = 0.9$. The simulation was performed for a system with $\chi_A = 1$, and different values of α. Remarkably, the effective diffusion coefficient has a 50-fold increase when in the active bath, compared to the diffusion coefficient of an isolated tracer. Even at a low density ($\rho \approx 0.01$) of active crowders, the diffusion coefficient of the tracer is substantially greater than in the absence of active crowders, implying a strong effect of being pushed by active particles.

(a)

(b)

(c)

(d)
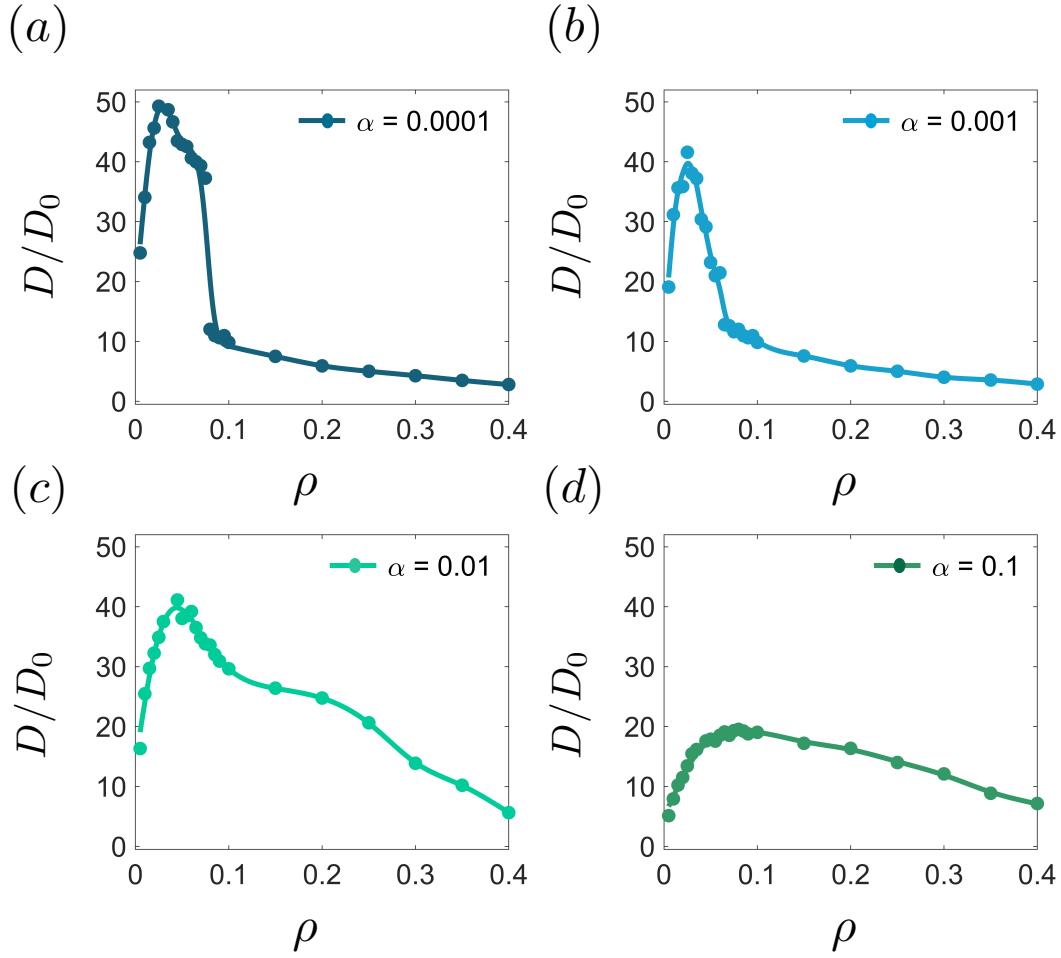
Figure 2.5 – *The relative diffusion coefficient of a tracer with $\beta = 0.9$, normalized to the diffusion constant D_0 of an isolated tracer.*

Since the diffusion coefficient of a single passive tracer is a small constant in the absence of crowders and goes to zero in the presence of a high density of crowders, the relative diffusion coefficient is expected to be a non-monotonic function of the density. Furthermore, the form of this dependence should also vary with the tumbling probability. The plots in Fig. 2.5 show a clear density dependence of the diffusion coefficient. The diffusion coefficient is sharply enhanced when the density of active particles is increased from zero, then decreases after a pronounced peak. Clearly, the density of the system greatly affects the diffusion coefficient of the tracer. To further investigate this effect, we come back to the observation of cluster formation. Additional
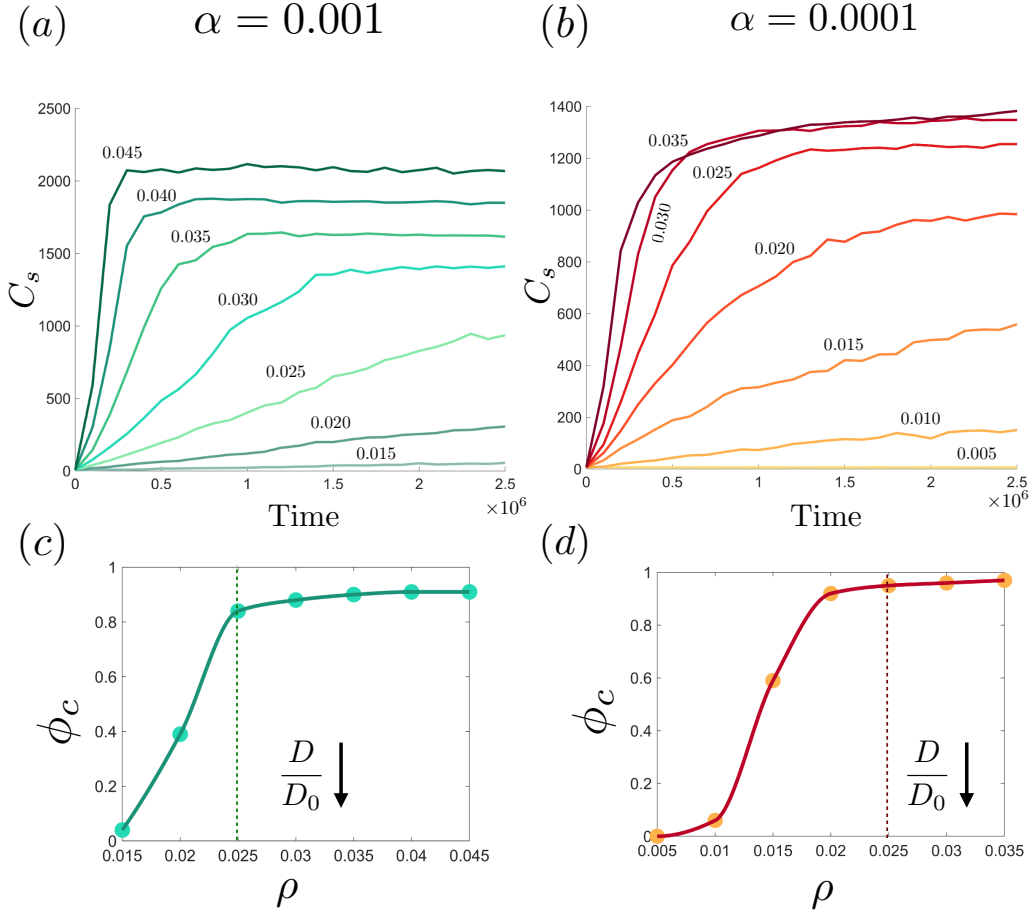
Figure 2.6 – *Cluster analysis: a) and b) Average cluster size as a function of time (averaged over 1000 realizations) for different densities. The numbers above the curves indicate the corresponding density. c) and d) Fraction of particles assembled in clusters in the last snap shot of simulation for the same densities. The dashed lines mark the density in which the tracer exhibits the maximum diffusion coefficient. Each column corresponds to the value of α indicated above it.*

analysis for the case $\beta = 1.0$ is provided in Appendix B.

2.4.1.4 Cluster formation

To analyze clustering, we define a cluster as a collection of at least six particles 'sticking together', i.e. being connected via mutual nearest neighbors. Particles without nearest neighbor or connected to fewer particles are considered as belonging to the gas phase. Clusters are identified with the data analysis framework Freud [105]. We measured

the average cluster size, C_s, as the average number of particles in a cluster over 1000 different realizations of the simulation. Figs. 2.6(a) and (b) show the time evolution of C_s for different densities and for $\alpha = 0.001$ and 0.0001, respectively. As can be seen in Figs. 2.6(a) and (b), cluster formation is accelerated by increasing the density of crowders.

In Fig. 2.6(c) and (d), we plotted the fraction of particles detected within clusters, ϕ_c, as seen in the last snapshot of the simulation which provides an estimate of the fraction of particles assembled in the clusters. ϕ_c can be described by $(N_c \times C_s)/N$, where N_c is the average number of clusters. As a function of the density, ϕ_c shows a clear transition from a state in which a very small fraction of particles are in the clusters to a state where almost all particles are in clusters.

To relate clustering to the tracer diffusion discussed before, we indicate with the vertical dashed lines the density at which the tracer's diffusion coefficient for the given tumbling probability is maximal. These lines fall near or slightly above the transition, suggesting an intimate relation of the decline in diffusion to the onset of phase separation. When the active crowders start to form clusters, there is coexistence of a dilute gas phase and clusters of active particles and the probability of active crowders being in the dilute phase decreases as long as the cluster size increases. Consequently, the diffusion coefficient of the tracer decreases as there are fewer and fewer active crowders in the dilute phase to push the tracer and enhance its diffusion.

2.4.2 Binary Mixture

Finally, we consider a binary mixture of active and passive crowders, with $\chi_A + \chi_P = 1$ where χ_P is the fraction of passive particles. We tracked the effect of the three control parameters χ_A, α and ρ on the diffusion coefficient of a tracer particle with $\beta = 0.9$. Adding passive particles into a purely active system changes not only the directionality
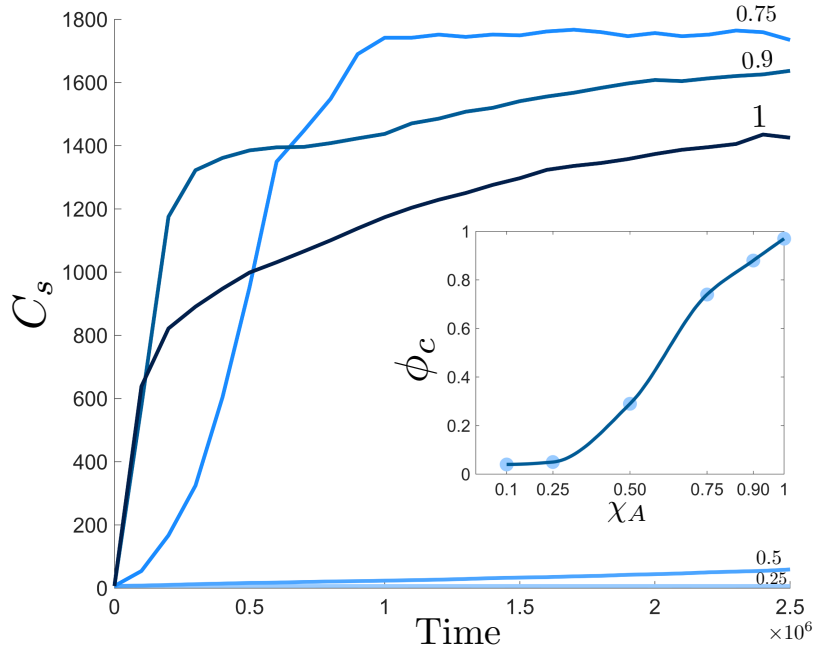
Figure 2.7 – *Cluster analysis for different fractions χ_A of active particles at fixed $\rho = 0.05$. Cluster size and fraction of particles in clusters (inset) as in Fig. 2.6 for different χ_A in a binary mixture of active and passive crowders. The numbers above each curve indicate the fraction of active particles (χ_A).*

imposed by collisions (due to pushing by the active particles), but also alters the global dynamics in a subtle way, specifically the dynamics of clustering. In the example shown in Fig. 2.7 with a fixed low density of crowders, an increase of the fraction of active crowders above 0.5 leads to a strong clustering signature both in the average cluster size C_s and in the fraction ϕ_c of particles within clusters (inset). The cluster size C_s shows biphasic growth for large fractions of active crowders with first rapid increase in the cluster size and then a much slower second phase, which appears to be more pronounced and slower for the largest active crowder fractions. Put differently, replacing some of the active crowders with passive particles delays the phase separation (compare the cases $\chi_A = 1$ and $\chi_A = 0.75$ in Fig. 2.7), likely because initially the rapid directional change of the passive particles randomizes the motion of the active particles. Eventually, however, clustering sets in. While clustering sets in later for $\chi_A = 0.75$

than for $\chi_A = 1$, it reaches its stationary state faster.

Above we have shown a correspondence between the onset of clustering and a decrease of the enhanced diffusion of a passive tracer (Fig. 2.5). Since clustering is decreased by increasing the fraction of passive particles in the system, we expect that the decrease in diffusion of the tracer is less pronounced when passive particles are present. This is indeed the case, as shown in Fig. 2.8, where we plot the diffusion coefficient as a function of the density for different combinations of the tumbling probability α and the fraction of active crowders χ_A: decreasing the fraction of active crowders leads to a broader peak in the diffusion coefficient as a function of density. We interpret this observation as reflecting the fact that at low χ_A, it is more likely to find many of the active particles (which can push the tracer) in the gas phase compared to higher χ_A. At the same time, however, the value of the maximal diffusion coefficient is also decreased, reflecting the fact that the total number of active particles is reduced. Nevertheless, even for very low fractions of active particles (bottom row in Fig. 2.8), the diffusion coefficient is still increased compared to the case with only passive particles. For instance, for $\alpha = 0.1$, $\chi_A = 0.1$, it is increased up to 5-fold.

2.5 Conclusion

In this study, we have analyzed the diffusion of a tracer particle in a crowded active system using a minimal lattice model. We implemented the pushing of a passive tracer by active crowder particles by a simple collision rule. A passive tracer in an otherwise purely active system or in a binary mixture of active and passive particles exhibits different motility regimes including significantly enhanced effective diffusion. Enhanced diffusion of tracers in the presence of active particles has been observed in several different systems such as in a bath of swimming microorganisms [82, 85, 93] and in a suspension of actively diffusing enzymes [73]. The activity mechanisms and the
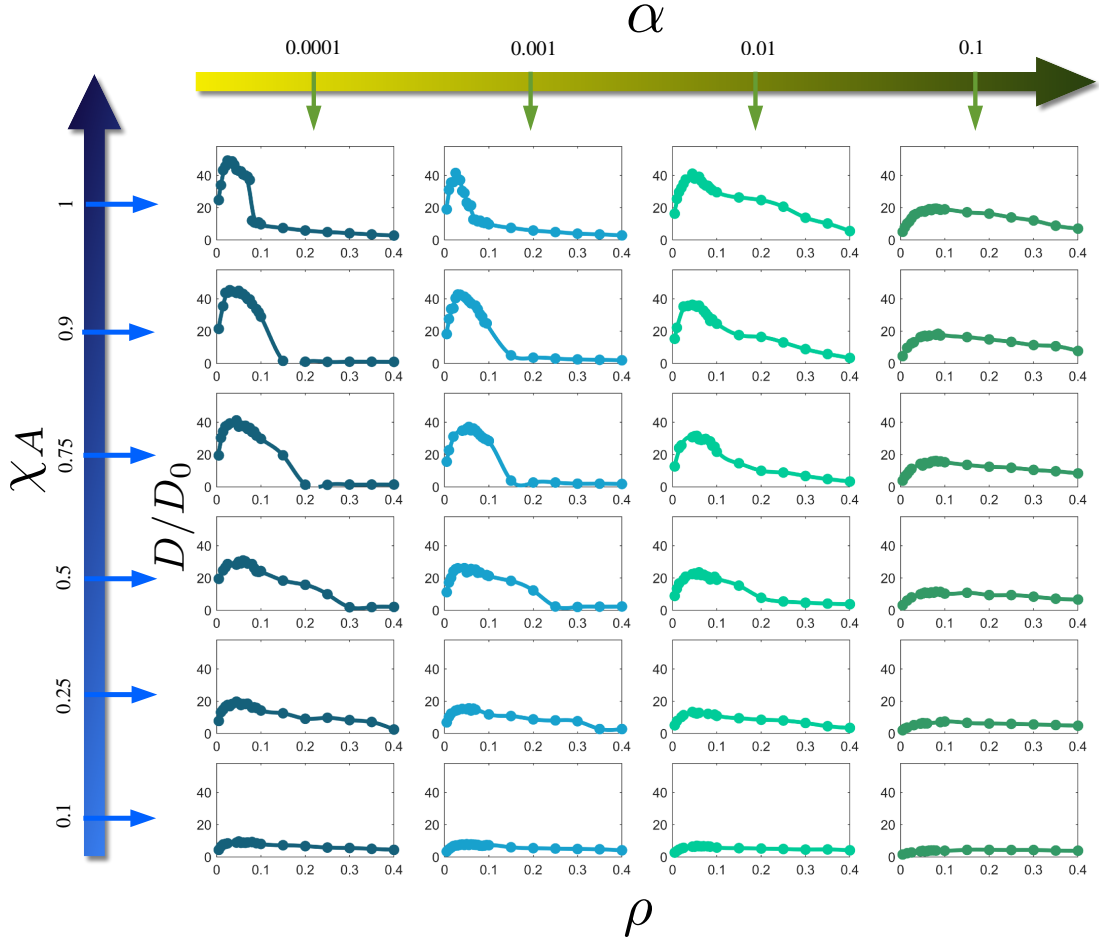
Figure 2.8 – *The diffusion coefficient of a tracer with $\beta = 0.9$ as a function of the density ρ and of the fraction of active row χ_A in a binary mixture.*

interaction in these systems are more complicated than those studied in our model, but the results shown here and related results of others [99] demonstrate that simple interactions are sufficient to generate such enhanced diffusion and can result in rich dynamic behavior. Our results show that the extent to which diffusion is enhanced depends on the activity of the crowder particles (modulated via their hopping rate relative to the tracer's hopping rate and via their tumbling probability, i.e. via the persistence of their motion) and on their density. The interplay of activity and density depends on the dynamics of the particles directly, but also indirectly via the phase separation of the crowders into low-density (gas-phase) regions and dense clusters. The

latter has a negative effect on the mobility of the tracer, both when the tracer becomes trapped in a cluster and when the tracer moves in a low-density area, where it is not pushed by active particles. Our findings thus point to an intricate interplay between the local dynamics of enhanced tracer diffusion and the global dynamics of the system.

One feature of active particle systems that we have not considered here are hydrodynamic interactions, which are typically present. On the one hand, studies like our present one or [106] show that phenomena such as enhanced tracer diffusion that are often observed experimentally in systems, where hydrodynamic interactions are present, are not dependent on those hydrodynamic interactions, but can also be found in reduced models without them. However, in general, one can expect that the quantitative results are modified by the inclusion of hydrodynamic interactions, both between the particles and with the surfaces that confine the particles to a quasi-two-dimensional system [107–109]. We hypothesize that the dominant effect of hydrodynamic interactions would be due to the interactions of particles with the surface of a relatively rigid clusters of particles and result in a rotation of the arriving particle similar to the case of a rigid wall. Depending on the extent of the resulting torque, such interactions could enhance or reduce cluster formation. One way of including such effects into a minimal lattice model would be via an additional update rule that rotates particles near the surface of a cluster.

Another aspect that could be of interest is whether the underlying lattice type influences the dynamics of the tracer particle. Phase separation as observed here has indeed been studied in models of active particles on different lattices [101, 103]. Specifically different lattices may allow different interaction rules, particularly if, as in our case, lattice sites beyond the nearest neighbor have an influence. For example, one recent study showed clustering and a hexatic phase in a system of passive particles on a hexagonal lattice [102].

Given the simplicity of our model, one can also extend it to other collision rules among the particles as well as use it to study the impact of active crowding on physical processes other than tracer diffusion.

Acknowledgement

Appendix

2.6   Effect of system size

To check whether the size of the lattice affects the results presented here, we ran simulations with different system sizes ($L = 50, 100, 256, 512$). Fig.2.9 shows the MSD of the tracer particle for two different densities of active crowders ($\rho = 0.02$ and $\rho = 0.40$). The results for different system sizes lie almost of top of each other, with only some deviations at long times for the smallest system size ($L = 100$ in Fig.2.9a and $L = 50$ in Fig.2.9d). Importantly, while the small values of α used in many of our simulations in principle allow for persistent motion of the active particles over distances exceeding the system size, due to the interactions between the particles this is typically not the case except for very low densities.
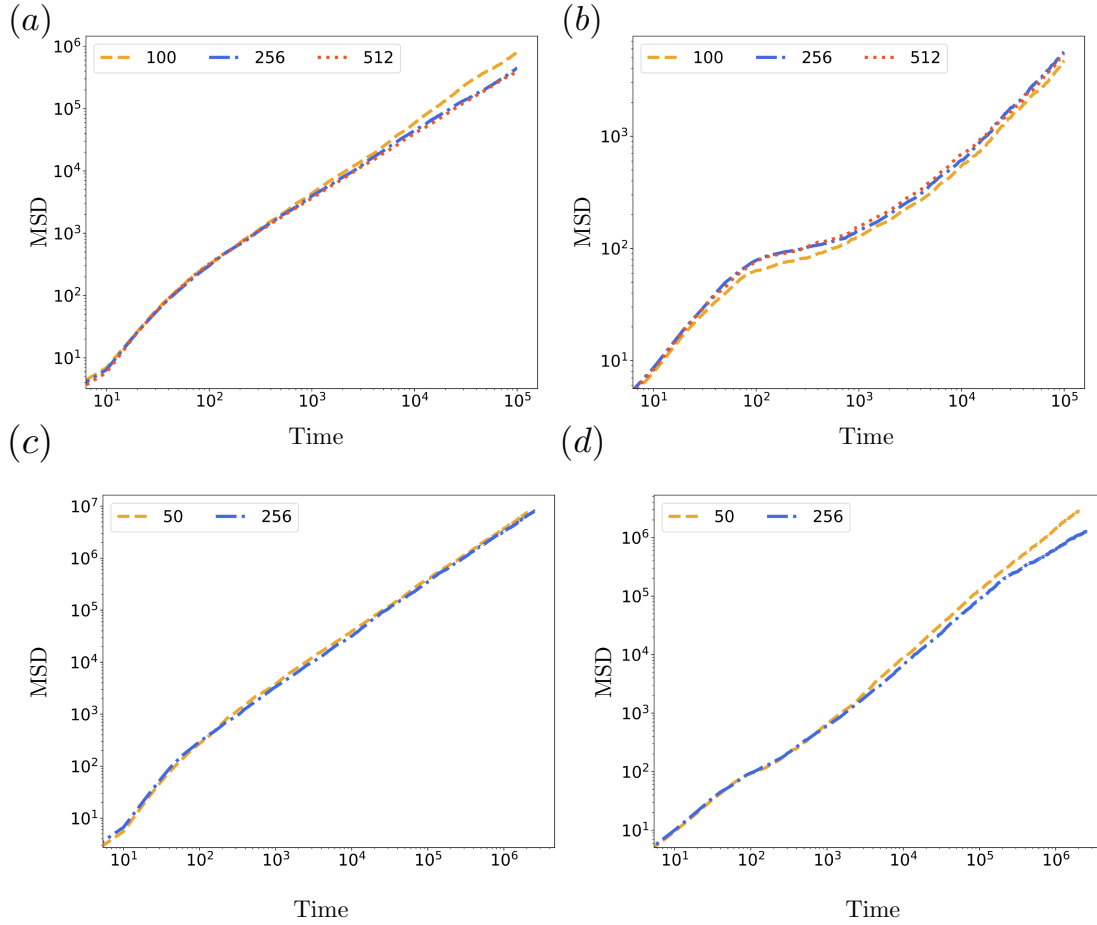
Figure 2.9 – *MSD as a function of time plotted for different simulation box size ($L = 50$, 100, 256 and 512) for densities (a) $\rho = 0.02$ and (b) $\rho = 0.4$, both with $\alpha = 0.0001$ (c) $\rho = 0.02$ and (d) $\rho = 0.4$, both with $\beta = 0.9$ and $\alpha = 0.01$. $\beta = 0.9$ in all cases. All the plots are averaged over 1000 realizations for each box size.*

2.7 Long-time dynamics for $\beta = 1.0$

The observation of trapping of the tracer in either clusters of active particles or in empty areas of the lattice in the case where the tracer cannot move on its own ($\beta = 1$) suggests the question whether such trapping and the subdiffusion resulting from it exhibits a sensitive dependence on the density, as a sufficient density may be required for trapping. We therefore simulated tracer mobility over a wide range of densities for $\beta = 1$ and four different values of α. α. As one can observe in Fig. 2.10 the
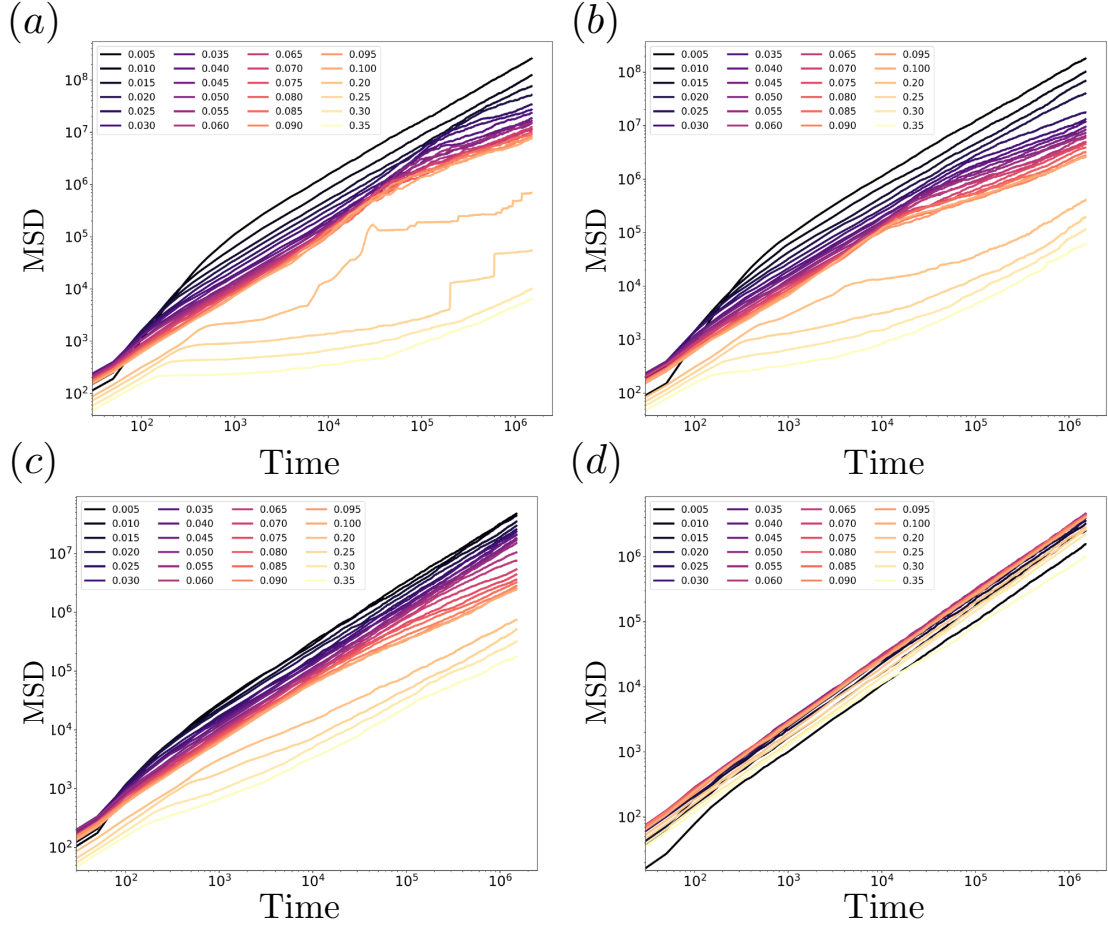
Figure 2.10 – *The mean square displacement of a tracer with $\beta = 1.0$ as a function of time for different densities and tumbling probabilities (a) $\alpha = 0.0001$ (b) $\alpha = 0.001$ (c) $\alpha = 0.01$ (d) $\alpha = 0.1$.*

tracer shows purely normal diffusion for the largest value of α, with non-monotonic dependence of the diffusion coefficient on density similar to Fig.2.5. For the smaller values of α, a subdiffusive regime appears for long times, as the active particles start to form stable or transiently stable clusters and trapping of the tracer starts to play a role. The transition to subdiffusion appears to occur at a critical density, which depends on the tumbling probability which is $\rho \simeq 0.020$ for $\alpha = 0.0001$, $\rho \simeq 0.025$ for $\alpha = 0.001$ and $\rho \simeq 0.060$ for $\alpha = 0.01$. In all cases, these values fall near to the onset of phase separation as shown in Fig. 2.6 (c) and (d). There also appears to be a second transition, clearly visible for $\alpha = 0.001$ and $\alpha = 0.01$, where for densities ≥ 0.25 a

plateau at intermediate times develops, likely also due to trapping.

Chapter 3

Strong Velocity Correlation in Suspensions of Passive Particles generated by Active Dopants

3.1 Introduction

Active matter is a novel class of non-equilibrium systems consisting of motile components, where energy is consumed and dissipated at the scale of the constituent units to generate systematic motion. These systems extend across an enormous range of length scales, from the cytoskeleton [1–3], bacterial colonies [4–6], and tissues [69] to bird flocks and animal herds [8, 110]. Being out of equilibrium, these disparate systems can exhibit exotic collective behavior which is absent in their equilibrium counterpart. For instance, they are capable of self-organizing into fascinating and perplexing dynamical patterns such as flocks, swarms, and vortices, to name just a few. One of the most popular theoretical models to describe such a diverse class of collective behavior, namely flocking, is the Vicsek model [32]. This model was introduced two decades ago to describe a flocking transition assuming an ensemble of self-propelled point-like agents
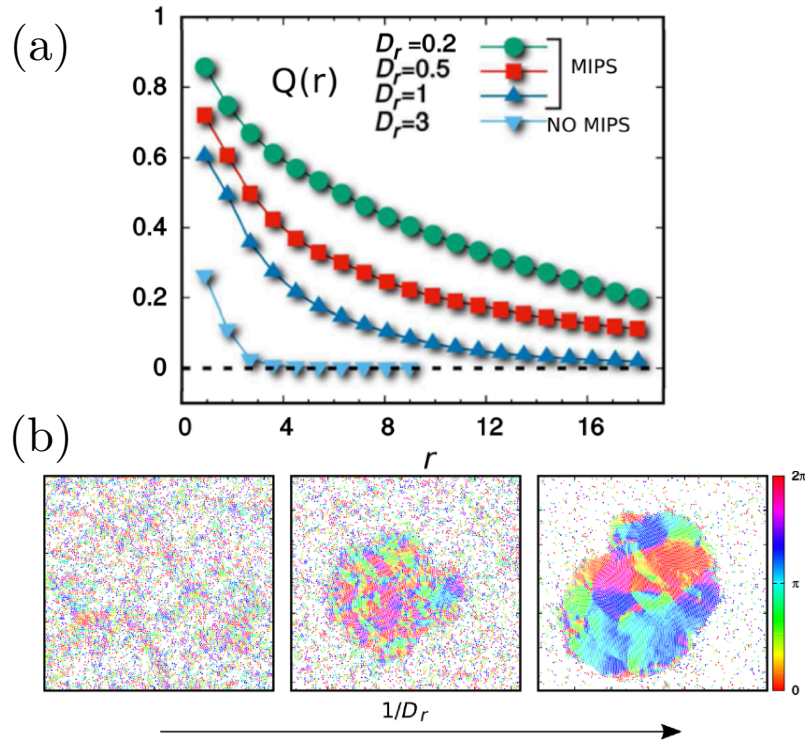
Figure 3.1 – *Panel (a) the spatial correlation function of the velocity orientation $Q(r)$, for the different values of D_r has been plotted. Correlation length increases with decreasing the rotational diffusion coefficient. Panel (b) shows the typical configurations for three different values of D_r. With decreasing rotational diffusion, domains with aligned velocity emerges in the system. Colors encode the direction of the velocity of each particle. Plots are taken from [59].*

with explicit mutual alignment interaction in the presence of external noise. One of the most astounding observations made in this context is that the Vicsek model system can give rise to a spectacular collective movement known as swarming which results in long-range orientational order in two dimensions, unlike in equilibrium systems. Only when driven out of equilibrium, this system can show discernible long-range order which is impossible to attain in equilibrium systems as proven by the Mermin Wagner theorem [111, 112].

Explicit alignment interactions are not always present in active matter systems. Even in the absence of explicit alignment interactions, active systems display rich phenomenology compared to their passive counterparts. Most remarkably, motile
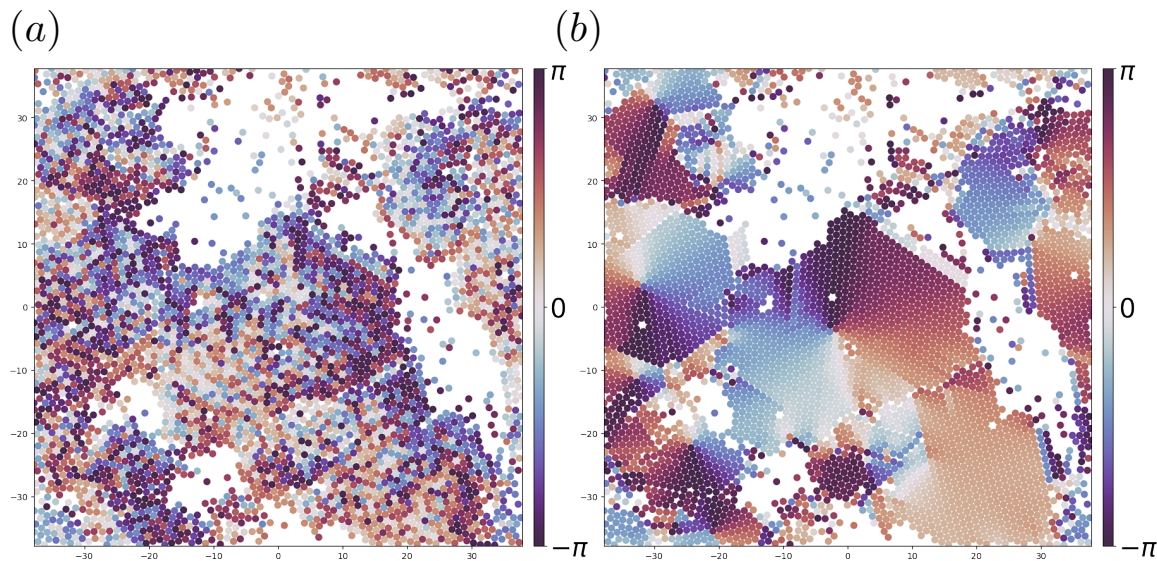
Figure 3.2 – *A snapshot of the configuration of the active particles. They have self-aggregated due to motion-induced phase separation. Panel (a) colors are associated with polarity of particles. The particles within the clusters are uncorrelated. Panel (b) colors encode the velocity direction of the particles. There is a strong correlation within clusters of active particles. Both panels are the same snapshot, only the color codes are different. The snapshot is realized with the density ~ 0.7 and $D_r = 0.001$*

entities with purely repulsive interactions can undergo phase separation (for large activity characterized by Péclet number) which is impossible for passive systems without attractive interactions. This phenomenon stems from the persistently non-equilibrium nature of the particles and is known as motility-induced phase separation (MIPS) [11, 58, 113]. The simple reasoning is: when the speed of motile units decreases abruptly with increasing local density, a homogeneous system becomes unstable, resulting in a phase-separated system in which a dense liquid with significantly reduced motility coexists with a dilute highly motile gas. Note that, although the system shows some global structural order, motile entities in the dense fluid exhibit no orientational order in the propulsion direction and those in the low-density state continuously join and leave the boundary of the dense state again without showing any orientational order.

Even though, due to the lack of explicit alignment interactions, there exists no
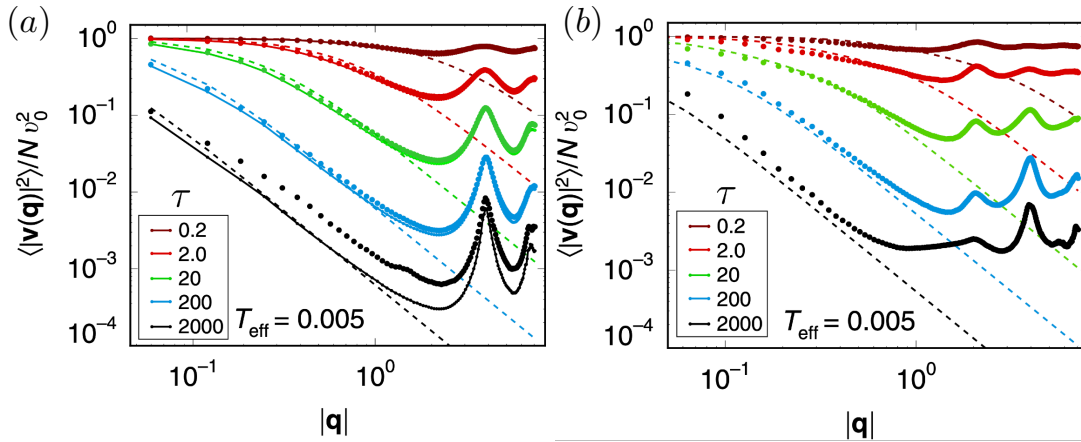
Figure 3.3 – *Panel (a) shows the behaviour of Fourier space velocity correlation functions for the soft disk model for different persistence time τ in a solid/ glassy phase at $T_{eff} = 0.005$. Panel (b) describes Fourier velocity correlations for the self-propelled Voronoi model (SPV), together with analytical prediction (dashed line). Plots are taken from [60].*

orientational ordering of the propulsion direction, also known as particle polarity, (see figure. 3.2.a), very recently, some groups have found that there is a strong velocity correlation in the dense limit of such systems of self-propelled particles. Caprini *et al.* [59, 114] have reported spontaneous velocity alignment in a $2d$ system of repulsive monodisperse, active Brownian particles which is associated with MIPS in the system (see figure. 3.2.b). They found that having sufficiently high density (in the solid-like state) of self-propelled particles is crucial for the emergence of spontaneous velocity alignment. Added to that, as the persistence time of the self-propelled particles increases the domains with aligned velocities grow (figure. 3.1.b). Moreover, the spatial velocity correlation increases as rotational diffusion coefficient decreases (figure. 3.1.a). In a recent work, Henkes *et al.* [60] have also observed similar velocity alignment in the epithelial cell monolayers over several cell sizes and also showed that the domains (with a finite bulk modulus) with aligned velocities grow as the square root of the persistence time of the self-propelled particles. They confirmed this observation with a simulation of a dense (solid-like) repulsive assembly of polydisperse over-damped
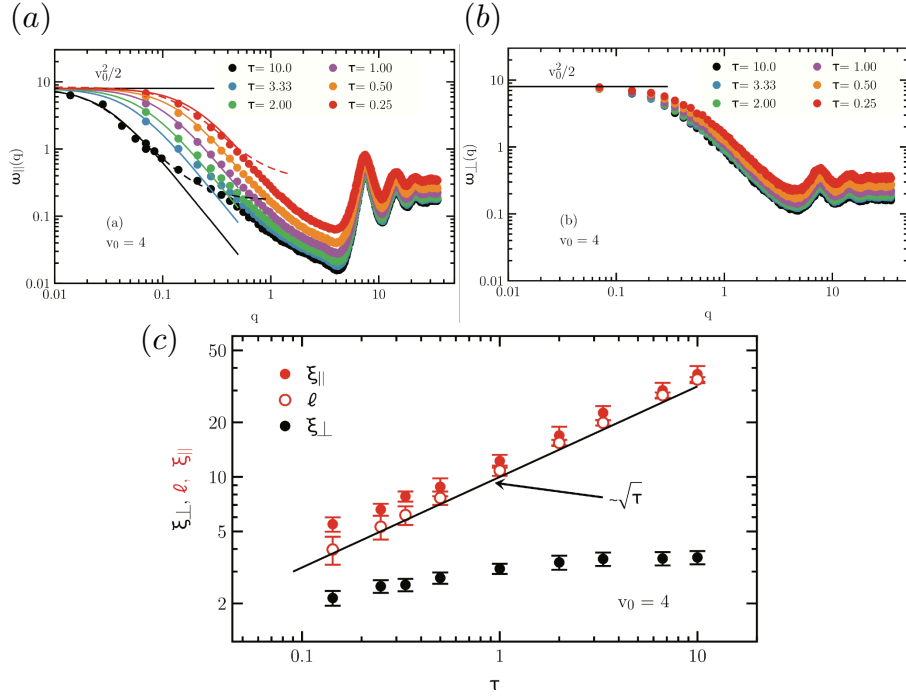
Figure 3.4 – *Panel (a-c) show the equal time velocity correlation functions at a fixed self propulsion velocity ($v_0 = 4$) for a range of τ. Panel(a) the longitudinal correlation function shows a rapid growth with increasing τ and in Panel (b) the transverse correlation is almost fixed. Panel(c) shows the longitudinal and transverse correlation length obtained from panels (a) and (b), respectively. The longitudinal correlation length scales with the square root of τ and the transverse correlation length is almost unchanged. Plots are taken from [61].*

active Brownian particles (see figure. 3.3.a) as well as a self-propelled Voronoi model (SPV) (see figure. 3.3.b). In figure . 3.3.a, they have shown that for a soft disk at low $T_{\text{eff}} = 0.005$, a dramatic $1/q^2$ slope has developed in the correlation function as τ increases. Indeed, in figure. 3.3.b, they showed the same simulation result for the SPV model. This observation is consistent with the findings of Caprini *et al.* [59, 114].

Later, Szamel *et al.* [61] showed that the velocity alignment is even present in a dense fluid-like system of self-propelled particles. They derived a microscopic theory to describe spatial velocity correlations in systems of active liquids and found that the longitudinal velocity correlation (due to finite bulk modulus of liquid) is very large and grows with persistence time (as reported by Caprini *et al.* [59] and Henkes *et al.* [60])

even in a liquid state. In figure. 3.4.a, they have plotted the equal time longitudinal velocity correlation, which shows a rapid growth with increasing τ, as well as the transverse correlation function in figure. 3.4.b which is almost constant. By contrast, in the absence of the shear modulus, the transverse velocity correlation is small and does not grow with the persistence time of the self-propelled particles (see figure. 3.4.c).

These studies have revealed that velocity correlation is a ubiquitous property in dense active matter systems, regardless the system being solid or fluid-like. The indispensable elements for forming such a strong velocity correlation are a) high-density assembly of self-propelled particles and b) persistent driving force. The question, however, is whether we can decouple the effect caused by the high density from the one caused by the activity/ persistence? To put it in another way, can a similar effect emerge in a dense passive system in the presence of a small number of active particles? In such a scenario, density and persistent activity are associated with and controlled from two different sources. In this chapter, we address this question and show that only a very small fraction of active particles is sufficient to demonstrate long-range velocity correlation in the system as long as the density of the embedded passive medium is high. We explore the effect of active forcing and persistence of this small fraction of active dopants on such large velocity correlations generated in the passive system by tuning the activity parameters. This study motivates and guides future experimental work to observe and study such exotic non-equilibrium signatures in simple tabletop experiments by adding a very small fraction of active Janus colloids in a dense suspension of passive colloids.

3.2   Model

For the numerical realization of the above scenario, we consider a binary mixture of $N = N_a + N_p$ particles, where N_a and N_p denote the number of active and passive
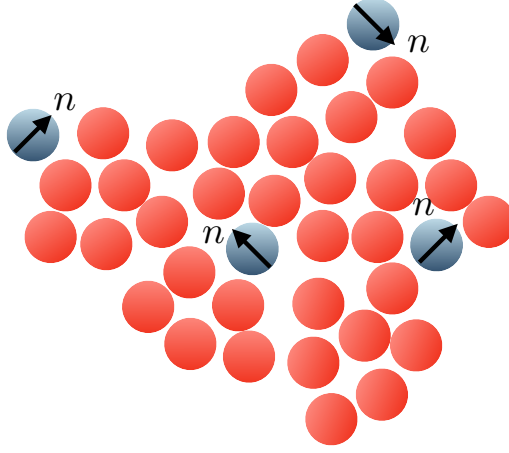
Figure 3.5 – *Schematic of the model employed in the simulation of the active/passive mixture. The mixture consists of active (blue) and passive (red) particles where **n** represents the self-propelling direction of each active particle.*

particles, respectively. Hence, $\phi_a = \frac{\pi N_a d^2}{4L^2}$ and $\phi_p = \frac{\pi N_p d^2}{4L^2}$ are the volume fractions of active and passive particles, respectively, where $L = 100\sqrt{\pi}$ is the box size and d is the particle diameter. The position, $\mathbf{x}_i$ and orientation, θ_i of the i-th self-propelled particle (undergoing an over damped motion) are given by these equations of motion:

$$\gamma \dot{\mathbf{x}}_i = \mathbf{F}_i + f_{act}\mathbf{n}_i \tag{3.1}$$

$$\dot{\theta}_{\mathbf{i}} = \sqrt{2D_r}\zeta_i, \tag{3.2}$$

where i is the index of the active particle, $i = 1, .., N_a$, f_{act} is the self-propulsion force, and $\mathbf{n}_i = (\cos(\theta_i), \sin(\theta_i))$ is the orientation vector. Here, D_r is the rotational diffusivity and ζ_i is the rotational noise which is Gaussian and white, with zero mean and correlations $\langle \zeta_i(t)\zeta_j(t') \rangle = \delta(t - t')$. The persistence time of self-propulsion, τ_p, is defined as the inverse of the rotational diffusion coefficient $\tau_p = 1/D_r$. We use $\gamma = 1.0$ as the constant drag coefficient in the system. In our model, active particles are not

affected by any explicit translational noise. Now for the passive particles, in the absence of rotational and translational noise, the overdamped equation of motion reads,

$$\gamma \dot{\mathbf{x}}_i = \mathbf{F}_i, \tag{3.3}$$

where $\mathbf{x}_i$ is the position of the i-th passive particle and $i = N_a + 1, .., N$. All particles in the system interact only through the steric interactions caused by the force $\mathbf{F}_i = -\nabla U_{tot}$. The potential energy $U_{tot} = \sum_{i \neq j} U(r_{ij})$ and the purely repulsive pair-wise interaction potential $U(r_{ij})$ is given by:

$$U(r_{ij}) = \begin{cases} 4\epsilon \left[\left(\frac{\sigma}{r_{ij}} \right)^{12} + \left(\frac{\sigma}{r_{ij}} \right)^{6} \right] + \epsilon, & r_{ij} < d \\ 0, & \text{otherwise,} \end{cases} \tag{3.4}$$

where $r_{ij} = x_i - x_j$ is the distance between particles i and j and d is an effective diameter with $d = 2^{1/6}\sigma$. σ and ϵ are characteristic length and energy scales for the Lennard Jones interaction, which is here truncated to its repulsive part, to this form, also known as Weeks-Chandler-Andersen potential.

We evaluate the velocity correlation in the system by analysing the spatial velocity auto-correlation function defined as

$$C(r) = \left\langle \frac{1}{N(N-1)} \sum_{i,j \neq i} (\hat{v}_i(\mathbf{r}_i) \cdot \hat{v}_j(\mathbf{r}_j)) \, \delta(r - |\mathbf{r}_i - \mathbf{r}_j|) \right\rangle \tag{3.5}$$

where r is the spatial distance and $\hat{v}_i(\mathbf{r}_i)$ is unit vector of the velocity of the i-th particle. Note that $\langle ... \rangle$ represents an average over steady state velocity configurations. This correlation function by construction starts from 1 and goes to 0 in the limit $r \to \infty$. Now, we also define the correlation length (ξ) over which the correlation function decays substantially, through $C(\xi) = \frac{1}{e}$. In the following sections, we analyse this correlation function and the correlation lengths for different densities of active (ϕ_a)

Figure 3.6 – *Snapshots of configurations of a purely active system for different area fraction of active particles. Panel (a) $\phi_a = 0.1$, panel (b) $\phi_a = 0.375$, panel (c) $\phi_a = 0.0.75$, Panel (d) $\phi_a = 1.0$. With increasing area fraction, clusters emerge in the system due to the motility. There is a velocity alignment among particles within the clusters. Colors encode the velocity direction of particles.*

and passive (ϕ_p) particles and also for different activity parameters f_{act} and τ_p (for a fixed mixture component).

3.3 Velocity correlation in a purely active system

We start by considering a purely active system with $\phi_p = 0$ and investigate the influence of the density of active particles (ϕ_a) on the velocity correlation. Since the density of the active particles is low, the probability of collision between particles is also low; hence, the velocity correlation is rather weak due to the lack of steric interactions (see figure 3.6(a)). With increasing density, the probability of collision increases. Therefore, a velocity correlation emerges in the system and this also seems to grow with increasing density. At smaller densities, one can see small correlated colonies of particles (see figure 3.6(b)) and with increasing density one observes bigger and bigger clusters of particles with strong velocity correlation across the cluster (see figure 3.6(c)). Finally, when the density is so high that the area fraction (ϕ_a) goes to ~ 1 the correlation length reaches the system size (see figure 3.6(d)).

Figure 3.7 shows the dependence of the velocity correlation on density. The color
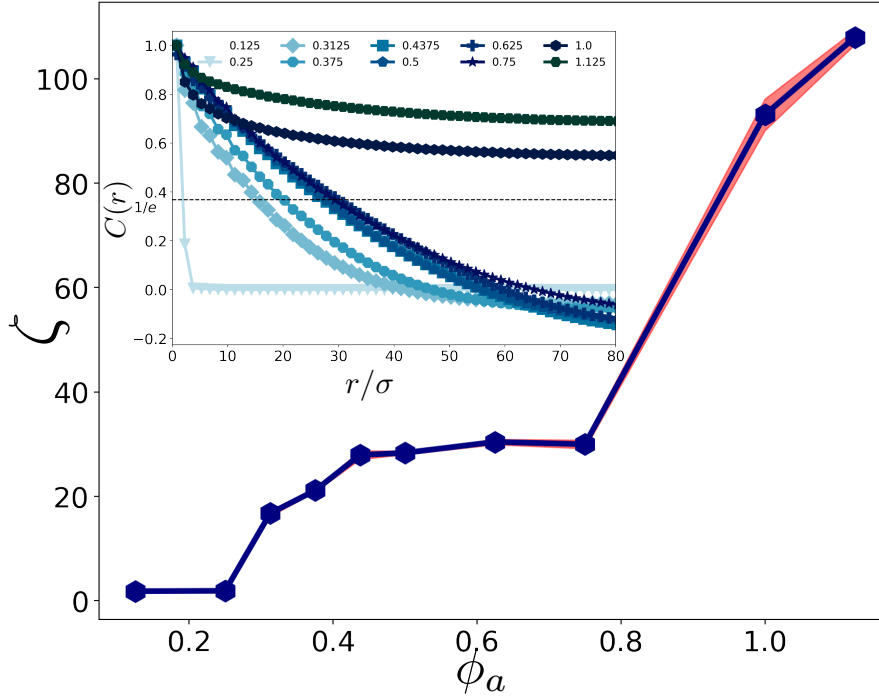
Figure 3.7 – *The correlation length obtained from fitting $C(r)$ in the inset figure as a function of area fraction of active particles*

represents the velocity direction of the particles. Note that there is a sudden jump close to $\phi_a \sim 0.8$ (see figure. 3.7) which is related to the rigidity percolation as at this density, the system becomes mechanically rigid. The above observation (growth of correlation with density) means that we need a system with a sufficiently high density of active particles to observe such large velocity correlations. Once we reach this density, rotational diffusion and activity start to play a significant role not only to control the size of the clusters but also to generate and sustain velocity correlation. This phenomenology is consistent with the previous studies. Caprini [59] showed that at higher density the motility-induced phase separation (MIPS) is accompanied by an inevitable velocity correlation. They found that the transition between hexatic and solid phases at higher density initiates the alignment of particles, leading to a quasi-long-range order in the system. The average size of the domains with aligned velocities grows as $\sqrt{\tau_p}$, where τ_p is the persistence time of the self-propulsion force

of active particles [59] . Now at first, we would like to explore whether we can see a similar velocity correlation in an active-passive mixture.

3.4 Mixture of active and passive particles

In this section, we demonstrate that long-range velocity correlation can also be observed in a mixture of active and passive particles. As mentioned in the model section, for this we consider active particles with area fraction ϕ_a and passive particles with area fraction ϕ_p in a fixed box of size L. Earlier studies have shown mixtures of active and passive particles can exhibit non-trivial dynamical behavior *e.g.* as shown in Chapter 2, at lower densities, the active particles can affect the dynamics of the passive particles. Apart from the transport properties, there have been other studies involving phase separation [115], fluidization of glassy systems [116], effective depletion-like attractions between passive particles in an active particles medium [98, 117, 118], crystallization of colloidal systems promoted by doping with self-propelling particles [119, 120], and mesoscale turbulence mediated by passive particles [121] to name a few. However, to the best of our knowledge, there is no study yet that addresses the velocity correlation of an active-passive mixture in the dense limit.

For a purely active systems, as we showed in the previous section, a sufficiently high density is required to first initiate phase separation and then in the phase separated state it has been shown to increase with increasing density (see figure. 3.7). To explore similar effects in a mixture, we combined active and passive particles with different area fractions and examined the velocity correlation in the same way as before. Remarkably, as shown in figure 3.8, a similar effect is present in the active/passive mixtures even at low active particle fractions (~ 0.12) but only at high densities of passive particles. In figure 3.8, one can see that for a smaller area fraction of both active and passive particles, the system remains in a homogeneous state and there is practically no
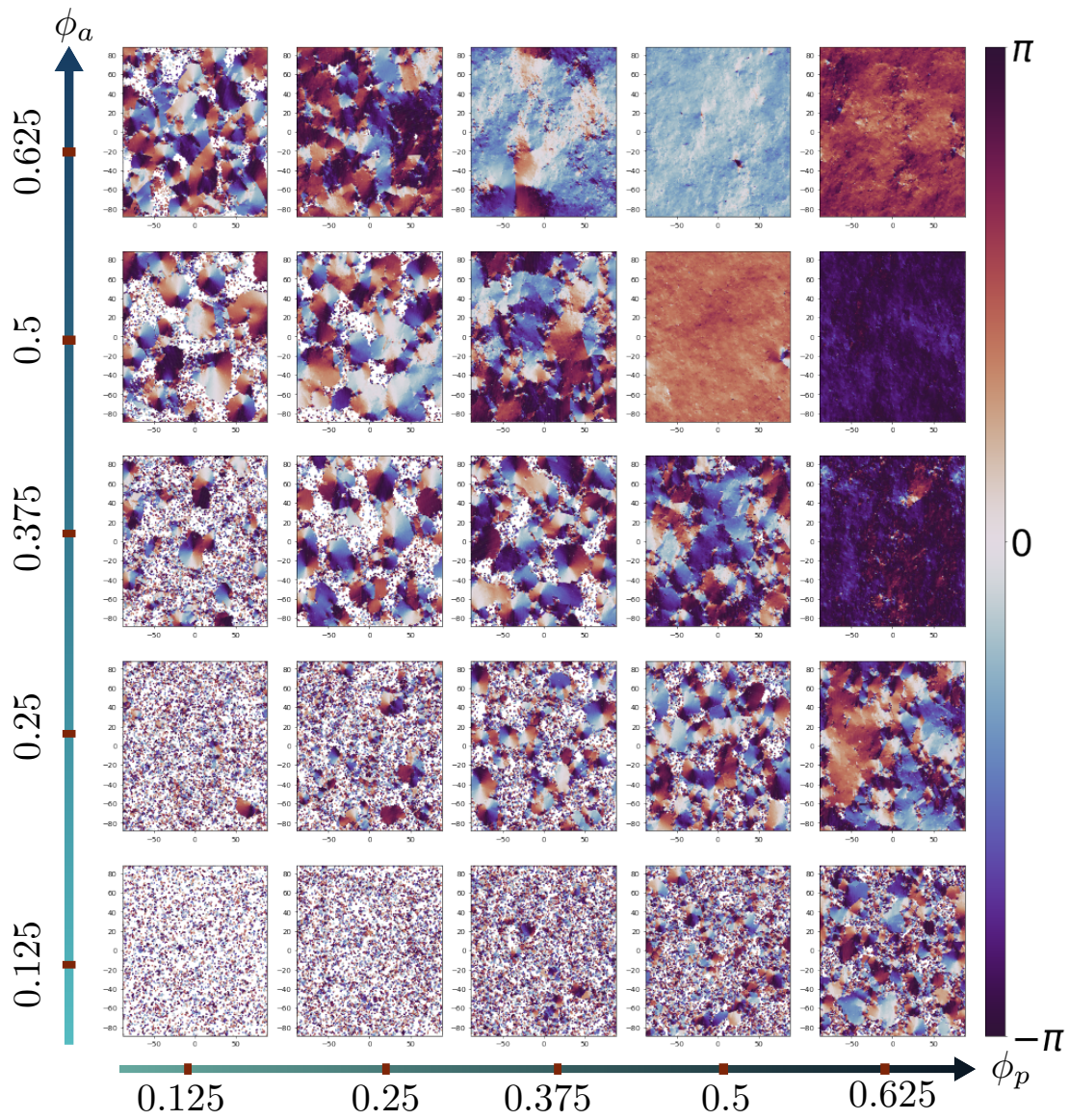
Figure 3.8 – *Configuration of the system for the different area fractions of active, ϕ_a and passive ϕ_p particles. Colors encode the velocity direction of particles in the system.*

Figure 3.9 – *Configurations of the system for different area fractions of passive particles ϕ_p at $\phi_a = 0.01$. Panel (a): at $\phi_p = 0.15$ the system remains in homogeneous state. Panel (b): at $\phi_p = 0.5$ small domains with velocity ordering emerges. Panel (c): at $\phi_p = 0.75$ the velocity correlated domain are quite large. Panel (d) at $\phi_p = 0.99$ the whole system becomes correlated in terms of velocity orientation.*

detectable signs of velocity correlation. As the area fraction of either of the components starts to gradually increase, the average size of domains with aligned velocities grows until the size of the domains with aligned velocity reaches the system size when the box is almost full ($\phi_{\text{tot}} \sim 0.90$).

Now, from the snapshots shown in figure. 3.8, it is clear that a mixture of active and passive particles can also show strong velocity correlation as observed in a pure active system. The question that naturally arises here is how far we can go by varying the relative densities of each component before the strong correlation disappears. In other words, would we see a similar effect in a mostly passive system just by adding a very small number of active particles? In the next section, we would like to answer this question.
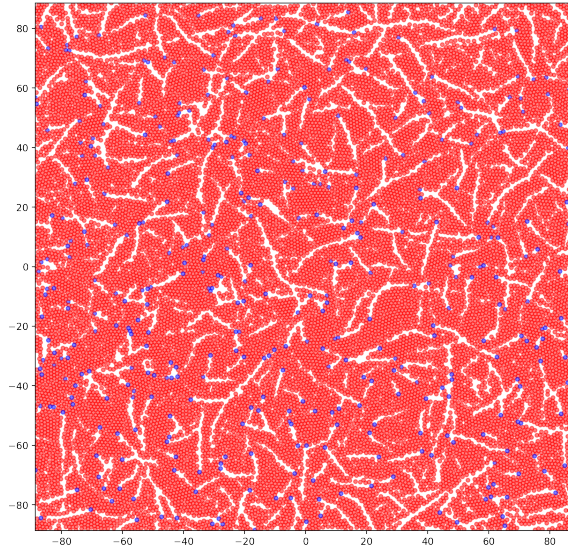
Figure 3.10 – *Configuration of a system with $\phi_p = 0.5$ and $\phi_a = 0.01$. Active particles
(blue particles) make their own path (white area) among the passive particles (red
particles) by ploughing through the passive medium.*

3.5 Velocity correlation between passive particles in the presence of active dopants

We consider a very small area fraction ($\phi_a \sim 1\%$) of active particles with fixed box
size and keep adding passive particles to the system (see figure 3.9). As we increase
the area fraction of passive particles, when $\phi_p \sim 0.2$ the system still remains in the
homogeneous state and the active particles navigate freely in the medium without
causing any velocity correlation (see figure 3.9(a)). However, as the area fraction of
passive particles reaches ~ 0.5, the excluded volume interaction starts to play a role, so
that the interaction over short distances becomes important, and small domains with
aligned velocity emerge in the system. However, these domains do not grow and mostly
remain finite in size. Notably, it can be observed that the active particles also make
their own path among the passive particles (see figure. 3.10) by ploughing through the
passive medium [122, 123].

As we continue to increase the area fraction of the passive particles, we see an

Figure 3.11 – *Panel (a). The correlation as a function of distance r between particles for different area fraction of passive particles at fixed area fraction of active particles $\phi_a \sim 0.01$. Panel (b) The correlation length obtained from fitting $C(r)$ in the panel (a) as a function of area fraction of passive particles.*

increase in the average size of domains with aligned velocities (see figure 3.9 (c)) which means active particles start to push passive particles to move together coherently. Finally, when the area fraction of passive particles in the system reaches $\phi_p \sim 0.99$, the whole system becomes correlated (see figure 3.9 (d)).

To quantify this spectacular strong velocity ordering, we calculate the velocity correlation in the system as a function of distance. As can be seen in the figure 3.11 (a), the velocity correlation grows continuously. As the area fraction of passive particles increase and after reaching $\phi_p \sim 0.85$ the entire system becomes correlated. In figure. 3.11(b) it is demonstrated that velocity correlation increases slowly with the density of passive particles at moderate density and then very rapidly as the density of passive particles exceeds ~ 0.85, which is close to the threshold density for solidification.

(a)

(b)
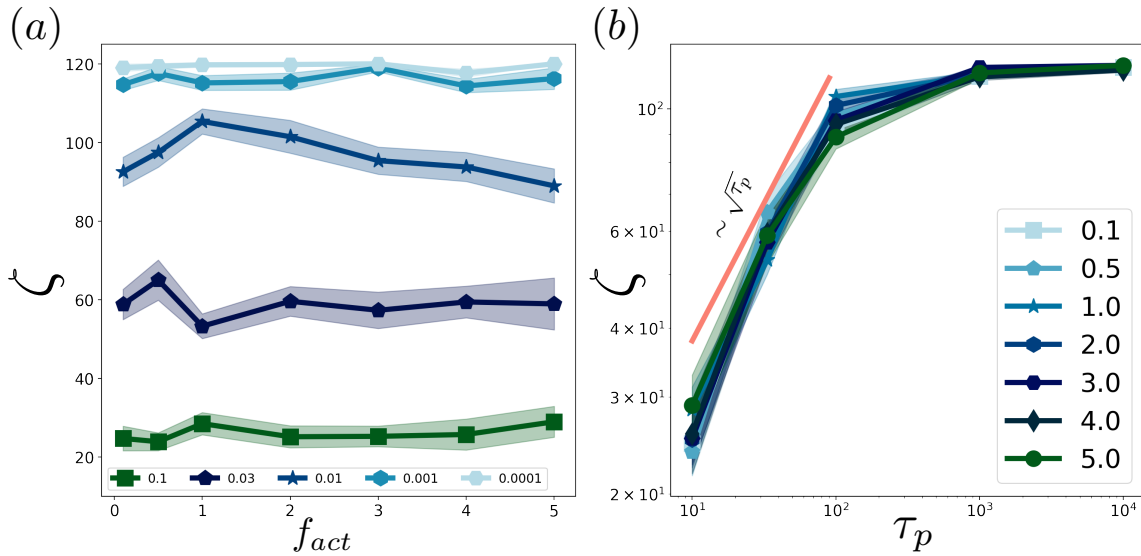
Figure 3.12 – *Panel(a): the correlation length as a function of self-propulsion force (f_{act}) for different rotational diffusion values. Panel(b): the correlation function as function of persistence time $\tau_p = 1/D_r$ for different self-propulsion force values.*

3.6 Effect of persistence time and active force on the velocity correlation

After observing that velocity correlation can be generated in a dense passive system in the presence of a small fraction of active particles, we now ask how the correlation depends on activity parameters like the self-propelling force f_{act} and the rotational diffusion coefficient $D_R = 1/\tau_p$. As can be seen in the figure 3.12, the correlation length for a fixed value of the rotational diffusion is almost unchanged when one alters the active forcing f_{act}. However, as the rotational diffusion decreases, corresponding to an increase in the persistence time, the correlation length increases for a fixed value of the self-propelling force. This means that rotational diffusion plays a very important role in developing the velocity ordering in the system. When the rotational diffusion constant decreases, the correlation length increases almost for all self-propulsion forces regardless of their strength and it increases as the square root of the persistence time

of the self-propulsion. Outstandingly, this is in agreement with the results obtained by Caprini [59] , Henkes [60] and Szamel [61]. Moreover, after the rotational diffusion reaches 0.001, the whole system becomes correlated in terms of velocity alignment. This means that we can have a correlated system of non-motile particles just by adding only a very small fraction of active particles and the degree of such velocity ordering can also be manipulated by controlling the activity parameters such as τ_p.

3.7 Conclusion

In summary, we have looked at the physics of velocity correlation in a mixture of active and passive particles. First, we gave a brief review of the recent work [59–61] that has reported a 'hidden' spontaneous velocity correlation in motility-induced phase separation in both active solid-like and liquid-like systems. They have shown that there are two indispensable elements for the formation of such a strong and strong velocity correlation, namely (a) a high density of self-propelled particles and (b) a high persistence time of the self-propulsive force. We extended this study to a dense passive system with a small fraction of active particles, to investigate whether we can decouple the effect caused by the high density from that caused by the activity or persistence time of active particles.

We first explored a pure active system and identified a sufficiently high density required to see the velocity correlation in the system. We then combined active and passive particles with different area fractions and investigated the velocity correlation in the same way as before. Most interestingly, we demonstrated that a similar effect can be seen even for a low fraction ($\phi_a \sim 0.125$) of active particles at a high density of passive particles.

Then, we considered a very small fraction of active particles ($\phi_a \sim 0.01$) in fixed box size and kept adding passive particles to the system. We found that at intermediate

area fraction of passive particles, active particles make their own path among the passive particles by ploughing through the passive medium. Notably, the average size of velocity-correlated regions grow rapidly with the density of passive particles which results in global correlation in the system. In short, the velocity correlation can be generated in a passive system by doping of active particles as long as the passive medium is dense enough.

We finally investigated the dependence of the activity parameters such as self-propulsion force f_{act} and rotational diffusion $D_r = \frac{1}{\tau_p}$ on the correlation in the system. It turned out that for fixed values of rotational diffusion, the correlation length is almost unchanged when one changes the active force. On the other hand, for a fixed value of f_{act} with decreasing rotational diffusion, the correlation length grows and scales with the square root of the persistence time which is in agreement with the purely active systems [59–61]. The insight from our study suggests that such exotic velocity correlations can be generated in experiments by doping a small fraction of active Janus particles in a dense suspension of passive colloids.

Chapter 4

Effects of direction reversals on patterns of active filaments [1]

4.1 Abstract

Active matter systems provide fascinating examples of pattern formation and collective motility without counterpart in equilibrium systems. Here, we employ Brownian dynamics simulations to study the collective motion and self-organization in systems of self-propelled semi-flexible filaments, inspired by the gliding motility of *Cyanobacteria*. Specifically, we investigate the influence of stochastic direction reversals on the patterns. We explore pattern formation and dynamics by modulating three relevant physical parameters, the bending stiffness, the activity, and the reversal rate. In the absence of reversals, our results show rich dynamical behavior including spiral formation and collective motion of aligned clusters of various sizes, depending on the bending stiffness and self-propulsion force. The presence of reversals diminishes spiral formation and

---

reduces the sizes of clusters or suppresses clustering entirely. This homogenizing effect of direction reversals can be understood as reversals providing an additional mechanism to either unwind spirals or to resolve clusters.

4.2   Introduction

Active matter is a class of systems that are inherently out of equilibrium through coupling to an internal process of energy consumption that results, for example in self-propulsion or growth [10, 12]. Specifically, the case of self-propelled active particles has received much attention in recent years, as it gives rise to intriguing dynamics and mechanical behaviour at the collective level. Such systems are ubiquitous in nature, examples include the cytoskeleton [1–3], swarming bacteria [4–6], tissues [69] ,and biofilms [68]. Finding suitable tools to study active matter systems is a challenge for non-equilibrium statistical physics in order to elucidate the dynamical behavior and the physical properties of these systems.

Self-propelled particles self-organize into macroscopic structures with collective dynamics like clustering, swarming, and swirling. This type of dynamical pattern formation has been subject to intensive research in recent years, both from a theoretical or computational viewpoint [39, 45–47, 124–134] and experimentally [55, 75, 135–140], often using systems of bacteria either swimming in a solution or gliding on surfaces as well as synthetic self-propelled particles systems [141].

On the theoretical side, most studies of collective effects in systems of self-propelled particles have considered either spherical or point-like particles [39]or short and rigid rod-like particles, as these are good approximations for the shape of the bacteria typically used in experiments such as swimming *Bacillus subtilis* or *Escherichia coli* [126, 133, 139] and as *Myxococcus xanthus*, gliding on surfaces [137]. The aspect ratio of rod-like particles has a strong impact on the patterns, as high aspect ratios promote

(nematic) alignment of the particles and swarming [62].

At very large aspect ratios, the the finite rigidity of the particles is expected to play a role. Therefore several computational recent studies have addressed semi-flexible filamentous particles or self-propelled polymers [47, 127]. Indeed, their collective behavior is modulated by their bending rigidity. Moreover, flexibility even results in new single-filament behavior, as individual flexible filaments are seen to curl into spirals due to their self-propulsion [46].

Complicating the understanding of the behavior of the collective motion of microbes, many of them in addition to active self-propulsion also perform active directional changes such as the well-known run-and-tumble motion of *Escherichia coli* [142]. Typically, these active direction changes are an integral part of the mechanisms for chemotaxis and other types of tactic behaviors, through a coupling of the rates of directional change to the direction of motion relative to a (chemical, light, etc.) gradient direction. Such active directional changes have occasionally been included in models for the motility and collective behavior of self-propelled particles [130, 143–145] or spreading of active polymers in porous media [146]. For bacteria, the simplest direction change in a reversal, where the whole filament reverses its direction of motion by 180°, as seen in the gliding motility of *M. xanthus*, a short rigid rod [137], as well as in gliding filamentous *Cyanobacteria* [147, 148].

In this article, we use extensive simulations to address how such reversals affect the collective behaviors of self-propelled semi-flexible filaments at overall relatively low density. To that end, we first consider the reference case without reversals and analyze the formation of spirals and swarms or clusters,

With that in mind, in this paper, we initially examine the self-assembly of active filaments by modulating the bending stiffness and self-propulsion force of the filaments, and then investigate how the introduction of reversals modifies the collective behavior.

We focus on the interplay of the filaments' self-propulsion force, bending stiffness, and reversal rate as the control parameters that modulate the pattern formation process. In the absence of reversals, the filaments form spirals for high self-propulsion force and low bending stiffness, for larger bending stiffness coherently moving clusters dominate the system. Introducing reversals reduces the rates for forming both types of patterns and thus the system becomes gradually more isotropic with increasing reversal rate. Both negative effects can be explained by the dynamical pathway of these structures: First, reversal adds a second mechanism that interrupts the spooling of the filaments and initiates unwinding. Second, a new mechanism is added for filaments to leave a cluster, since filaments typically leave a coherently moving cluster during a reversal.

4.3   Model

4.3.1   Self-propelled filaments

We consider a system of N_c self-propelled semi-flexible filaments. The individual filament is described as a chain of N monomers located at position s $(\boldsymbol{r}_1, \boldsymbol{r}_2, \cdots, \boldsymbol{r}_N)$ in space (see Fig. 4.1 (a) for a schematic). Two consecutive monomers in the chain are connected by a harmonic spring. In addition, the angle between three consecutive monomers along the chain are subject to a harmonic bending potential, which controls the flexibility of the chain. In the over-damped regime, the equation of motion for each monomer can be written as:

$$\zeta \dot{\boldsymbol{r}}_i = -\nabla_i U_s - \nabla_i U_b + \boldsymbol{F}_i^a + \boldsymbol{F}_i^{ex}. \tag{4.1}$$

where $\dot{\boldsymbol{r}}_i$ is the velocity of the i-th monomer, ζ is the friction coefficient. The four force contributions on the right hand side of this equation represent stretching and bending
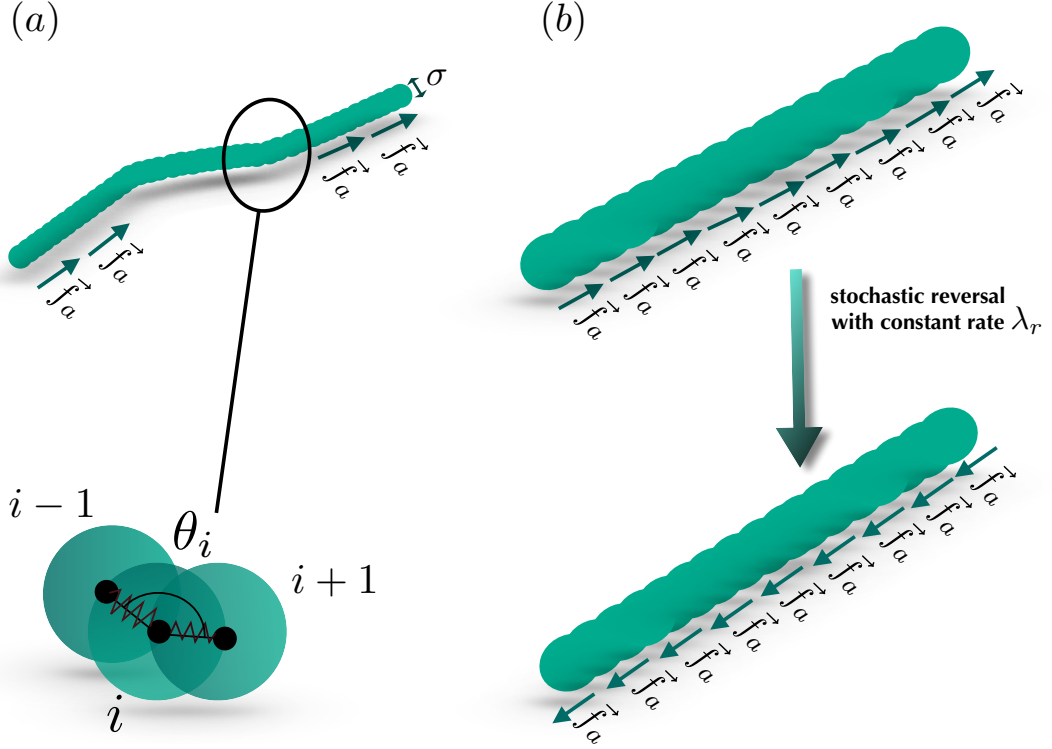
Figure 4.1 – ***Model of a self-propelled filament.*** ***(a)*** *Sketch of a self-propelled filament composed of monomers with diameter σ. The active force inducing their self-propulsion acts tangentially along each bond. **(Zoom)** The flexibility of the chain is modeled by a harmonic bending potential, where θ_i is the angle formed by each successive triplet of monomers $i-1, i, i+1$. **(b)** Sketch of the reversal mechanism of a self-propelled filament: Upon a stochastic reversal with rate λ, a filament reverses the direction of its self-propulsion force by 180°.*

of the chain, the active force responsible for self-propulsion and volume exclusion, respectively.

U_s is the stretching potential due to the harmonic springs (each with an equilibrium length of r_0 between consecutive monomers) with the form

$$U_s = \frac{\kappa_s}{2} \sum_{j=2}^{N} (r_{j,j-1} - r_0)^2. \tag{4.2}$$

where $r_{j,j-1} = |\boldsymbol{r}_j - \boldsymbol{r}_{j-1}|$ is the distance between the j-th and $j-1$-th monomer and κ_s is the spring constant associated with stretching.

U_b is the harmonic bending potential which controls the flexibility of the bonds. Considering θ_i as the angle formed by a consecutive triplet of monomers $(i-1, i, i+1)$, given by $\theta_i = cos^{-1}\left(\frac{\boldsymbol{r}_{i-1,i}\cdot\boldsymbol{r}_{i,i+1}}{|\boldsymbol{r}_{i-1,i}||\boldsymbol{r}_{i,i+1}|}\right)$, this potential is defined as

$$U_b = \frac{\kappa_b}{2} \sum_{j=2}^{N-1} (\theta_j - \pi)^2. \tag{4.3}$$

where π is the equilibrium angle of between adjacent pairs of monomers, corresponding to a straight chain, and κ_b is the spring constant associated with bending.

The self-propulsion is induced by the active force $\boldsymbol{F}_i^a$,

$$\boldsymbol{F}_i^a = f_a \hat{t}_i, \tag{4.4}$$

where f_a fixes the absolute value of the self-propulsion force and $\hat{t}_i$, the unit vector tangent to the chain at the position of i-th monomer, defines its direction. For a chain consisting of discrete monomers, this vector can be approximated as:

$$\hat{t}_i = \frac{\alpha_c}{2}\left(\frac{\boldsymbol{r}_{i+1,i}}{|\boldsymbol{r}_{i+1,i}|} + \frac{\boldsymbol{r}_{i,i-1}}{|\boldsymbol{r}_{i,i-1}|}\right). \tag{4.5}$$

Here $\alpha_c \in \{-1, +1\}$ specifies the state of the polarity (head-tail) for each chain $c \in \{1, \cdots, N_c\}$ where N_c is the number of chains in the system. This variable will be important for the modelling of reversal events, as we will discuss below.

Finally the presence of the repulsive force $\boldsymbol{F}_i^{ex}$ prevents overlaps of the monomers. Such volume exclusion is implemented using the Week-Chandler-Anderson potential:

$$U_{ext}(r) = \begin{cases} 4\epsilon\left[\left(\frac{\sigma}{r}\right)^{12} + \left(\frac{\sigma}{r}\right)^6\right] + \epsilon, & r < 2^{1/6}\sigma \\ 0, & \text{otherwise} \end{cases} \tag{4.6}$$

where σ is the nominal interaction diameter and ϵ is the energy scale of the interaction.

In addition, adjacent monomers in the filament overlapped, resulting in a smooth filament and $r_0 = \sigma/2$

4.3.2 Direction reversals

So far, our model agrees with previous models for self-propelled filaments [46, 47, 127]. In addition, we include spontaneous reversals of the direction of self-propulsion, as they are often seen in the surface motion of bacteria [146, 149] including filamentous species such as gliding filamentous *Cyanobacteria* [150–152]. Typically, the rates for such reversals are modulated by various tactic behaviors such as chemotaxis, phototaxis, etc. Here we consider the baseline case of spontaneous reversals in a homogeneous environment.

We model random reversal events, where the gliding direction of a chain changes instantaneously by 180deg, as generated from a Poisson process with a reversal rate λ_r (see Fig. 4.1b). Mathematically, this means that the polarity (head-tail) state α_c of a chain c follows a stochastic process

$$\alpha_c = 1 \quad \overset{\lambda_r}{\underset{\lambda_r}{\rightleftharpoons}} \quad \alpha_c = -1. \tag{4.7}$$

In such a Poisson process, the distribution of waiting times τ elapsed between two consecutive reversals is an exponential distribution of the form

$$P_{\mathrm{w}}(\tau) = \lambda_r e^{-\lambda_r \tau}. \tag{4.8}$$

Hence to implement the reversals for a single chain, we draw a random waiting time τ_0 from the exponential distribution described in Eq.4.8 at time t_0 . Between t_0 and $t_1 = t_0 + \tau_0$, the chain evolves following Eq. 4.1. At t_1 the gliding direction of the chain is reversed and another waiting time τ_1 is drawn from the same waiting time

distribution. This process is done for each chain independently during the simulation by drawing subsequent time intervals $\tau_2, \tau_3, ...$, such that reversals of any chain in the system is uncorrelated with the reversal of any other chains.

4.3.3   Simulations and parameters

All simulations presented here were run on GPUs using the simulation package HOOMD-blue [153] with custom extensions for self-propulsion and for reversals, which were compiled together with the whole software. The simulation integrates Eq.4.1 over $t = 10^8$ time steps.

In these simulations, lengths are measured in units of the monomer radius σ and the energy unit is $k_B T$. We choose the time unit to be the self-diffusion time for a single monomer $\tau_D = \frac{\sigma^2 \zeta}{k_B T}$ where ζ, which determines the damping, is set to $\zeta = 15$. Our system consists of $N_f = 1666$ filaments each having $N_m = 59$ monomers.

We set the spring constant of the stretching spring to $\kappa_s = 10^4$, *i.e.* to a relatively high value to make sure that chains do not stretch too much along their axis. Hence the distance between two successive monomers does not fluctuate strongly and is approximately constrained to the fixed value r_0. Furthermore, to obtain a smoother filament, we also set the value $r_0 = \frac{\sigma}{2}$. To investigate a large parameter space, we varied κ_b in the range $\{1, 1800\}$ and f_a between $\{1, 100\}$. The packing fraction, $\phi = N_f N_m r_0 \sigma / L^2$, is set to 0.1 in all simulations, where L denotes the box size and $L = 167\sigma$

The aspect ratio, a dimensionless number representing the ratio between the contour length and the diameter of the individual monomers $a = \frac{L_f}{\sigma}$, is set to almost 30 and $L_f = (N_m + 1)r_0$ is the contour length of the filaments. The reversal rates λ_r are varied between $\{0 - 0.1\}$ and are same for all the filaments.

4.4   Results

To address the effect of direction reversals on the collective dynamics of self-propelled filament, we performed systematic simulations varying three key parameters, the bending stiffness κ_b, the strength of self-propulsion f_a, and the reversal rate λ_r. We will show typical snapshots of these simulations below. We start with the case without direction reversals ($\lambda_r = 0$), which has been studied before [47, 127] and which serves us as a reference scenario here. In that case, it is known that a variety of non-equilibrium patterns can be formed, for which we will present a detailed diagram of states below.

Later on, we add the reversal mechanism to the filaments, inspired by the reversal dynamics (due to phototaxis) observed in *Cyanobacteria* to investigate the response of the system to an abrupt and random reversal in gliding direction. We report a dramatic change in the individual as well as collective dynamics in the state diagram as we crank up the reversal rate eventually destroying the spiral state completely.

4.4.1   Non-reversing active filaments

4.4.1.1   Spiral formation

In the absence of direction reversals, the collective dynamics of the chains is dominated by the interplay between self-propulsion, bending stiffness and confinements due to the excluded volume effect. A key observation at low density of filaments is that flexible filaments may form spirals while stiffer filaments tend to form clusters [47, 127].

Spirals form due to the self-interaction of an isolated active filament with high self-propulsion and low bending stiffness. Spiral formation stands in contrast to the relatively straight equilibrium structure of a semi-flexible filament and depends on the self-propulsion. Spiral formation is initiated when the head of the filament collides with a subsequent part of its own body, such that excluded volume interaction force
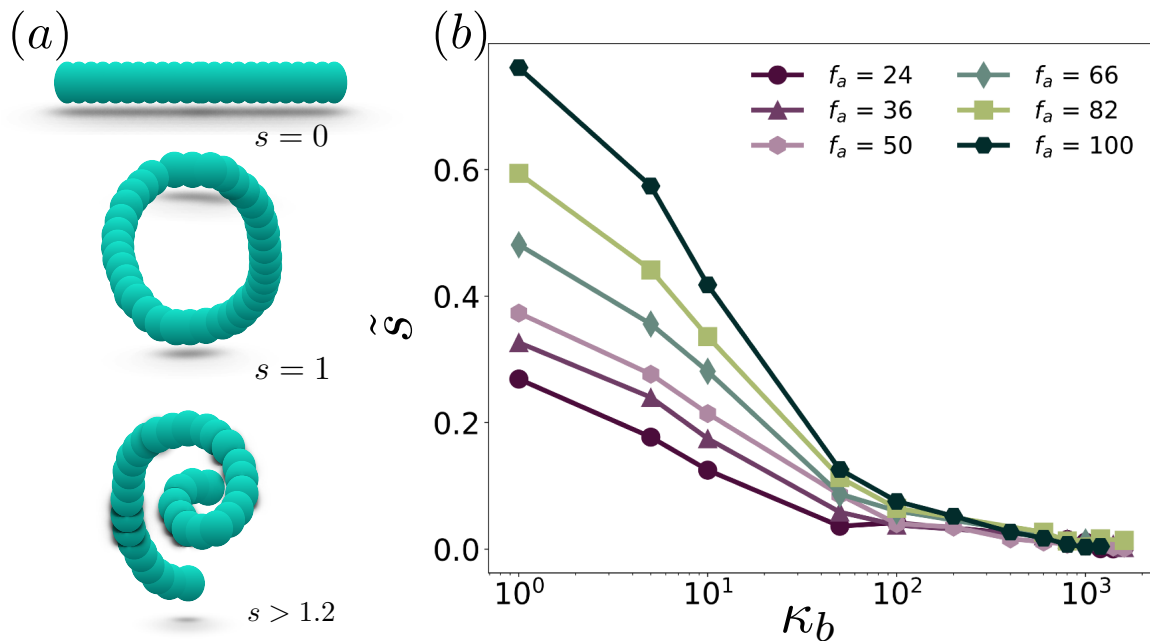
Figure 4.2 – *Spiral ratio as a function of bending stiffness for different values of self-propulsion force.* *(a) Sketch of different configuration of a single filament characterised by the indicated spiral number indicated by s. (b) Quantification of spiral formation by the spiral ratio $\tilde{s}$: An increase in bending stiffness decreases the probability of spiral formation at a constant self-propulsion force. Different values for self-propulsion are shown in different colors. With increasing self-propulsion force at low bending stiffness, spiral formation is promoted. For high bending stiffness, spiral formation does not take place regardless of the self-propulsion force. The aspect ratio of the filaments is $a = 30$ and the packing fraction is $\phi = 0.1$.*

the filament to wind onto itself. If the self-propulsion is strong enough, filaments twist around their own body through this mechanism and form stable spirals. To characterise the dynamical state with spiral formation we define a spiral number for each filament in the system which quantifies how many times a filament is wound up around itself and is defined as:

$$s = \left| \frac{\sum_{i=2}^{N-2} \Delta\theta_i}{2\pi} \right| \tag{4.9}$$

where θ_i is the angle formed by the beads $i-1, i, i+1$. $|..|$ denotes the absolute value of the spiral number since they can be twisted either in the clockwise or counterclockwise direction. $s = 0$ indicates an almost straight configuration (see Fig. 4.2 (a)) and $s = 1$
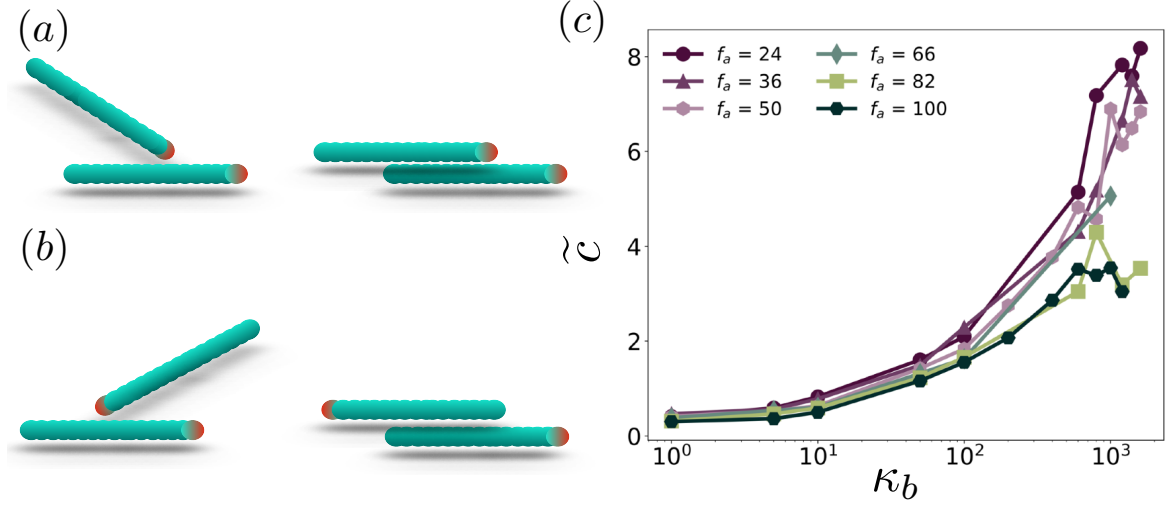
Figure 4.3 – *Cluster ratio as a function of bending stiffness for different values of self-propulsion force. (a) A binary collision of self-propelled filaments that results in parallel alignment and coherent motion that initiates cluster formation. (b) A binary collision of self-propelled filaments that results in anti-parallel alignment and transient coherent motion. The red monomer shows the head of the filament in both cases. (c) Increasing the bending stiffness promotes cluster formation in the system. Different values for the self-propulsion force are shown in different colors. The aspect ratio of the filaments is $a = 30$ and the packing fraction $\phi = 0.1$.*

a ring shape (see Fig. 4.2 (a)). We consider a filament to be in a spiral state if $s \geq 1.2$ (see Fig. 4.2(a)).

To distinguish global patterns of filaments, we introduce the spiral ratio as the ratio of the number of filaments in the spiral state (i.e., with $s \geq 1.2$), N_s, to that in the straight configuration, N_{sf}:

$$\tilde{s} = \frac{N_s}{N_{sf}}. \tag{4.10}$$

The spiral ratio is plotted in Fig.4.2(b) as a function of the bending stiffness and the self-propulsion force. The figure shows a pronounced decrease of the spiral ratio with increasing bending stiffness, which reflects the fact that increasing bending stiffness (κ_b) hinders the self-interaction needed for spiral formation. Fig.4.2(b) also shows that, for fixed bending rigidity, spiral formation is promoted by an increase in the self-propulsion force.

4.4.1.2   Cluster formation

In the limit of high bending stiffness, filaments behave like rod-shaped agents. In this regime, filaments move in the direction of their long axis direction and when they undergo collisions, they rotate to align due to their steric interaction. At high bending stiffness, collisions between filaments are dominant over self-interactions as the bending required for the self-interaction is unfavourable. Dependent on the angle of incidence in the collision event the two filaments align either parallel or anti-parallel (Fig. 4.3(a) and (b), respectively). In the first case, they continue their motion together, in the second case, they stay in contact transiently [10, 130]. Clusters of filaments form when additional filaments collide with already aligned filaments, resulting in groups of filaments that move coherently. The size and life-time of these clusters depends on bending rigidity, activity as well as the density of the filaments in the system [10, 62, 133].

To characterise the clustering behaviour we identify clusters using the following criteria: two monomers are considered to be part of the same cluster if their centers are distanced less than 1.2σ. We note that this criterium automatically includes all monomers of one filament in the same cluster. In addition, we only considered clusters with at least $N_f = 10$ filaments to avoid counting micro clusters. Clusters are identified with the data analysis framework Freud [105]. Finally, in analogy to the spiral ratio, we define a cluster ratio as the ratio of number of filaments in clusters, N_c to the number of free filaments, N_f.

$$\tilde{c} = \frac{N_c}{N_f} \tag{4.11}$$

Fig. 4.3 shows the cluster ratio as a function of the bending stiffness for different values of the active force. The cluster ratio is seen to increase monotonically with increasing bending stiffness (κ_b) and also with increasing self-propulsion force. One can
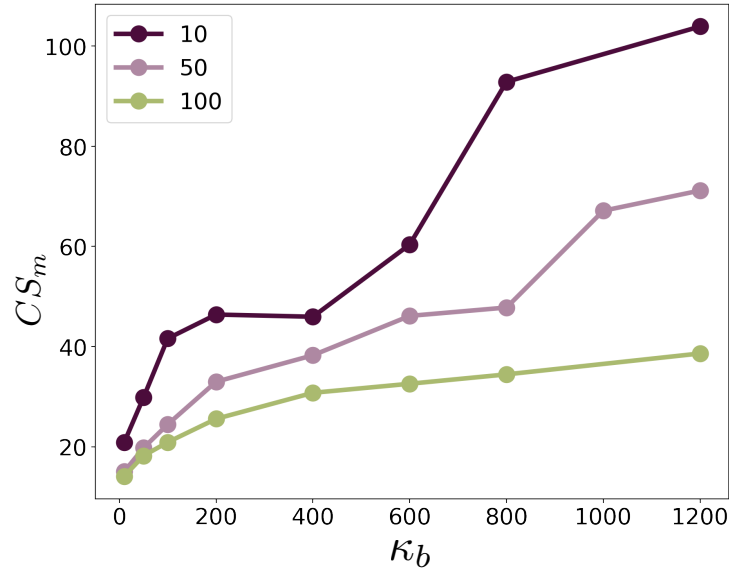
Figure 4.4 – ***Average cluster size as a function of bending stiffness***. *The average cluster size is shown in different colors for different self-propulsion forces.*

also see that high values of the spiral number are associated with small clusters and vice versa: the regions with higher values of spiral ratio in Fig. 4.2 correspond to the region of low cluster ratio in Fig. 4.3. When the bending stiffness is low, spirals are formed due to the self-interaction, when the bending stiffness increases, the deformation of the filaments becomes unfavorable, which is why they usually have a straight, rod-like conformation that promotes alignment and, thus, clustering.

We also define the average cluster size, CS_m, which is the average total number of filaments belonging to clusters and this seems to increase with increasing bending stiffness indicating (see Fig. 4.4) the fact that bending stiffness which suppress spiral formation, promotes clustering.

Since both spiral ratio and cluster ratio show opposing trends as function of the bending rigidity and of the self-propulsion force, we wondered whether the results could be written as functions of a dimensionless parameter combination. A natural candidate is the flexure number, the ratio of activity and bending rigidity [47, 127, 154,
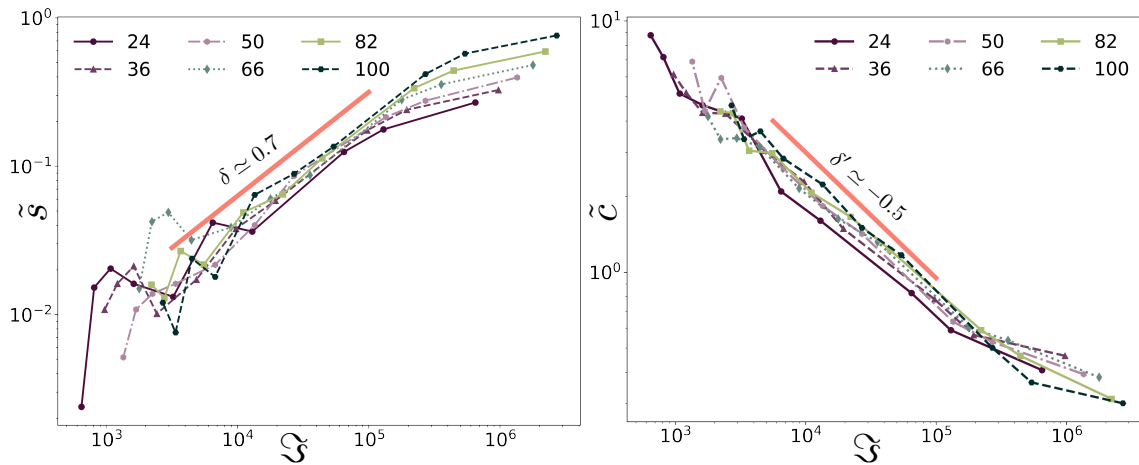
Figure 4.5 – *(a) Spiral ratio $\tilde{S}$ and (b) cluster ratio $\tilde{C}$ as functions of the flexure number $\Im$: Data collapse for different self-propulsion forces and bending rigidities when these are plotted as functions of a dimensionless combination, the flexure number. The color of the points indicates the value of the self-propulsion force. The red lines indicate power laws fitted to the curves, with exponents δ and δ'.*

155] can be written as:

$$\Im = \frac{f_a L^3}{\kappa_b} \tag{4.12}$$

Figure 4.5 shows the spiral and cluster ratio as functions of the flexure number. Indeed the data from simulations with different bending stiffness and self.propulsion forces are seen to collapse onto one curve. Only for the largest flexure numbers, we see systematic deviations for the spiral ratio. For smaller values of the flexure number, the spiral ratio increase as a power law $\tilde{S} \sim \Im^{\delta}$ with $\delta \simeq 0.7$. Likewise, the decrease of the cluster ratio also follows a power law $\tilde{C} \sim \Im^{\delta'}$ with $\delta' \simeq -0.5$.

4.4.1.3 State diagram

We performed systematic simulations varying the self-propulsion force f_a and the bending stiffness κ_b to explore the variety of patterns in the steady state of the system.

To distinguish different states of the system, we assign a state to all filaments in a snapshot via the following criteria: A filament is considered as a spiral if its spiral number is < 1.2. The filament is taken to be in the cluster category if it is not a
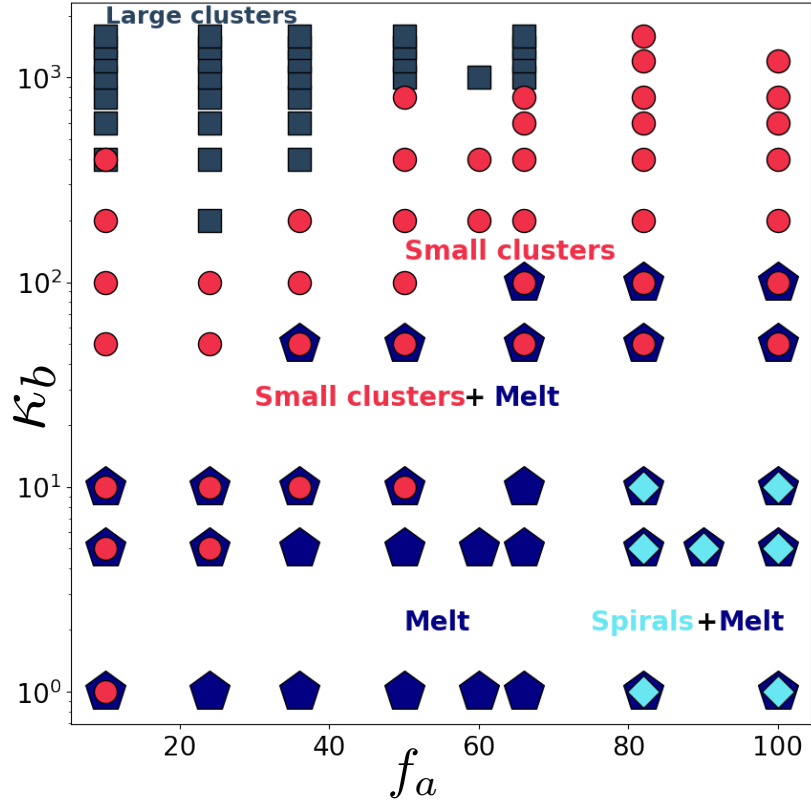
Figure 4.6 – *Non equilibrium state diagram of non-reversing self-propelled filaments.* *The state diagram is drawn as a function of self-propulsion force f_a and the bending stiffness κ_b in the absence of reversals. The different states are indicated by different symbols and the color of each symbol is matched to the corresponding designation of the state. For details on the characterisation and identification of the states, see text.*

spiral and part of a cluster of ≥ 10 filaments. Since this criterion does not capture the diversity of cluster patterns, we further subdivide the cluster state by the size of clusters and distinguish a small-cluster category for filaments in clusters with size ≥ 10 and < 100 and a large-cluster category for filaments in clusters with ≥ 100 filaments. All other filaments are considered to be in the melt state.

Using this classification and averaging over 200 snapshots per condition, we classify the state of the whole system as follows: We classify the system's state as a large-cluster state or as a small-cluster state if $\geq 40\%$ of the filaments are in large or small clusters, respectively. As the two criteria are not mutually exclusive, coexistence of small and
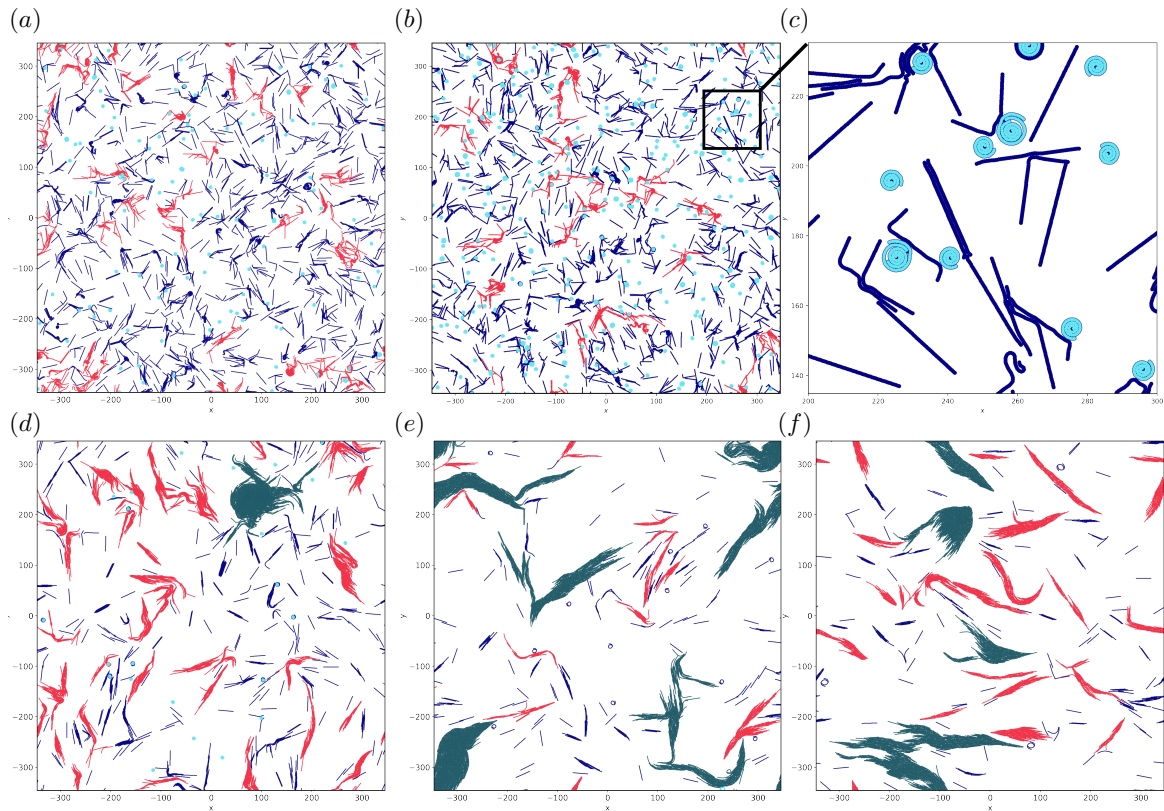
Figure 4.7 – *__Snapshots of the simulation for different__ f_a __and__ κ_b. __(a)__ snapshot for $\kappa_b = 10$, $f_a = 10$ in 'melt' state __(b)__ $\kappa_b = 5$, $f_a = 100$ in spiral+melt state __(c)__ Close-up view of spirals in plot (a) __(d)__$\kappa_b = 600$, $f_a = 82$ __(e)__ in small-cluster state $\kappa_b = 1000$, $f_a = 24$ __(f)__ in large-cluster state $\kappa_b = 1600$, $f_a = 10$ in large + small cluster state.*

large clusters is identified if both are satisfied simultaneously. Likewise, a spiral state is identified when more than 20% of the filaments form spirals (the threshold is chosen lower than for the other states, as under the conditions simulated here, we ever see 40% of the filaments being spirals). Finally, the system state is classified as a melt state if $\geq 40\%$ of the filaments fall into this category. Just like for small and large clusters, coexistence of other states is possible and indeed seen frequently, e.g. between melt and small clusters and melt and spirals. The diagram of states shown in Fig. 4.6 summarizes this classification. Simulation snapshots corresponding to the different states are shown in Fig. 4.7, where the color code of the filament shows the classification at the filament level.

For low bending stiffness and low self-propulsion force, the filaments are mostly in the melt (or isotropic) phase and move in all directions, as can be seen in Fig. 4.7 (a). We note that while the melt filaments are dominant, there are also some small clusters. Increasing the self-propulsion force, while the bending stiffness is kept at a small value, promotes spiral formation, as shown in Fig. 4.7 (b) and (c). Formation of spirals is quite natural in this regime because the filaments are flexible enough to bend onto themselves. Their self-propulsion then results in spiral formation and, once formed, a spiral is typically stable until another filament collides with it.

Collisions with other filament seems to be the dominant (if not only) mechanism that breaks up spirals, since we have not included explicit translational or rotational noise in our simulations. Under the conditions we simulated, the spiral state typically coexists with the melt phase, as casn be seen in the snapshots in Fig. 4.7 (b) and (c). Consistent with this observation, a pure spiral state, the "gas of spirals" reported in earlier studies [47] is only observed at even lower densities than used here.

As shown above (Figure 4.2), the fraction of spirals decreases with increasing bending rigidity. For sufficiently large bending stiffness, collective behavior via the formation of clusters becomes dominant over individual filament dynamics. In this regime, the self-interaction is of lesser importance compared to inter-filament interaction, and when filaments collide, they can bundle into small clusters with local alignment (nematic order). Over time, the clusters grows as other filaments collide with them and join them. At intermediate bending stiffness, there is a coexistence of the freely swimming filaments and small clusters of the filaments (Fig. 4.7 (d)). As we increase the bending stiffness (Fig. 4.6 (d-f)), the clusters become larger and the system state is classified as a large-cluster state, in particular for low self-propulsion force.

These observations show that the collective behavior of filaments is modulated by their bending stiffness and their self-propulsion force. In agreement with earlier work

[47, 127], we distinguish several regimes, characterized by the formation of spirals and of clusters of various sizes. Generally, we observed that, in the absence of direction reversals, filaments with high self-propulsion force and low bending stiffness form spirals, while filaments with high bending stiffness tend to form clusters. This general picture will serve as a reference in the following section, where we will include direction reversals and study how the variation of the reversal rate affects the patterns formed by self-propelled filaments.

4.4.2 Reversing active filaments

Next, we consider active filament that exhibit reversals of their direction of motion. Many microorganism show reversals of their motility direction (in swiming and surface motility), often as part of the (chemo- or photo-)tactic strategy. Here we consider the case of spontaneous, non-biased reversals. Active filaments are taken to change their direction of motion abruptly by 180 °, these reversals occur according to a Poisson process with rate λ_r. Varying the rate of the reversal process, we explored the effect of reversals on the structures and the collective motion of the active filaments.

Fig. 4.8 shows snapshots of the system for two sets of parameters, in both cases without reversals (left) and with a non-zero, but small reversal rate (right). The two parameters sets chosen here correspond to the regime exhibiting spirals ($f_a = 100$ and $\kappa_b = 1$, top) and to the regime dominated by small clusters ($f_a = 24$ and $\kappa_b = 1000$, bottom). In both cases, the patterns are seen to be changed by the introduction of the small reversal rate, indicating a substantial influence of the reversals. In the case of high f_a and low $\kappa - b$, spirals are very frequent in the absence of reversals (although they co-exist with straight filaments). With the reversal rate $\lambda_r = 0.1$, spirals are completely suppressed. In the case of low f_a and high κ_b, the change is less dramatic as collectively moving clusters are seen both in the presence and absence of reversals,
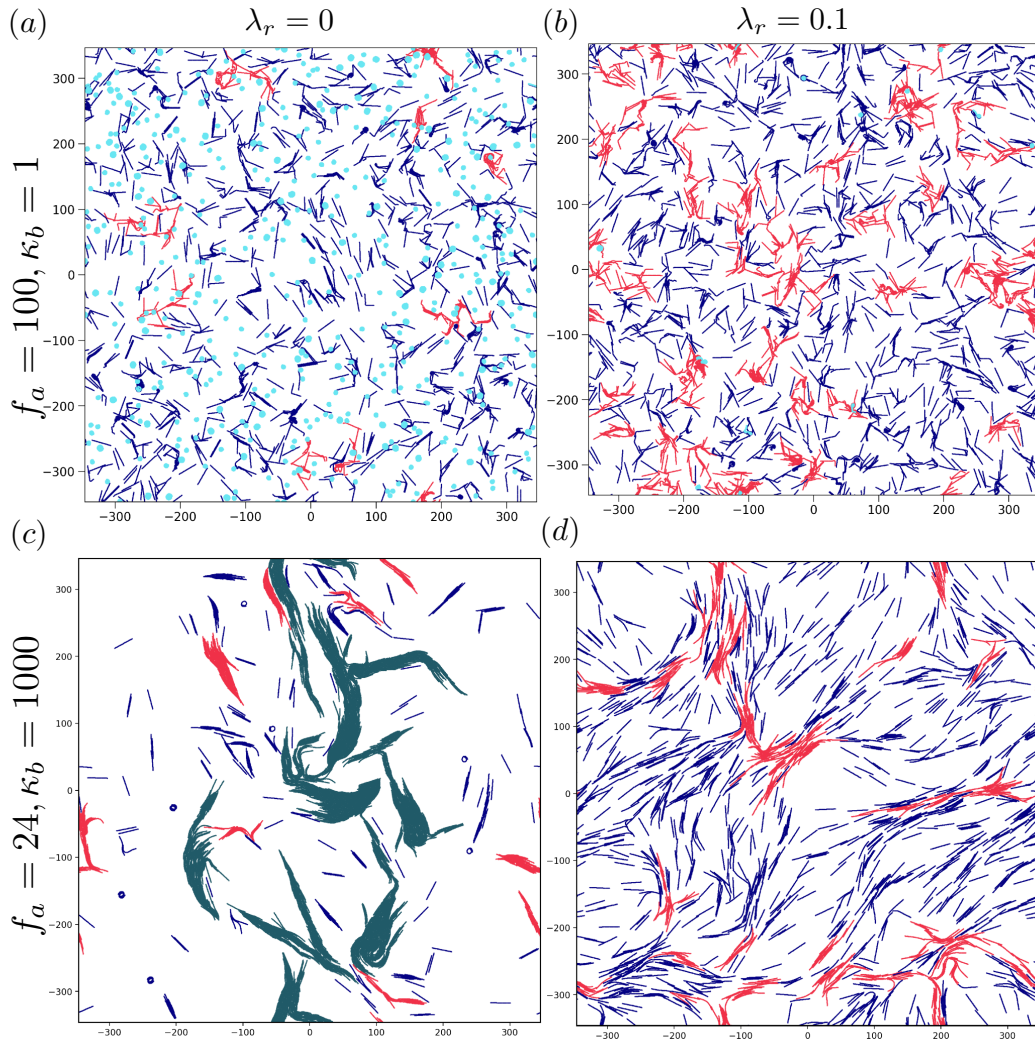
Figure 4.8 – *Snapshot of the simulation with reversal dynamics.* *We show snapshots from the simulations keeping the bending stiffness, activity, density, and aspect ratio same and changing the reversal rate. Applying reversal rate changes the pattern formation drastically from its non-reversing counterpart.* **a,b** *in the presence of a nonzero reversal rate, spiral formation has disappeared.* **c,d** *Likewise, in the presence of reversals, the cluster sizes become smaller than the non-reversing case. The coloring of the filaments indicates their classification as spirals (cyan), filaments in small clusters (red), large clusters (grey) and a melt (blue).*

however, the size of the clusters is considerably decreased by the reversals.
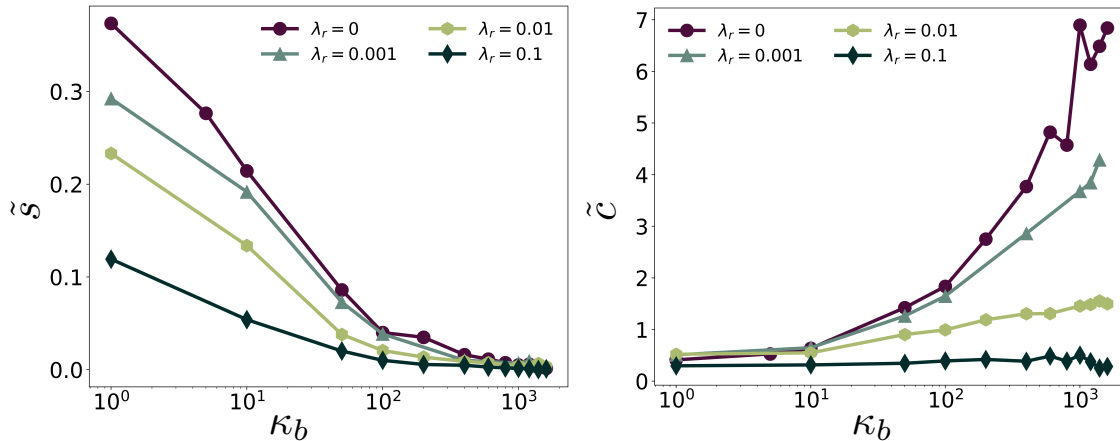
Figure 4.9 – *Spiral and cluster ratio for different reversal rates λ_r at an active force, $f_a = 50$.*

4.4.2.1   Unwinding of spirals and declustering

To quantify these observations, we determined again the spiral and cluster ratio. In Fig. 4.9, we plot the two quantities as functions of the bending stiffness, comparing different reversal rates. These results confirms the qualitative observation from the snapshots: Reversals reduce both spiral formation and cluster formation, for all values of the bending stiffness. Higher reversal rates result in stronger reduction. As these results show a clear reversal rate dependence of the pattern formed by the active filaments, we next investigated the effects of the reversal rate λ_r on the state diagram in the κ_b-f_a space. The results are shown in Fig. 4.10 for four different values of the reversal rate. Already for the smallest reversal rate considered ($\lambda_r = 0.001$), the spiral state as well as the large-cluster state are strongly diminished. Increasing the reversal rate further, also the small-cluster state get pushed towards larger bending stiffness and larger self-propulsion force.

The suppression of spirals is rather straightforward: As mentioned earlier, in the absence of reversals, spirals dissolve through collision with other filaments. Reversals
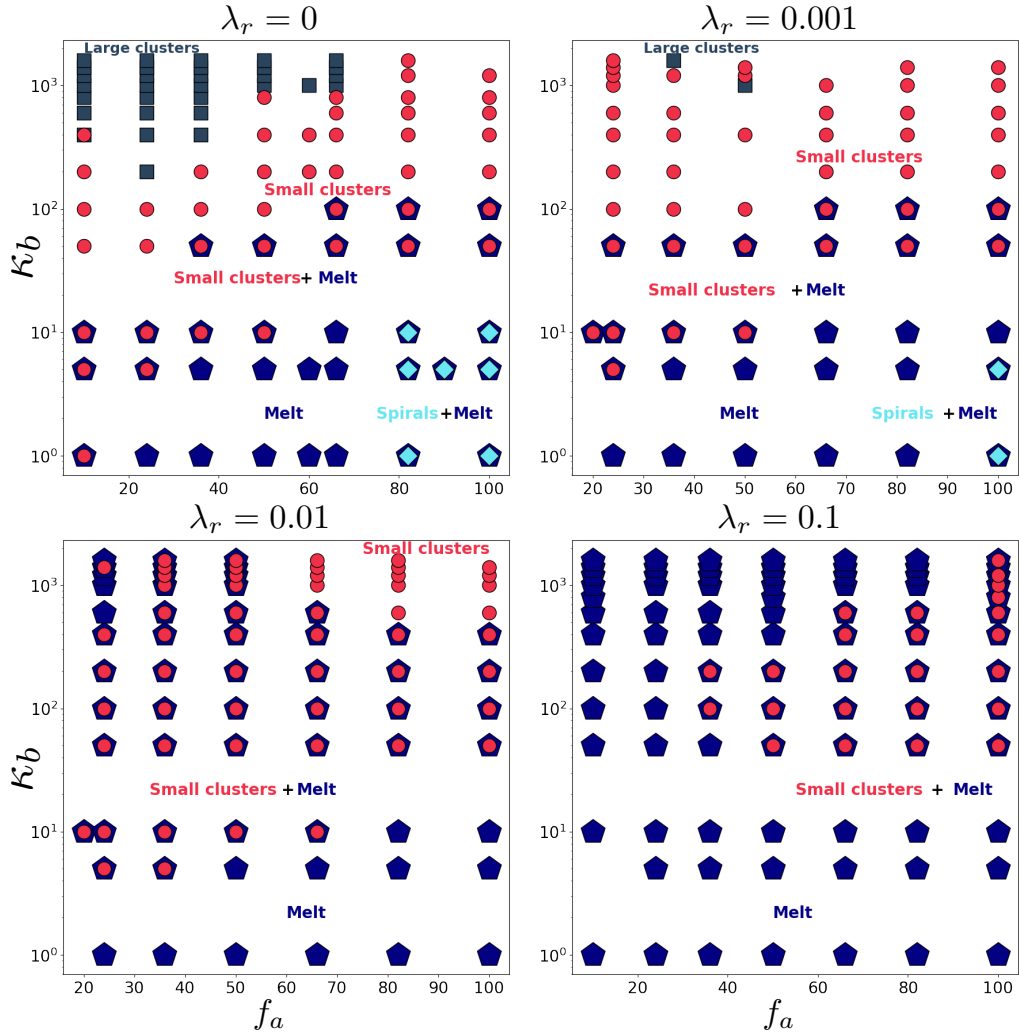
Figure 4.10 – *Diagram of state for reversing self-propelled filaments. The state diagram is constructed as a function of the self-propulsion force f_a and the bending stiffness κ_b and shown for four different values of the reversal rate λ_r. States are marked by different symbols and different colors as in Figure 6. When the reversal rate increases, on the one hand the tendency of formation of large clusters decreases, on the other hand the propensity of spiral formation in the system is progressively suppressed.*

add a second mechanism for breaking up spirals, namely a change in the polarity (head-tail direction) of the self-propelled filaments. When the reversal occurs, the self-propelled filaments is not directed inward in the spiral any more, but rather outward, and thus the spiral unwinds (see Fig. 4.11).

Likewise, reversals add an additional mechanism for filaments to leave a cluster, as
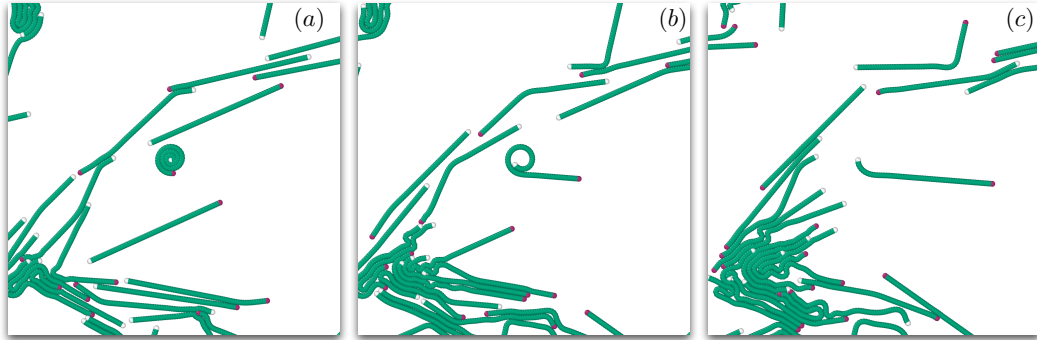
Figure 4.11 – ***Unwinding of a spiral due to the reversal dynamics:*** *Panel (a) shows a filament in the spiral state in the center. In Panel (b) a reversal event takes place. Panel (c): The spiral unwinds and the filament resumes the straight configuration. The white monomer is the head of the filament, the green is the body and the purple is the tail.*

filaments in a cluster typically move collectively in one direction, so that any filament that reverses is likely to move out of the cluster. This shifts the balance between filaments joining a cluster and filaments leaving a cluster and results in smaller clusters as observed. For very large reversal rates, clusters disappear entirely and the system becomes isotropic again. In this limit, the filaments do not show active directed motion any more, but rather move back and forth in a fashion similar to passive diffusion. Thus a melt state like for passive polymers is indeed expected.

4.5   Summary and Conclusion

In this study, we have simulations of self-propelled filaments to study their pattern formation and, specifically, the impact of direction reversal on these patterns. The simulations mimic bacterial gliding motility on surfaces and their assembly into clusters and swarms. In contrast to the well-studied spherical or rod-like self-propelled particles, we considered long and flexible filaments.

First, we discussed the patterns that could form in the absence of direction reversals, modulating the bending stiffness (κ_b) and self-propulsion force (f_a) of the filaments at

a relatively low filament density. The results, in agreement with earlier work [47, 127], reflect a competition between the self-interaction of filaments, possible due to their flexibility, and the interaction between filaments. At low bending stiffness and high self-propulsion force, the self-interactions are dominant, leading to the formation of spirals. However, when the bending stiffness increases, the self-interaction is reduced and steric interactions between filaments become more important. In that case, filaments form clusters through collisions and move collectively in these clusters. Based on systematic simulations, we have determined a diagram of states in the κ_b-f_a space.

Then, to understand the impact of stochastic direction reversals, we added a reversal rate to the filaments' dynamics, mimicking the run-reverse movement of bacteria, and examined the effects of this additional control parameter on the formation of motility patterns. In general, reversals counteract both clustering and spiral formation, thus resulting in more isotropic structures. Both negative effects can be understood via dynamical pathways these structures: First, reversals add a second mechanism to interrupt the spooling of spirals and induce unspooling. Second, it also adds new mechanisms for filaments to leave a cluster, as filaments typically leave a coherently moving cluster upon reversal. The additional mechanism for leaving clusters results in smaller clusters compared to the no-reversal reference case. Finally, high reversal rates result in purely back-and-forth motion, similar to a passive scenario.

Our results show that the direction reversals have a great impact on the patterns of microorganisms in the casting media or other systems. The direction reversals have unpleasant effects (like the destruction of spirals and clustering) on the patterns formed by the bacteria, which could also affect the dynamics of microorganisms in the system. Since the direction reversal has a very unique effect on the self-assembly of active filaments, it can also be extended to a higher density to study the effects of the reversal rate on the pattern formed in that regime with/without obstacles in the system.

Acknowledgement

Chapter 5

Self-Buckling of Filamentous Cyanobacteria [1]

5.1 Introduction

Many species of filamentous cyanobacteria exhibit gliding motility when in contact with solid surfaces or other filaments, but display no swimming motion. The mechanism behind this motility appears to be distinct from myxobacteria, and remains debated in the literature. Understanding the collective phenomena in colonies of filamentous cyanobacteria is a key element in interpreting fossil structures, managing giant blooms, or optimizing bioreactor efficiency. At the base of these phenomena lies the individual filament itself, and predicitive models require, as an input, the active and passive mechanical properties of the individuals.

Many techniques for measuring mechanical properties of microorganisms, like

---

traction force microscopy [156], atomic force microscopy (AFM) [157], or microcapillary force sensors (MFS) [158] have been developed in the past. Yet, resolving the forces involved in the self-propulsion of a microorganism over a solid surface remains a formidable task.

Our colleagues, in Dr. Stefan Karpitschka's lab, show that gliding forces can efficiently be quantified by making use of Self-Buckling, a concept which goes back to the work of Leonhard Euler in 1778. Filaments that exceed a certain critical length start to buckle once they encounter an obstacle. By recording numerous such events, they obtained a comprehensive statistics to derive the critical length. Further, they independently quantified the bending rigidity of numerous filaments by MFS. Using non-linear Kirchhoff theory, they derive the propulsion force density from the critical length and the bending rigidity.

In this chapter, we developed molecular dynamics simulations of self-propelled flexible particle chains to compare with continuum theoretical thresholds and experimental data, and set the parameters such as the self-propelling force, the bending stiffness, and the friction coefficient to study the pattern formation of cyanobacterial colonies in the next chapter. The critical lengths obtained in the continuum-theoretical model are close to the peak in the length distribution in freely growing colonies, indicating the importance of this quantity for their self-organization.

In the classical self-buckling theory by Euler, the critical length for a vertical column, clamped at its lower end and free to move at its upper end, of uniform bending modulus B, cross-sectional area A, and density ρ, subjected to its own weight due to gravitational acceleration g, is given by [159]

$$L_c = \left(7.837 \frac{B}{\rho\, g\, A}\right)^{1/3}.$$

(5.1)
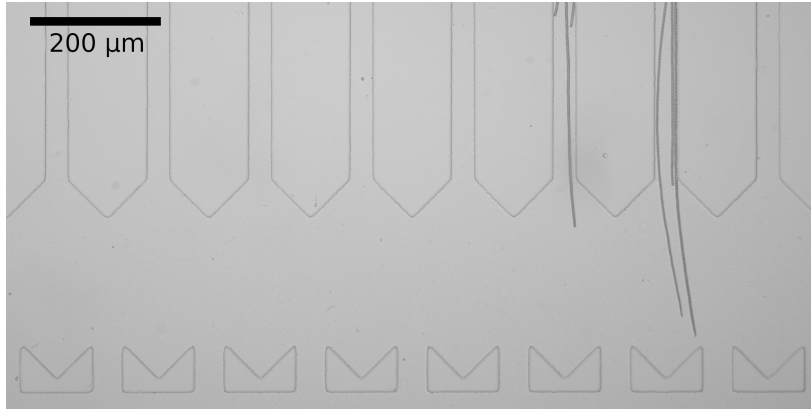
Figure 5.1 – *Microfluidic device with* $40\,\mu m$ *wide channels.*

Active filaments differ from these original considerations: the active force density is (presumably) oriented tangentially instead of vertically, and the typical boundary conditions are a supported front and a free end. Under the action of gravity, this is an unstable situation: the column would simply fall to either side. For filaments that exert active forces in tangential direction, however, this situation is indifferent until buckling induces curvature. Then, the active forces no longer point to the support, causing a net torque and a rotation. The buckling threshold in this case is given by

$$L_c^{(c)} = \left(30.5722\,\frac{B}{f}\right)^{1/3}. \tag{5.2}$$

i.e. by the same scaling with bending modulus and force as in Eq.5.1, but with a different numerical prefactor. This prefactor was obtained by linear stability analysis of Eq.5.1 by assuming three boundary conditions: (i) zero torque at the head of the filament (ii) zero torque at the tail of the filament and (iii) zero force at the tail of the filament (This equation was derived by Dr. Stefan Karpitschka).

5.2 Buckling Experiment

In S. Karpitschka's lab, they use microfluidic devices for the buckling experiments; the standard procedure is given in [160]. Fig. 5.1 shows various designs used for the analysis. The channels are between $20\,\mu m$ and $40\,\mu m$ wide and typically dead-end where the filament hit (preferable orthogonal) the wall. The devices are prepared with PDMS (polydimethylsiloxane) on silicon wafers and then plasma bonded on a glass microscope slide. Through the flushing and loading sites that were added before the bonding, the nutrient solution (BG11) as well as the bacteria are loaded into the device. It is preferred to use fresh and healthy blue-green-looking bacteria and break them into smaller pieces by mechanical stress. Then, microscopy pictures are taken at $6\times$- or $10\times$-magnification with time intervals of either $1\,s$, $10\,s$ and $30\,s$. For the data analysis, the length of the filament, the gliding velocity just before hitting the obstacle, and whether it buckles or not are determined by image analysis. In total, we collected 245 events (☑ 184:61 ☒) for *Oscillatoria lutea* and 114 events (☑ 88:26 ☒) for *Kamptonema animale*.

5.2.1 Buckling Threshold

From these histograms (Fig. 5.2), one can extract the buckling frequency, i.e. the number of buckling events per bin divided by the total number of events per bin. This can be thought of as the buckling probability for a filament in a certain bin and is shown in Fig. 5.2.b for *Oscillatoria lutea* and in Fig. 5.2.a for *Kamptonema animale* as histograms.

The estimated parameters for this data set were found to be

$$
\begin{array}{c|c|c}
\textit{Oscillatoria lutea} & L_c = 171.22\,\mu m & \Delta L_c = 34.61\,\mu m \\
\textit{Kamptonema animale} & L_c = 151.58\,\mu m & \Delta L_c = 18.91\,\mu m
\end{array}
$$
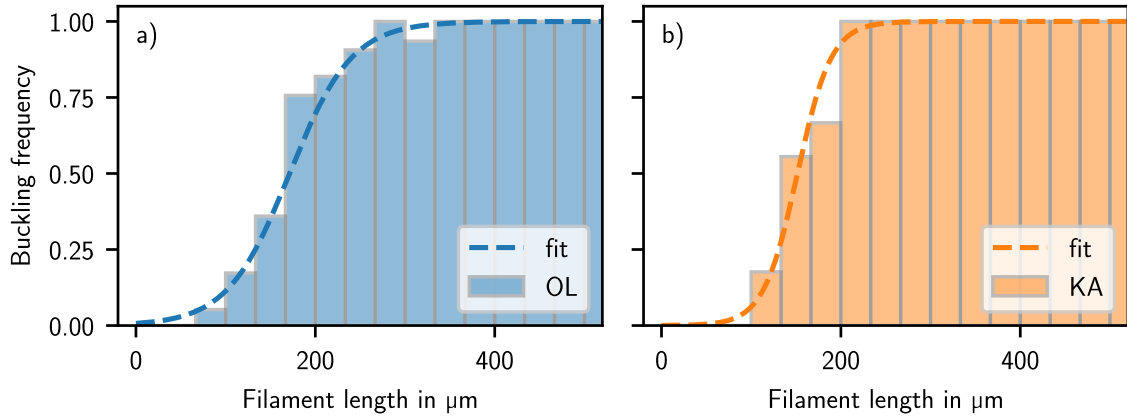
Figure 5.2 – *Buckling frequency for* Oscillatoria lutea *(a) and* Kamptonema animale *(b) determined as the ratio of buckling events to total number of events per bin as the solid histogram. The logistic regression is denoted by the dashed line.*

The corresponding boxplot with median, second and third quartile as well as the whiskers with 5% and 95% of the distribution is shown in Fig.5.3.
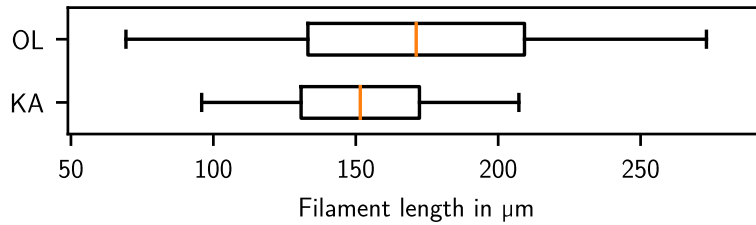
Figure 5.3 – *Critical buckling length L_c of* Oscillatoria lutea *and* Kamptonema animale. *The median is denoted in orange, the second and third quartile by the box and the whiskers show the 5% and 95% of the distribution.*

Some extracted trajectories of filamentous *Cyanobacteria* over time are shown in Fig. 5.4.

5.3   MD Simulations

We consider a filament as a chain of N monomers located at positions $(\boldsymbol{r}_1, \boldsymbol{r}_2, \cdots, \boldsymbol{r}_N)$ in space (Figure 5.5.a). Two consecutive monomers in the filament are connected by a
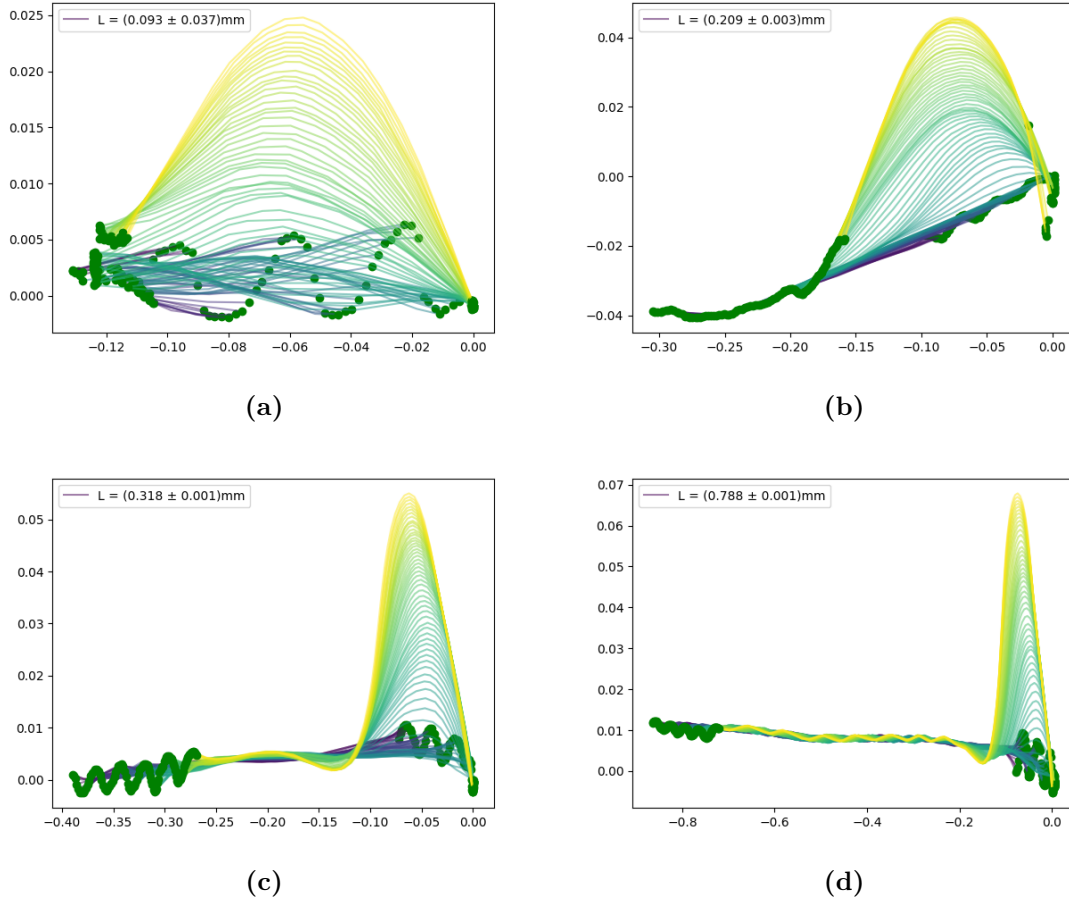
Figure 5.4 – *Trajectories of* Kamptonema animale *(a) and* Oscillatoria lutea *(b-d) over time, shown as color code from dark blue (50 seconds before the event) to yellow (50 seconds after the first contact). The end points are depict as green dots. Space and length is in pixels for 20x magnification. Note that the y-axis has a different spacing than the x-axis.*

harmonic spring. Additionally, the flexibility of the chain is controlled by a harmonic bending potential, where the angle is determined by three successive monomers along the filament. Using Brownian dynamics simulation in the over-damped regime, the equation of motion for each monomer can be written as follows:

$$\zeta \dot{\boldsymbol{r}}_i = -\nabla_i U_s - \nabla_i U_b + \boldsymbol{F}_i^a + \boldsymbol{F}_i^{ex}. \tag{5.3}$$
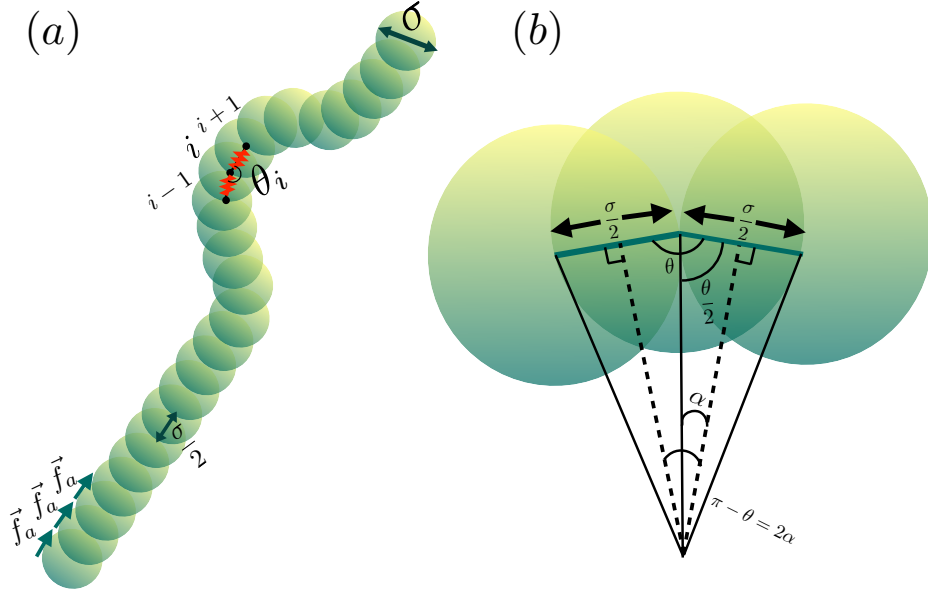
Panel(b) Geometry of the particle chains in MD simulations.

Figure 5.5 – ***Model of a self propelled filament*** *Sketch of a self-propelled filament composed of monomers of diameter σ, where the bond length for each two successive monomers is constant and equal to $r_0 = \sigma/2$. The flexibility of the chain is introduced by the harmonic bending potential, where θ_i is the angle formed by each successive triplet of monomers $i - 1, i, i + 1$.*

where $\dot{\boldsymbol{r}}_i$ is the velocity of the i-th monomer, ζ is the friction coefficient. Four forces contribute to the equation of motion shown on the right hand side: the stretching force, the bending of the chain, the active force, which is responsible for self-propulsion, and the volume exclusion.

U_s stands for the stretching force introduced by the harmonic springs (with an equilibrium length of $r_0 = \sigma/2$)

$$U_s = \frac{\kappa_s}{2} \sum_{j=2}^{N} (r_{j,j-1} - r_0)^2, \tag{5.4}$$

where $r_{j,j-1} = |\boldsymbol{r}_j - \boldsymbol{r}_{j-1}|$ is the distance between the j-th and $j - 1$-th monomers and κ_s is the spring constant associated with stretching.

The flexibility of the filament is controlled by the harmonic bending potential, U_b.

Here θ_i is the angle formed by a successive triplet of monomers $(i-1, i, i+1)$, given by $\theta_i = cos^{-1}\left(\frac{\boldsymbol{r}_{i-1,i} \cdot \boldsymbol{r}_{i,i+1}}{|\boldsymbol{r}_{i-1,i}||\boldsymbol{r}_{i,i+1}|}\right)$. This potential is defined as

$$U_b = \frac{\kappa_b}{2} \sum_{j=2}^{N-1} (\theta_j - \pi)^2, \tag{5.5}$$

where π is the equilibrium angle of between adjacent pairs of monomers, corresponding to a straight chain, and κ_b is the spring constant associated with bending.

The motility of the filament is induced by the active force $\boldsymbol{f}_i^a$,

$$\boldsymbol{f}_i^a = f_a \hat{t}_i, \tag{5.6}$$

where f_a is the magnitude of active force and $\hat{t}_i$, the unit vector tangent to the filament at the position of i-th monomer, defines its direction. For a chain with discrete monomers, $\hat{t}_i$ can be defined as follows:

$$\hat{t}_i = \frac{1}{2} \left(\frac{\boldsymbol{r}_{i+1,i}}{|\boldsymbol{r}_{i+1,i}|} + \frac{\boldsymbol{r}_{i,i-1}}{|\boldsymbol{r}_{i,i-1}|} \right). \tag{5.7}$$

The repulsive force $\boldsymbol{F}_i^{ex}$ that prevents the monomers from overlapping can be implemented using the Week-Chandler-Anderson potential:

$$U_{ext}(r) = \begin{cases} 4\epsilon \left[\left(\frac{\sigma}{r}\right)^{12} + \left(\frac{\sigma}{r}\right)^6 \right] + \epsilon, & r < 2^{1/6}\sigma \\ 0, & \text{otherwise,} \end{cases} \tag{5.8}$$

where σ is the nominal interaction diameter and ϵ is the energy scale of the interaction.

Finally, the obstacle, which has the V-shape with the opening angle $2\pi/5$, is immobile and blocks the path of the filament moving towards the vertex. For the implementation of the obstacle, we used spherical beads that overlap to get a smoother shape (center-to-center distance of two consecutive beads $= \sigma/2$). They were positioned

in the box to so form a V-shape structure.

In order to relate MD simulations to the continuum buckling theory, we need to translate the coefficients of the bond potential κ_b and the active force f_a from MD simulations to the continuum material properties, bending modulus B and active force density f, respectively. This is best done by comparing the total energy of a filament that is bent to a constant radius R, or the total active force, respectively, between the two representations.

From Figure 5.5.b, one can derive the geometric relations

$$L = \frac{\sigma}{2}(N-1), \tag{5.9a}$$

$$R = \frac{\sigma}{4\sin\left(\frac{1}{2}(\pi-\theta)\right)} \overset{|\theta-\pi|\ll1}{\approx} \frac{\sigma}{2(\pi-\theta)}, \tag{5.9b}$$

where N is the number of particles in the chain, σ is their diameter, $\sigma/2$ their equilibrium distance, and L is the contour length in both representations. The total bending energy, $E_B^{(c)}$ and $E_B^{(d)}$ in continuum and discrete representations, respectively, are

$$E_B^{(c)} = \frac{B\,L}{2R^2}, \tag{5.10a}$$

$$E_B^{(d)} = \frac{\kappa_b}{2}(\theta-\pi)^2(N-2). \tag{5.10b}$$

Equating these energies, one obtains a relation between κ_b and B:

$$B = \frac{1}{2}\sigma\,\kappa_b\,\frac{N-2}{N-1} \overset{N\gg2}{\approx} \frac{1}{2}\sigma\,\kappa_b. \tag{5.11}$$

Similarly, the total active force generated by a filament is

$$F_A^{(c)} = f\,L, \tag{5.12a}$$

$$F_A^{(d)} = f_a\,N, \tag{5.12b}$$

such that

$$f = \frac{2\,f_a}{\sigma}\,\frac{N}{N+1} \overset{N \gg 1}{\approx} \frac{2\,f_a}{\sigma}. \tag{5.13}$$

The appearance of N in the exact equations points to discretization effects that should vanish for large N.

The buckling threshold from continuum theory reads

$$L_c^{(c)} = \left(30.5722\,\frac{B}{f}\right)^{1/3}. \tag{5.14}$$

Inserting the relations of geometry and material parameters, we obtain a critical particle count N_c for the discrete version:

$$\frac{\sigma}{2}\,(N_c - 1) = \left(30.5722\,\frac{\sigma^2\,\kappa_b}{4\,f_a}\,\frac{N-2}{N}\right)^{1/3}. \tag{5.15}$$

Note that, dimensionally, this is correct since κ_b has the dimension of an energy (per square radian, which is a dimensionless quantity), and f_a has the dimension of force (which is energy per length). Instead of particle count N, the aspect ratio $a = \frac{1}{2}(N+1)$ is a convenient measure for the polymer shape. The critical aspect ratio becomes

$$\sigma\,a_c \overset{N \gg 2}{\approx} \left(30.5722\,\frac{\sigma^2\,\kappa_b}{4\,f_a}\right)^{1/3}. \tag{5.16}$$

Using the simulation parameters from Fig. 5.5 ($\sigma = 1$, $\kappa_b = 5000$, $f_a = 0.1575$),
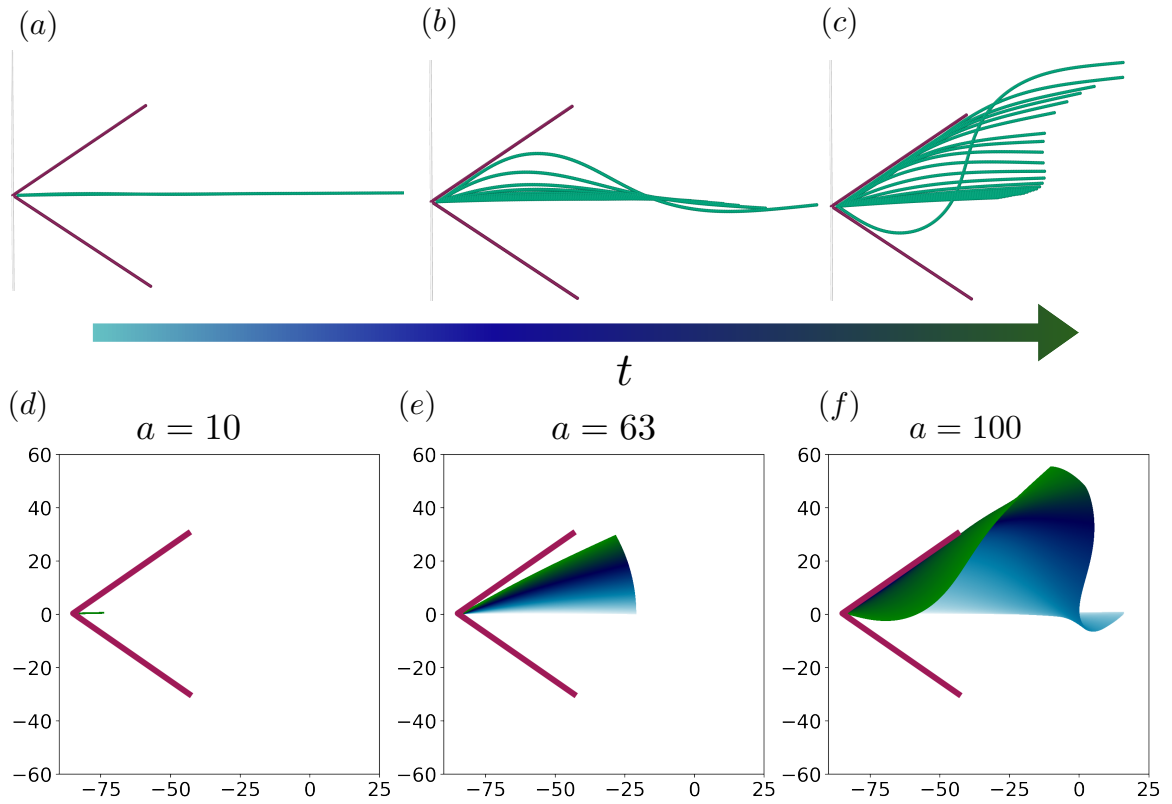
Figure 5.6 – *MD simulation results for buckling particle chains, for $\kappa_b = 5000$ and $F_{act} = 0.1575$ Panel(a-c)show snapshot of configuration of simulation for different time Panel(d-f) show trajectories of the filament for aspect ratios 10,63,100 over time, shown as color code from light blue(2 seconds before the hitting the vertex)to dark green (118 seconds after the first contact).*

we obtain $a_c = 62.37$. To confirm this value, we performed simulations for different aspect ratios $60 - 65$ (Fig. 5.6) and calculated the front-mid-end angle of each filament as a function of time. Remarkably, we observed that there is a transition between $a = 62$ and $a = 63$ that is in perfect agreement with theory and experiment (Fig. 5.7). In Fig. 5.6(d-f), we plotted the trajectory of the filaments for $a = 10$ (below the critical length), 63 (critical length), and 100 (above the critical length) fro given the self-propulsion force and the bending stiffness , which clearly shows the buckling of the filament at and above the critical length.

In chapter 6, we use another set of parameters in the MD simulations ($f_p = 1.26$
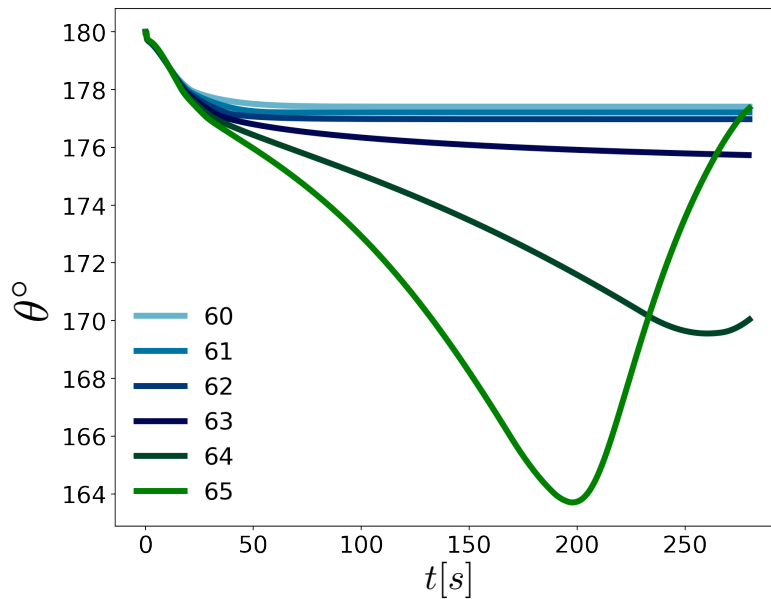
Figure 5.7 – *Front-Mid-End angle of MD simulations as a function of time, for aspect ratios 60-65.*

and $k_b = 5000$). These are close to the experimental parameters and were chosen by the aspect ratio relative to the critical aspect ratio for buckling: using Eq. 5.16, we insert $f_p = 1.26$, and obtain $a_c = 31.185$. In Fig. 5.8 also we observe a transition between $a = 31$ and $a = 32$ in the simulation which is in perfect agreement with the results for the longer filaments. We will use these parameters, $\sigma = 1$, $\kappa_b = 5000$, $f_a = 1.26$, $a_c = 32$, in the next chapter to study pattern formation of filamentous *Cyanobacteria* at high density to make a comparison with the experimental observation.

5.4 Conclusion

Using the critical length from theory, Eq. 5.16, the measured critical lengths, and the measured bending moduli, one can calibrate the active force density of each species:

$$
\begin{array}{l|l}
\textit{Oscillatoria lutea} & f = 0.85\,\text{nN/µm} \\
\textit{Kamptonema animale} & f = 0.88\,\text{nN/µm}
\end{array}
$$
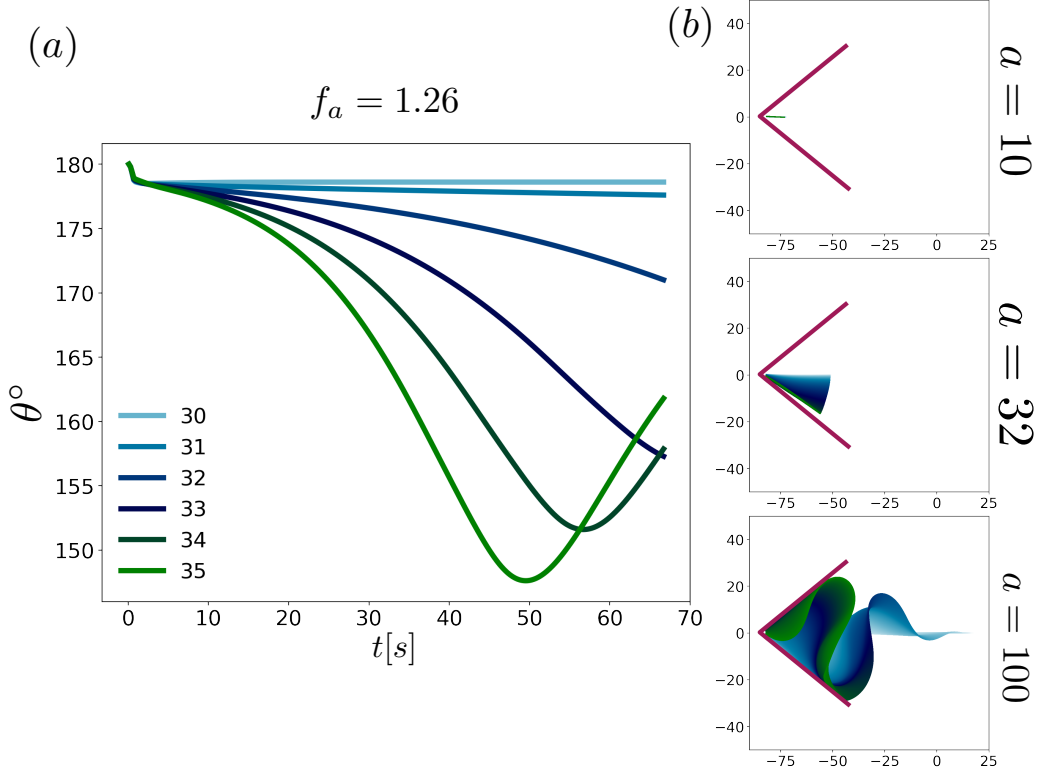
Figure 5.8 – *MD simulation results for buckling particle chains, for $\kappa_b = 5000$ and $f_a = 1.26$ Panel(a) Front-Mid-End angle of MD simulations as a function of time, for aspect ratios 30-35. Panel(b) Trajectories of the filament for aspect ratios 10,32,100 over time, shown as color code from light blue(2 seconds before the hitting the vertex)to dark green (65 seconds after the first contact)*

The values are remarkably similar. An error estimate using standard error propagation and the inter-quartal distances of bending moduli and critical lengths would give errors around 50 %. In order to relate MD simulations to the continuum buckling theory, we translated the coefficients of the bond potential κ_b and the active force f_a from MD simulations to the continuum material properties, bending modulus Band active force density f, respectively. The buckling experiment provides us the force density (active force per bead). Since we can also measure the velocity of the filament, this also provides the friction coefficient, a quantity which is usually difficult to measure for such gliding motion. Thus, we obtain a complete quantitative parametrization of the filament properties, which we can use in our MD simulation in order to study pattern

formation of filamentous *Cyanobacteria* in the next chapter.

Chapter 6

Collective Dynamics of Gliding Filamentous Cyanobacteria at High Density

6.1 Introduction

In this chapter, we investigate dense layers of filaments as a new model system for active matter. Due to their inherent non-equilibrium nature, active matter systems exhibit a wealth of fascinating material properties and collective behaviors. Examples include animal groups such as fish and birds or colonies and suspensions of microorganisms such as bacteria, as well as synthetic self-propelled particles.

The bewildering collective behavior of active matter systems has led scientists in recent decades to explore the collective dynamics of active systems at the cellular and subcellular levels. A significant part of these studies deals with experimental work on self-propelled particles in biological systems such as bacterial suspensions and molecular motors. In addition, fundamental theoretical models such as the agent-based model of Vicsek *et al.* [32, 57] and the hydrodynamic approach proposed by Toner & Tu [56]

have shown that fundamental physical mechanisms are often sufficient to explain the observed collective behavior in living systems.

Biological systems have inspired scientists to establish models that mimic their motility strategies. In this study, in addition to the current models of worm-like filaments, we add a reversal mechanism that mimics the movement of light-sensitive bacteria which was missing in previous studies of long, flexible active filaments. This mechanism allows us to control the movement of the filaments externally. A prototypical biological example of such a system is *Cyanobacteria*.

6.2 *Cyanobacteria*

Cyanobacteria prosper in every illuminated aquatic environment. Given its importance in the carbon and nutrient cycles, it has played a pivotal role in the composition of oceans, and the atmosphere for billions of years. *Cyanobacteria* have also been used as useful model organisms for understanding and improving photosynthetic productivity.

To modeling their dynamics, one should note that *Cyanobacteria* are an enormously diverse group of prokaryotes and present in a wide range of habitats such as marine, freshwater, soil, etc. The diversity of species and living conditions forces them to use different strategies to move and function. In this chapter, we would like to focus on genera such as *Oscillatoria*, *Kamptonema*, and *Lyngbya*. In these types of cyanobacteria, the trichome length, i.e. the organization of independent cells into multicellular filaments, varies greatly from a few tens to several thousand cells. Their aspect ratio is usually greater than one and they are very flexible and can move on surfaces. Moreover, they are photophobic and sensitive to changes in light intensity. In the following, we will discuss these two essential behaviour of these types of *Cyanobacteria* in more detail.

6.2.1 Gliding motility

Gliding motility is a process of bacterial movement on a surface, carried out by several bacterial species. It is an active movement exhibited by microorganisms in contact with a solid substrate, with no evidence of organelle motility or conformational change. Although the gliding displayed by blue-green algae has been extensively discussed in the literature, there is still no comprehensive explanation for the causative mechanism.

The physical mechanism behind the gliding movement of prokaryotic cells at the cellular level can be classified into three categories: surface-tension gradients, slime extrusion, and traveling waves.

6.2.1.1 Surface-tension gradients

In 1923, Coupin [161] suggested that the movement of *Oscillatoria sp.* was due to the the gradient of surface tension, but he did not provide any evidence to support this idea. Later, in 1934, Burkhholder [162] restated this idea and provided some observation in the behavior of cut filaments of Oscillatoria. Additionally, in 1983, Keller *et al.* [163], developed a theoretical model to explain that surface tension is the deriving force for gliding motility of *M. xanthus* and validated their model with experimental observations [164].

Surface tension is the tension at the interface between two immiscible liquids as a result of the changing forces on the molecules in this area. This force is exerted in the plane of the interface and is omnidirectional so that an object suspended at the interface experiences the same "pulling force" in all directions. Therefore, no net force acts on the object and it remains motionless. The magnitude of the surface tension depends on the nature of the two liquids in contact and is higher at liquid-gas interfaces than at liquid-liquid interfaces. Indeed, Aqueous solutions have the highest surface tension among biologically relevant liquids. A surfactant is a molecule that accumulates
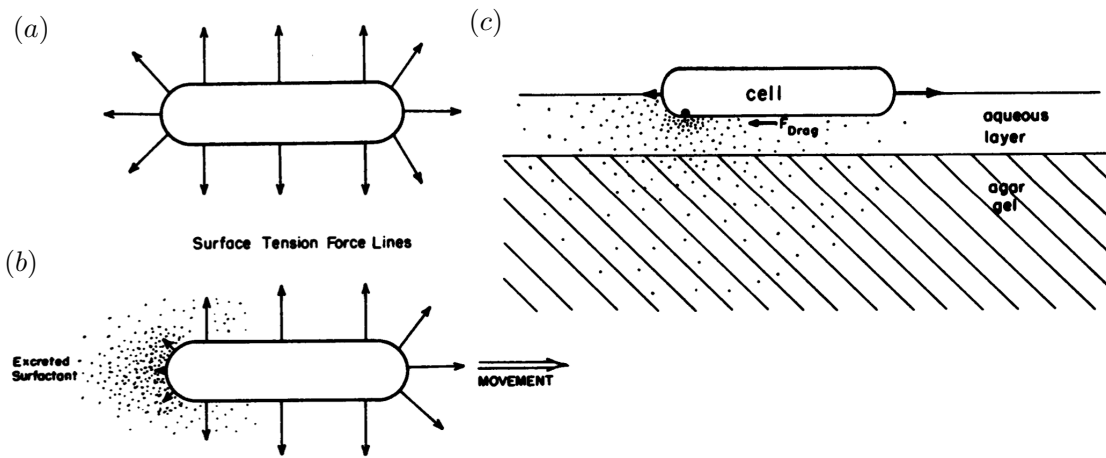
Figure 6.1 – *Schematic representation of a myxobacterial cell at an interface Panel (a) A uniform force in all directions results in no net force. Panel (b) A surfactant secreted at one end of the cell results in a lower surfactant tension at the end and produces an unbalanced force leading to directional motion. Panel (c) The side view of the cell at an interface shows the gradient of the surfactant that causes the cell to move. The pictures are taken from [163].*

preferentially at the interface to lower the surface tension. If surfactant molecules are uniformly distributed on the surface, the surface tension would be uniformly reduced compared to the pure interface (Figure 6.1 .a). On the other hand, a non-uniform surfactant concentration would lead to a gradient in surface tension and in turn give rise to net directional forces (Figure 6.1 .b and c). These directional forces are capable of propelling objects suspended in or near the interface. It is postulated that the *Myxobacteria* can excrete a surfactant from sites near the ends of the cells. When the excretion is largely or entirely from one of the sites, these surfactants lower surface tension in the vicinity of that site causing an unbalanced force on the cell. Consequently, the cell propels at the plane of the interface with a speed that results in a drag force, on the cell body, equal to force generated by the surface tension gradient.
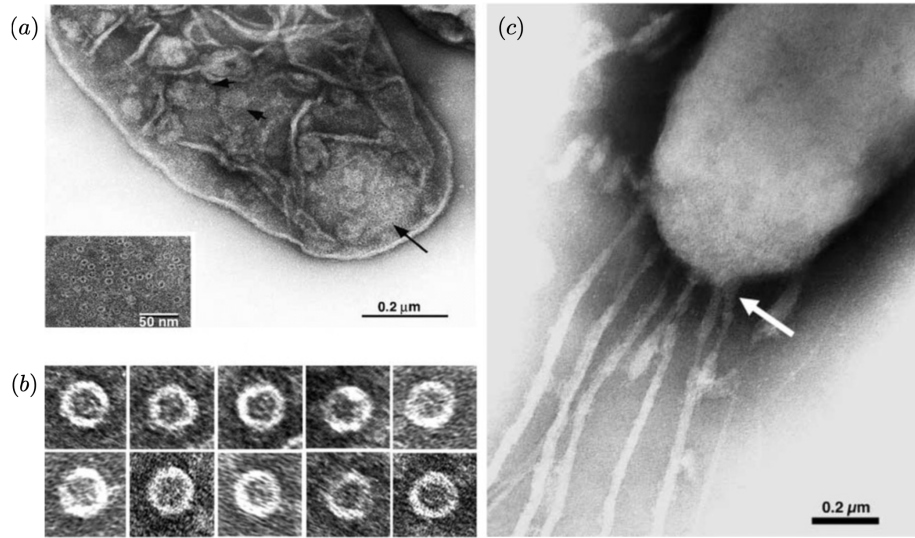
Figure 6.2 – *Secretion of slime by myxobacteria. Panel (a) Negatively stained electron micrograph of an isolated M. xanthus cell envelope showing multiple ringlike structures located predominantly at the poles of the cell. The inset shows a higher magnification of the nozzle array in the region indicated by the long arrow. Panel (b) A gallery of electron micrographs of negatively stained isolated nozzles. Panel (c) Electron micrograph of a gliding cell. At higher magnification, it can be seen that the slime trails are composed of several slime bands, which are secreted from the sites at the cell pole, where the nozzles are located. The images are taken from [165]*

6.2.1.2 Slime extrusion

A second mechanism for gliding motility involves the extrusion of slime from an organelle called the "junctional pore complex". Slime extrusion has been identified as a mechanism for thrust generation in gliding bacteria. Initially, this model was largely discarded because it was unclear how slime excretion could generate sufficient thrust force to propel the bacteria. In addition, estimation of the energetic costs of slime production appeared to be excessively high. Note that slime is a polyelectrolyte gel, i.e., a charged, cross-linked polymer network embedded in a liquid solvent. Such gels are capable of swelling to many hundred times their dry volume, generating enormous swelling forces. Wolgemuth et al. [165, 166] proposed a model for force generation based on the hydration of slime and were able to show that the slime excursion could generate a driving force sufficient to explain the observed gliding force of both myxobacteria

and *Cyanobacteria*, and they were able to predict how the bacterial velocity depends on the drag force.

Furthermore, slime was still found to be secreted underneath the surface of *M. xanthus* mutant cells, which are nonmotile, thereby showing that the production of slime does not necessarily lead to bacterial gliding [167].

6.2.1.3 Traveling waves
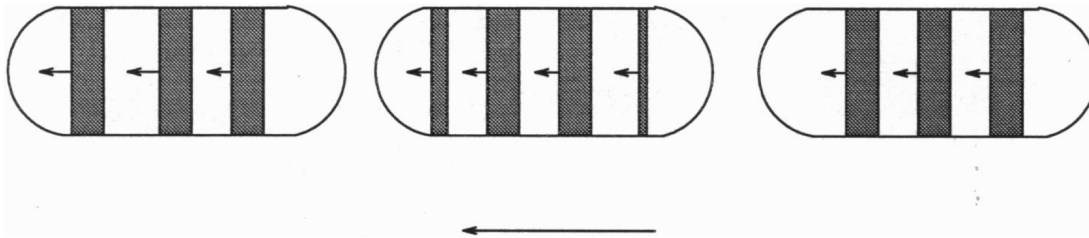
Figure 6.3 – *Schematic representation of traveling tangential wave with a wave length of about one-third of body length. The dark areas shows the region of contraction and light areas are regions of expansion and eventually cell swims to the left. the picture is taken from [168]*

The third model, built at the scale of the entire cell, is based on waves propagating on the surface of the bacteria, with the thin liquid acting as a lubricant. Initially, Brien *et al.* [169] developed this model for a gliding bacterium, *Flexibacter strain BH3*. The model has been applied to myxobacteria with various complex rheological behaviors for the slime in the presence of a rigid substrate [170–172] as well as a soft substrate [173] to explain the mechanosensitivity as a feature of the gliding bacteria in experiments and also in an agent-based model [174].

Traveling waves are surface oscillations. They can be either normal or tangential to the surface or a combination of both. To model this mechanism, imagine the organism as a sphere or ellipsoid with tangential waves traveling from one pole to the other, where the wave amplitudes are constant along the latitudes as one can see in the figure

6.3. The wavelength is denoted by λ, and a denotes the amplitude of these traveling surface waves. Therefore, the spherical organism swims with velocity V [168]:

$$V = (\frac{\pi^3}{2})(\frac{a}{\lambda})^2 c. \tag{6.1}$$

This formula is only valid with the approximation of $\frac{a}{\lambda} \ll 1$. In deriving this formula, it is assumed that the surface waves are axially symmetric, so that they are constant at all times along the meridians, which implies that the organism moves in a straight fashion. However, actual organisms often move in helical paths.

All the mechanisms presented in this section have been proposed to understand the gliding mechanism of bacteria, including that of *Cyanobacteria*. In addition to the gliding movement, *Cyanobacteria* have a severe need for light. In the next section, we elaborate on this particular property of *Cyanobacteria*.

6.2.2 Photo-sensitive movement of *Cyanobacteria*

Light is a source of energy for *Cyanobacteria*. An insufficient amount of light can cause inadequate energy production, whereas, an excessive amount of light has the potential to severely cause cellular damage through several mechanisms such as decreasing photosynthesis efficiency and causing damage by bleaching. Photosynthetic microorganisms, such as *Cyanobacteria*, are capable of phototactic migration towards environmental niches in which light is bright enough to efficiently drive photosynthesis, while at the same time being adequately filtered of harmful UV or excess light [151].

Filamentous *Cyanobacteria* can modulate their movement in response to the incident light to find optimal lighting conditions in their environment. There are three types of photo-movement: photokinesis, phototaxis, and photophobic responses.

- **photokinetic** microorganisms such as *Phormidium autumnale* adapt their sliding

speed to the incident light intensity. The gliding speed increases linearly with light intensity [175].

- **phototactic** microorganisms move towards the light source. The positive phototactic species tend to move persistently towards the regions with higher light intensity. However, there are other species, such as *Phormidium autumnale* that cannot move directly to the light source, but rely on random collisions to align themselves in the direction of the light. Others such as *Anabaena variabilis* can steer by bending the trichome [176].

- **photophobic** organisms react to spatial and temporal light gradients. There are some types of organisms that when moving from a darker area to a brighter area, reverse movement direction to avoid the higher light intensity; a behavior known as photophobic response. On the other hand, others do the opposite, that is, when they go from a bright area to a dark area, they reverse their direction to stay in the bright area, also known as a step-down response [150].

Although *Cyanobacteria* exhibit all three types of photo-motion, the most important one, which plays an important role in pattern formation, is photophobia. This has been a source of inspiration for us to use stochastic reversals of the movement direction as one of the key parameters to control pattern formation in the system.

There is a fascinating cyanograph experiment by Häder on the pattern formation of *Cyanobacteria* in vitro that describes the photo-movement, or more precisely the photophobic property, of these bacteria (figure 6.4). He demonstrated that bacteria can position themselves in the brighter area by moving away from darker area to form a photographic positive on the bacterial culture.

Several theoretical and experimental model systems have been developed to study pattern formation in such systems. The main goal is to mimic the behavior of such agents in a controlled fashion to attain a better comprehension of the mechanism

Figure 6.4 – *Häder cyanograph experiment. A Petri dish with a culture of photophobic filamentous Cyanobacteria (Phormidium uncinatum) onto which a photographic negative is projected. Filamentous Cyanobacteria cover the brighter area and avoid the darker area. The image is taken from [152]*

at work. A well-known class of active matter which includes elongated bacteria and active filamentous particles is a group of rod-shaped particles. This class of particles resembles nematic liquid crystals, but because of their activity, a new concept was introduced to study them: active nematics.

6.3 Active Nematic

As a result of the directional motion, the self-propelled particles have an inherent polarity. Steric interactions in the elongated class of active matter systems cause them to order their alignment, the so-called nematic order. The nematic ordering in dense systems of active matter opened a new area of interest called active nematics [10, 177, 178]. Nematic order is ubiquitous in dense systems of motor-driven actin filaments [179], microtubules [3], bacterial colonies such as gliding bacteria [31] and even non-living analogues, such as monolayers of vibrated granular rods [33–35]. The

fascinating realization of nematic order is evident in structures such as flocks and swirls, which have attracted much interest and attention in recent years. This interest has led scientists to go beyond molecular systems and develop the concept of active nematics at the mesoscopic level, for example, bacteria and neural stem cells.

In most known bacterial systems, such as the *Cyanobacteria*, spectacular patterns have formed that exhibit nematic order and topological defects. Scientists have endeavored to elucidate the mechanism behind these patterns to clarify the physical parameters that play an essential role in the formation of such patterns [31].

Most theoretical and simulation studies have been performed for spherical active particles or short rod-shaped particles that mimic experimental observations. In recent years, a new model for mimicking the movement of bacteria has been proposed called self-propelled worm-like filaments [46]. This model combines a worm-like chain model for semi-flexible polymers with propulsion force to imitate the motion of bacteria. The propulsion force acts tangentially along all bonds of a filament and when the self-propulsion force approaches zero, this model reverts to a standard worm-like chain model. The studies by Gompper's group [46, 47, 133] show that a wide range of collective behavior can occur in a system of active, semi-flexible filaments, ranging from spirals to swarms of filaments. Our results in Chapter 4 also confirm these rich behaviour in such systems. However, most of these studies have been at a low density of short filaments. In this chapter, we investigate the opposite case: long, semi-flexible filaments at high-densities. *Cyanobacteria* colonies provide a realization of the opposite case: long semiflexible filaments at high density.

6.4 Model and parameters

We adapted the active filaments model in chapters 4 and 5. We parameterize all variables such as bending stiffness, self-propelling force, friction coefficient, and aspect
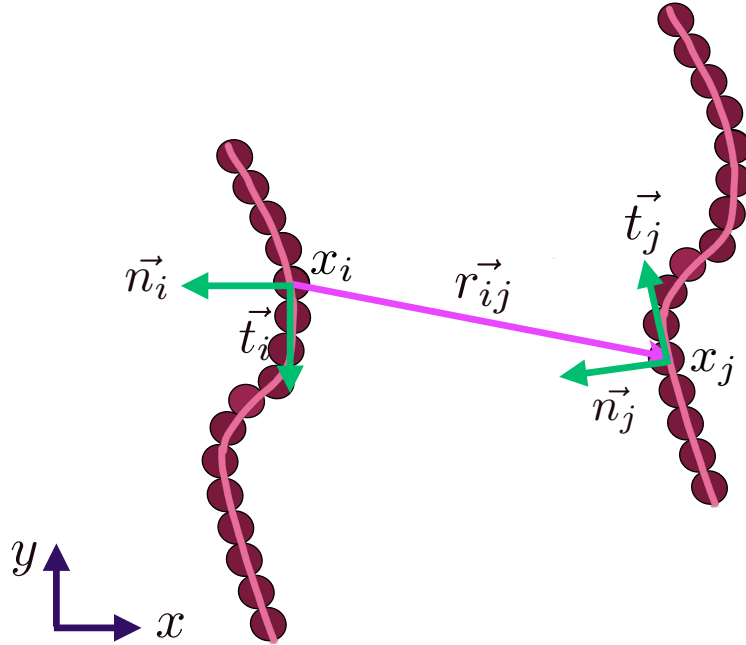
Figure 6.5 – *The displacement vector $\boldsymbol{r}_{ij}$ in the local frame of reference of particle i . The tangential and normal vectors of particles i and j are indicated in green.*

ratio of the filaments based on chapter 5.

6.5 Analysis Methods[1]

6.5.1 Particle reference

Each filament i is supposed to consist of particles $j \in \{1, 2, ..., N_i\}$, where N_i is the number of particles on filament i. The particle location is $\boldsymbol{x}_{i,j}$ and it has an orientation, described by the tangent unit vector $\boldsymbol{t}_{i,j}$. $\boldsymbol{n}_{i,j}$ shall be the normal vector, obtained by a 90 degree counter-clockwise rotation of $\boldsymbol{t}_{i,j}$, such that $\boldsymbol{t}_{i,j} \times \boldsymbol{n}_{i,j} = \boldsymbol{e}_z$.

Since we are not discriminating between particles on identical or different filaments, we simplify the notation to a single index, using $\boldsymbol{x}_i$, $\boldsymbol{t}_i$, and $\boldsymbol{n}_i$ for the position, tangent, and normal unit vectors, where $i \in \{1, 2, ..., N\}$, and N is the total number of particles.

---

[1]This section is based on a manuscript in preparation with Dr. Stefan Karpitschka

The density field ϕ of all particles is given by

$$\phi(\boldsymbol{x}) = \sum_{i=1}^{N} \delta(\boldsymbol{x} - \boldsymbol{x}_i) \,, \tag{6.2}$$

where $\delta(\cdot)$ is Dirac's δ distribution. Similarly, the polarization field is given by

$$\boldsymbol{p}(\boldsymbol{x}) = \sum_{i=1}^{N} \boldsymbol{t}_i \, \delta(\boldsymbol{x} - \boldsymbol{x}_i) \,, \tag{6.3}$$

and the orientational nematic order parameter tensor is

$$q_{kl}(\boldsymbol{x}) = \sum_{i=1}^{N} \left((\boldsymbol{t}_i \cdot \boldsymbol{e}_k)(\boldsymbol{t}_i \cdot \boldsymbol{e}_l) - \frac{\delta_{kl}}{2} \right) \delta(\boldsymbol{x} - \boldsymbol{x}_i) \,, \tag{6.4}$$

where the indices k and l are for any direction x or y, $\boldsymbol{e}_x$ and $\boldsymbol{e}_y$ are the Cartesian unit vectors, and δ_{kl} is the Kronecker delta. q_{kl} is a traceless symmetric tensor that encodes the nematic orientation 2θ and amplitude Q:

$$q_{xx} = -q_{yy} = Q \cos 2\theta \tag{6.5}$$

$$q_{xy} = Q \sin 2\theta \tag{6.6}$$

Q is the positive eigenvalue of q_{kl}. For a single particle i with orientation $\boldsymbol{t}_i$, $S = 1/2$. Thus the amplitude of the nematic order should be $2Q$, which takes values in $[0, 1]$. The eigenvector corresponding to Q is $\begin{pmatrix} \cot\theta \\ 1 \end{pmatrix}$, the eigenvector corresponding to $-Q$

is $\begin{pmatrix} -\tan\theta \\ \\ 1 \end{pmatrix}$. To obtain 2θ and $2Q$ from q_{kl}, we'll use

$$2Q = \sqrt{(q_{xx} - q_{yy})^2 + (2q_{xy})^2} = 2\sqrt{q_{xx}^2 + q_{xy}^2} \tag{6.7}$$

$$2\theta = \arctan\left(q_{xx} - q_{yy}, 2q_{xy}\right) = \arctan\left(q_{xx}, q_{xy}\right) \tag{6.8}$$

with the two-parameter version of the arcus tangent, $\arctan(\Delta x, \Delta y)$, to avoid ambiguities between quadrants.

The displacement vector between two particles i and j is given by

$$\boldsymbol{r}_{ij} = \boldsymbol{x}_j - \boldsymbol{x}_i. \tag{6.9}$$

We are interested in the density and orientation correlation in the particle frame of reference, given by its unit tangent and normal vectors, $\{\boldsymbol{t}_i, \boldsymbol{n}_i\}$. The Cartesian components of the displacement vector in this frame of reference are given by the dot products of $\boldsymbol{r}_{ij}$ with unit tangent and normal vectors of particle i :

$$\boldsymbol{r}_{ij}^{(i)} = \left(\boldsymbol{r}_{ij} \cdot \boldsymbol{t}_i\right)\boldsymbol{e_x} + \left(\boldsymbol{r}_{ij} \cdot \boldsymbol{n}_i\right)\boldsymbol{e_y}. \tag{6.10}$$

Equivalently, there is a polar representation with components

$$\{r_{ij}^{(i)}, \phi_{ij}^{(i)}\} = \{|\boldsymbol{r}_{ij}|, \arctan(\boldsymbol{r}_{ij} \cdot \boldsymbol{t}_i, \boldsymbol{r}_{ij} \cdot \boldsymbol{n}_i)\}, \tag{6.11}$$

again, using the two-parameter version of the arcus tangent, $\arctan(\Delta x, \Delta y)$, to avoid ambiguities between quadrants. The particle density field, in the frame of reference of particle i, is given by

$$\phi^{(i)}(\boldsymbol{r}) = \sum_{j=1}^{N} \delta\left(\boldsymbol{r} - \boldsymbol{r}_{ij}^{(i)}\right). \tag{6.12}$$

We will use $\boldsymbol{r}$ for coordinates relative to a reference particle and $\boldsymbol{x}$ for absolute coordinates.

6.5.2 Mean field

A local mean density field can be derived by convolving the density with a normalized kernel $K(\boldsymbol{x})$, for instance $K(\boldsymbol{x}) = \frac{1}{\pi R^2}\Theta(R - |\boldsymbol{x}|)$ where $\Theta(\cdot)$ is Heaviside's Θ and R the radius of the (circular) kernel:

$$\overline{\phi}_K(\boldsymbol{x}) = \int d\boldsymbol{x}^2 \; \phi(\boldsymbol{x}')K(\boldsymbol{x} - \boldsymbol{x}'). \tag{6.13}$$

The same applies for mean polarization and mean nematic tensor:

$$\overline{\boldsymbol{p}}_K(\boldsymbol{x}) = \frac{1}{\overline{\phi}(\boldsymbol{x})} \int d\boldsymbol{x}^2 \; \boldsymbol{p}(\boldsymbol{x}')K(\boldsymbol{x} - \boldsymbol{x}'), \tag{6.14}$$

$$\overline{q}_{kl,K}(\boldsymbol{x}) = \frac{1}{\overline{\phi}(\boldsymbol{x})} \int d\boldsymbol{x}^2 \; q_{kl}(\boldsymbol{x}')K(\boldsymbol{x} - \boldsymbol{x}'). \tag{6.15}$$

Magnitude and orientation of $\overline{\boldsymbol{p}}_K(\boldsymbol{x})$ are straight forward. Magnitude and orientation of $\overline{q}_{kl,K}(\boldsymbol{x})$ are calculated by

$$|\overline{q}_K| = \sqrt{\left(\overline{q}_{xx,K} - \overline{q}_{yy,K}\right)^2 + \left(2\overline{q}_{xy,K}\right)^2} = 2Q_K, \tag{6.16}$$

$$2\theta_{q_K} = \arctan\left(\overline{q}_{xx,K} - \overline{q}_{yy,K}, 2\overline{q}_{xy,K}\right). \tag{6.17}$$

6.5.3 Order parameter correlations

The density correlation in the particle reference frame is obtained by averaging the density distributions for all particle reference frames,

$$S(\boldsymbol{r}) = \frac{1}{N}\sum_{i=1}^{N}\phi^{(i)}(\boldsymbol{r}) = \frac{1}{N}\sum_{i=1}^{N}\sum_{j=1}^{N}\delta\left(\boldsymbol{r} - \boldsymbol{r}_{ij}^{(i)}\right). \tag{6.18}$$

A histogram representation of $S(\boldsymbol{r})$, composed of finite local mean density values, is obtained by integrating over the respective bin $\mathcal{B}$, normalizing by its norm (area) $||\mathcal{B}|| = \int_{\mathcal{B}} d\boldsymbol{r}$:

$$\widetilde{S}(\mathcal{B}) = \frac{1}{||\mathcal{B}||} \int_{\mathcal{B}} d\boldsymbol{r}^2 \, S(\boldsymbol{r}) \tag{6.19}$$

The polar orientation correlation P is calculated equivalently, using the dot product of the tangent vectors as weight:

$$P(\boldsymbol{r}) = \frac{1}{N} \sum_{i=1}^{N} \sum_{j=1}^{N} (\boldsymbol{t}_i \cdot \boldsymbol{t}_j) \, \delta\left(\boldsymbol{r} - \boldsymbol{r}_{ij}^{(i)}\right). \tag{6.20}$$

The mean polar orientation correlation $\widetilde{P}(\mathcal{B})$ is obtained by integrating over a bin $\mathcal{B}$ and normalizing with the binned density correlation:

$$\widetilde{P}(\mathcal{B}) = \frac{1}{||\mathcal{B}|| \, \widetilde{S}(\mathcal{B})} \int_{\mathcal{B}} d\boldsymbol{r}^2 \, P(\boldsymbol{r}) \tag{6.21}$$

The nematic orientation correlation M must use a weight that is cyclic on π instead of 2π in terms of the angle θ_{ij} between the tangent vectors $\boldsymbol{t}_i$, $\boldsymbol{t}_j$ of two particles i and j:

$$M(\boldsymbol{r}) = \frac{1}{N} \sum_{i=1}^{N} \sum_{j=1}^{N} \cos\left(2\theta_{ij}\right) \delta\left(\boldsymbol{r} - \boldsymbol{r}_{ij}^{(i)}\right). \tag{6.22}$$

The mean nematic orientation correlation $\widetilde{M}(\mathcal{B})$ is again obtained by integrating over a bin $\mathcal{B}$ and normalizing with the binned density correlation:

$$\widetilde{M}(\mathcal{B}) = \frac{1}{||\mathcal{B}|| \, \widetilde{S}(\mathcal{B})} \int_{\mathcal{B}} d\boldsymbol{r}^2 \, M(\boldsymbol{r}) \tag{6.23}$$

The angle between two vectors is unambiguously calculated by

$$\theta_{ij} = \arctan(\boldsymbol{t}_j \cdot \boldsymbol{t}_i, \, \boldsymbol{t}_j \cdot \boldsymbol{n}_i). \tag{6.24}$$

With standard trigonometric identities, one can show that

$$\cos\left(2\theta_{ij}\right) = \frac{\left(\boldsymbol{t}_j \cdot \boldsymbol{t}_i\right)^2 - \left(\boldsymbol{t}_j \cdot \boldsymbol{n}_i\right)^2}{\left(\boldsymbol{t}_j \cdot \boldsymbol{t}_i\right)^2 + \left(\boldsymbol{t}_j \cdot \boldsymbol{n}_i\right)^2} = \left(\boldsymbol{t}_j \cdot \boldsymbol{t}_i\right)^2 - \left(\boldsymbol{t}_j \cdot \boldsymbol{n}_i\right)^2, \qquad (6.25)$$

the last equality following from $\boldsymbol{t}$ and $\boldsymbol{n}$ being defined as unit vectors.

In practice, $\widetilde{S}(\mathcal{B})$, $\widetilde{P}(\mathcal{B})$ and $\widetilde{M}(\mathcal{B})$ are obtained by calculating $\boldsymbol{r}_{ij}^{(i)}$, $\boldsymbol{t}_i \cdot \boldsymbol{t}_j$, and $\cos\left(2\theta_{ij}\right)$ for all i and j. Then, a histogram with a collection of bins $\mathcal{B}$ is computed over the components (Cartesian or polar) of all the $\boldsymbol{r}_{ij}^{(i)}$. With unity weights, one then obtains $\widetilde{S}$. Using $\boldsymbol{t}_i \cdot \boldsymbol{t}_j$ as weight for $\boldsymbol{r}_{ij}^{(i)}$, and dividing the resulting histogram entries by the corresponding entries of $\widetilde{S}$, one obtains $\widetilde{P}$. $\widetilde{M}$ analogously, using $\cos\left(2\theta_{ij}\right)$ as weights.

6.6   Results

To study the pattern formation that has been observed in colonies of *Cyanobacteria* in the experiment, we first infer the relevant parameters for our model (described in Chapter 5) from the self-buckling experiments. The value of the relevant parameters that we get are (in the dimensionless units described in 5.3): bending stiffness $\kappa_b = 5000$, self-propulsion force $f_{act} = 1.26$ and the friction coefficient $\gamma = 1.26$ at sufficiently high density 0.7 for highly elongated bacteria with the aspect ratio of $a = 32$. Note that the critical aspect ratio a_c for *Kamptonema animale* species is $a_c \sim 32$ where the filamentous structure starts to buckle. To attain a better understanding of the behavior seen in this system, we first performed simulations without direction reversals.
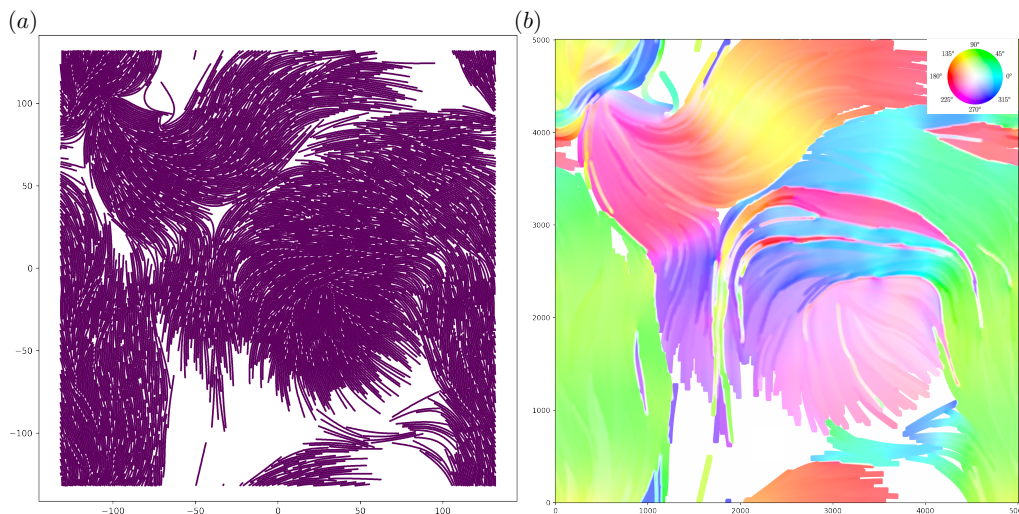
Figure 6.6 – *Panel (a) A snapshot of the simulation. Panel(b) describes the velocity of the filaments where color encodes the direction of the filaments' instantaneous velocity and the magnitude is represented by saturation.*

6.6.1 Pattern formation without direction reversal

6.6.1.1 Mean field analysis

As can be seen in Figure 6.6.a, for previously described parameter values, filaments form large bundles in a steady-state and display spectacular collective motion. In Figure 6.6.b, the direction of each monomer in a filament is encoded by a continuous color map, and the magnitude of the velocity is represented by the saturation of the colors. There are large bundles of filaments that point in the same direction and also move together. In addition, some small bundles that come from the opposite direction pass through larger bundles in the system.

Figure 6.7.a indicates the local density in the system, which is mostly nonzero and varies heterogeneously in the system. Since there are large bands of the filaments in the system, one can also look at the polar and nematic order of the filaments. Figure 6.7.b shows the polar bands in the system which appear to be very strongly ordered. The colors encode the direction of the polar band, and the saturation represents their magnitude. As can be seen in the middle of 6.7.b, there are small polar bands that

(a) (b) (c)
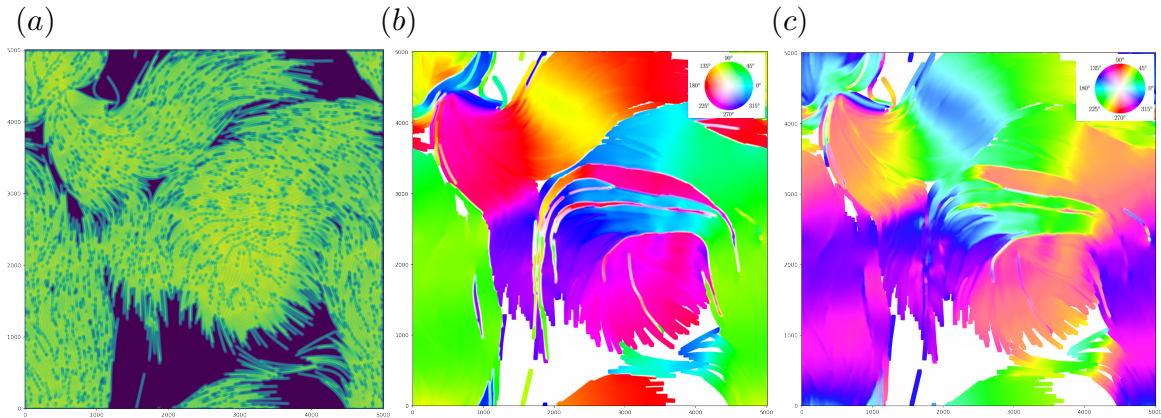
Figure 6.7 – *Panel (a) The local density field shows strong spatial heterogeneity in the steady state. Panel (b) shows mean polarization. The colors encode the the direction of the polarity and the saturation reflects the magnitude of the polarization. Panel (c) shows mean nematic order. The colors encode the the direction of the nematic order parameter and the saturation denotes their magnitude.*

move in the opposite direction of a larger band. This means that when we look at the system at the scale of the filaments we can see such lane-like structures. Figure 6.7.c shows robust nematic ordering throughout the system, except for the points where topological defects seem to appear.

6.6.1.2 The order parameter correlation in the local frame of reference

For a quantitative analysis of the degree of order in the system, we first calculate both the polar and nematic order parameters. Next, we analyze the spatial correlation functions (for both nematic and polar order) in the frame of reference of filaments. Figure 6.8 shows the order parameter correlation calculated in the frame of reference of a monomer of a filament. It tells us how the correlations decay or grow as we sit on a typical monomer but look further away from it both in the parallel and perpendicular direction. Figure 6.8.a indicates that filaments form a highly periodic structure (crystalline order) in a normal direction due to the high packing fraction. Figure 6.8.b indicates a strong polar correlation in the "west" (90°) and "east" (270°) directions of the filaments. The strong polar correlation means that the filaments have a high
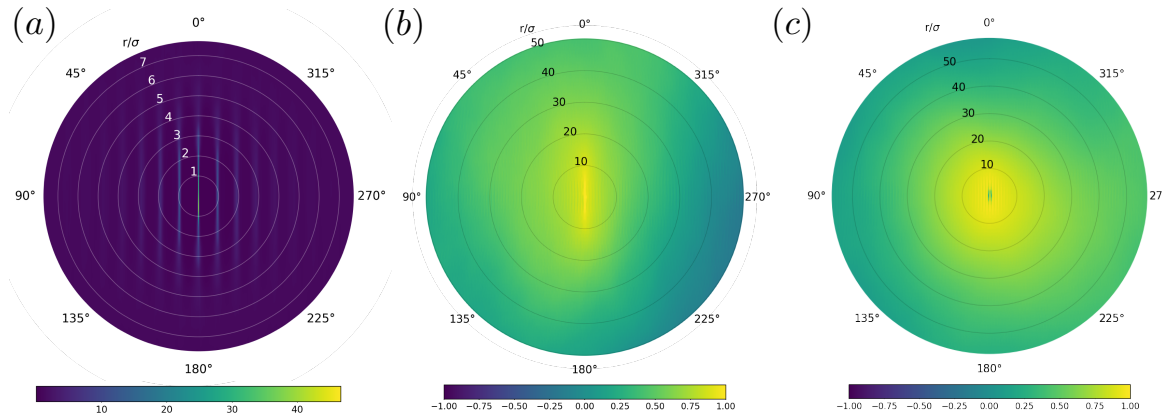
Figure 6.8 – *Order parameter correlation in the frame of reference of the monomers. The north direction (0°) is the tangent vector in the gliding direction of the filament in all plots. Panel (a) Density correlation $\widetilde{S}_{local}$ which shows a crystalline order in the normal direction due to stacking of filaments parallel to each other. Panel (b) Polar orientation correlation which shows a strong but anisotropic correlation. Panel (c) describes presence of a strong nematic orientation correlation.*

tendency to glide in the same direction, which is shown in figure 6.7.b by the large clusters sharing similar color. Figure 6.8.c demonstrates a strong nematic correlation of filaments which is present in both normal and tangential direction direction of the filament.

To gain a better understanding of the correlation of the order parameters we consider only the correlation in the normal and tangential directions. Figure 6.9 shows the spatial correlations of the order parameters (polar and nematic) in the normal (6.9 (a-c)) and tangential (6.9 (e-f)) direction. Similarly, figure 6.9 (a,d) describe the spatial density correlations in the normal and tangential directions, respectively. The presence of sharp peaks in the density spatial auto-correlation 6.9 indicates a crystalline structure in the normal direction of the filaments. This reveals the formation of a dense stacking of filaments in the system. Panels 6.9 (b,e) describe strong polar correlation in both normal and tangential directions. Similarly, one can also observe a strong nematic orientational correlation in figure 6.9 (c,f) in both normal and tangential directions.
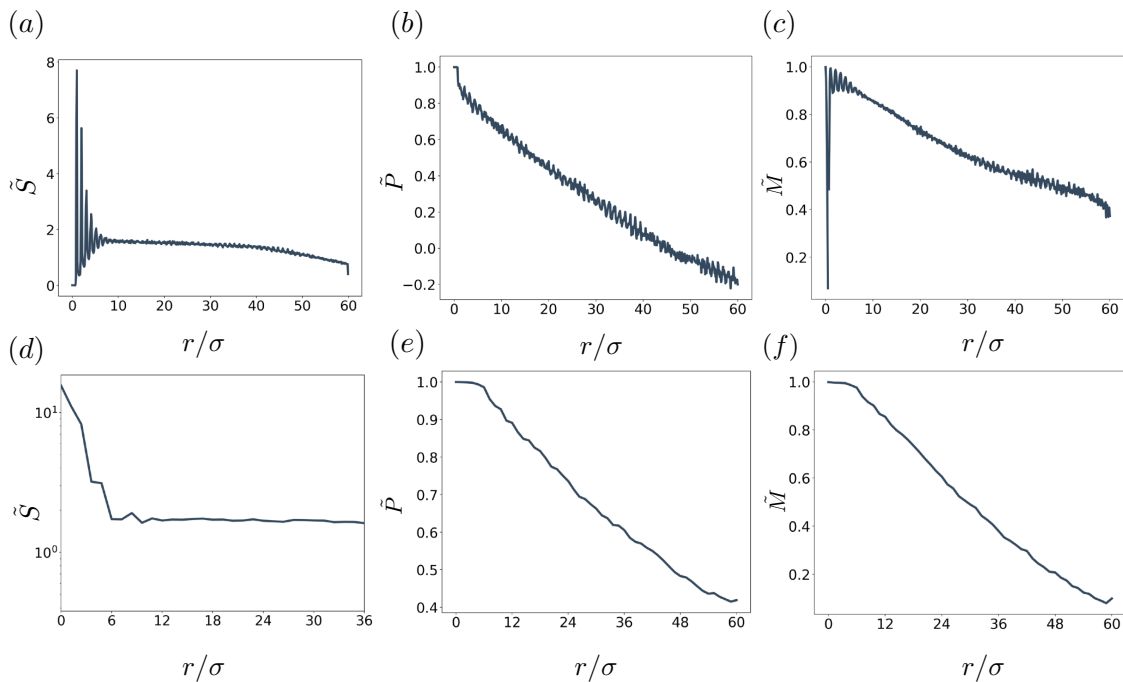
Figure 6.9 – *Order parameter correlation in the reference frame of the monomers for both normal (a-c) and tangential (d-f) directions. Panels (a,d) show the spatial correlations in density, Panels(b,e) the polar spatial correlation and panels(c,f) the spatial correlation of the nematic order.*

Up to now, we have described different aspects of the static and dynamical features observed in the steady-state of a self-propelled filament system. Now, we will explore the effect of velocity reversal dynamics by analyzing similar variables of interest.

6.6.2 Pattern formation with direction reversal dynamics

In this section, we look at the pattern formation of self-propelled filaments with direction reversal incorporated in the dynamics. As mentioned earlier, *Cyanobacteria* can change their gliding direction when the intensity of light in a medium changes. To mimic this behavior we used the same strategy as detailed in chapter 4 and add stochastic reversal dynamics to the motion of the filaments. Under this scheme, filaments change their direction of motion abruptly by 180 ° and these reversals occur according to a Poisson process with rate λ_r. Run length for each filament is a stochastic quantity but
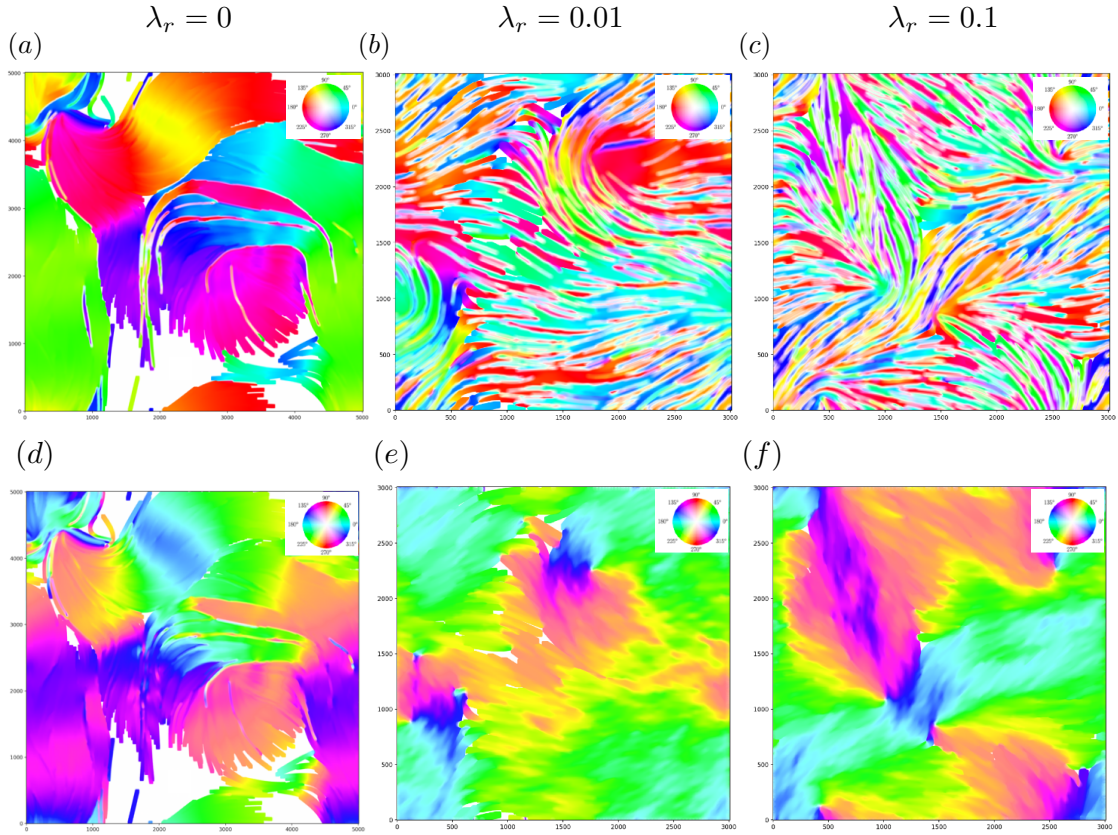
Figure 6.10 – *Panel(a-c) show mean polarization for different reversal rate (λ_r). The colors encode the polar orientation of filaments and the magnitude is encoded by its saturation. Panel (d-f) represents mean nematic order for different reversal rate. As before, the colors encode the nematic order of the filaments and the saturation reflects their magnitude.*

averages to $L_{run} \sim \frac{f_{act}}{\lambda_r \gamma}$.

6.6.2.1 Mean field analysis

We again look at similar physical quantities that reflect the local order in the steady-state generated under the reversal dynamics. Figure 6.10 shows the mean polarization for the same set of parameters as described in the section 6.6.1 and the only difference is the presence of a finite reversal rate in the dynamics of the self-propelled filaments. The mean polarization is plotted in the panels 6.10 (a-c). As one can see in these panels the big polarized bands become thinner as the reversal rate increases in the

system. One can also observe an overwhelming presence of lane-like structures. Overall, with increasing the reversal rate, the bands shrink to become thinner and move in the opposite direction with respect to one another.

The nematic order is only weakly perturbed by the presence of slight reversal dynamics; hence we observe almost equally strong nematic order in the system with reversals compared to its non-reversing counterpart. With increasing reversal rate, to our surprise, the nematic order even seems to grow; a feature completely opposite to the trends seen in the polar order parameter.

Concomitant with an increase in the number of small polar bands, the nematic orientation correlation increases. As the frequency of forward and backward motion rises due to the higher reversal rate, the filaments lose their tendency for polar alignment. However, mostly due to the parallel and antiparallel alignment, during collisions between the filaments, the nematic order in the system grows. As can be seen in figure 6.10 (c,f), the nematic bands become wider with increasing reversal rate.

6.6.2.2 The order parameter correlation in the local frame of reference

Figure 6.11 shows the order parameter correlation in the local contour frame of reference for different reversal rates. As the direction reversal increases, the polar correlation becomes limited to self-correlation, i.e., a filament exhibits a strong correlation with itself, and as the reversal rate increases, the self-correlation becomes stronger.

The polar correlation decreases in both normal and tangential directions compared to the non-reversing case. In the normal direction, it sharply decreases to zero, which means that there is only a strong correlation between a filament and itself.
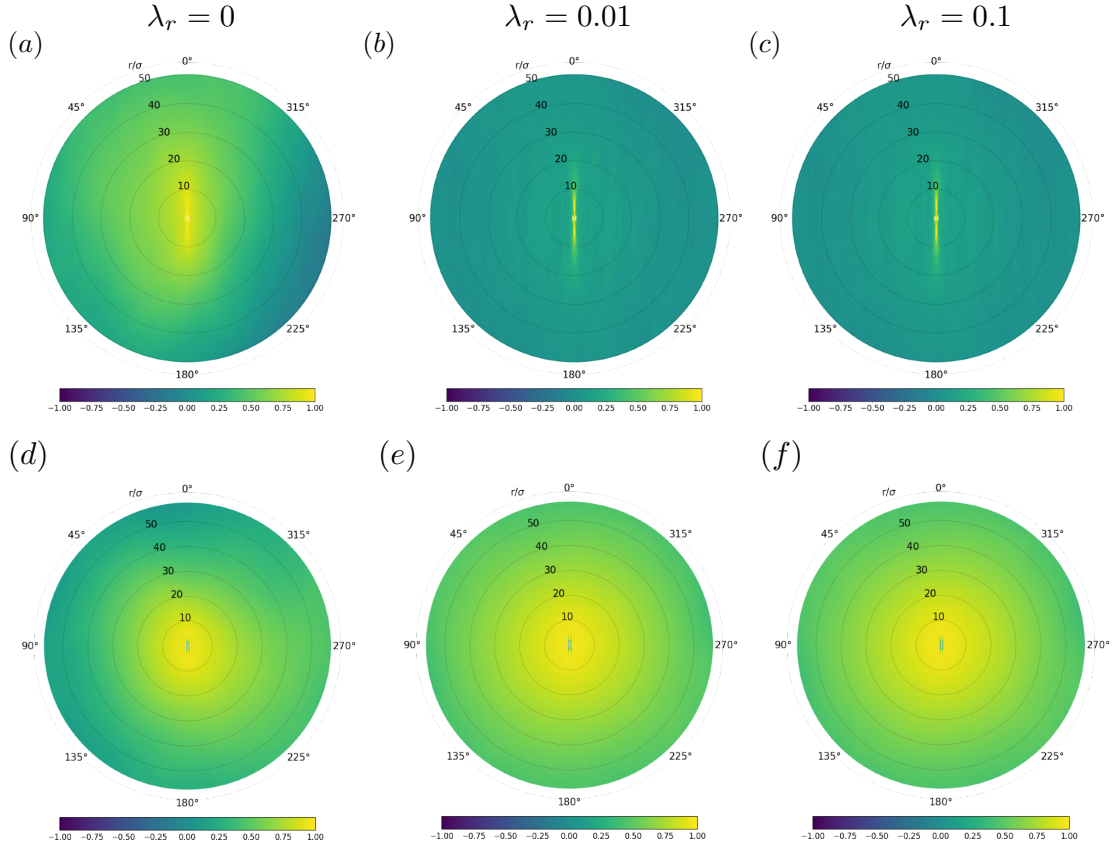
Figure 6.11 – *Panels (a-c) correlation of polar order parameter is plotted as a function of distance r for the whole range of angles between 0 and 2π. The plot shows the correlation is strong mostly against the monomers of the same filament along the tangential direction (i.e. along 0 and π). Nearest neighbors have small tendency to glide in the same direction and the tendency rapidly decreases with increasing reversal rate. Panels (d-f) correlation of nematic order parameter is plotted as a function of distance r for the whole range of angles between 0 and 2π. The figure shows the correlation increases with increasing reversal rate this is in stark contrast to the trends we observed for polar order parameter.*

6.6.3 Aspect Ratio

Another factor that may play an important role in both polar and nematic ordering is the aspect ratio of the filaments. To investigate this factor, we varied the aspect ratio a, keeping all other parameters in the simulation fixed. In addition to the aspect ratio of 30 studied so far, we have simulated two more, one below the critical self-buckling aspect ratio, $a = 10$, and one above $a = 100$.

In the absence of direction reversals , for the lower aspect ratio, $a = 10$, we still
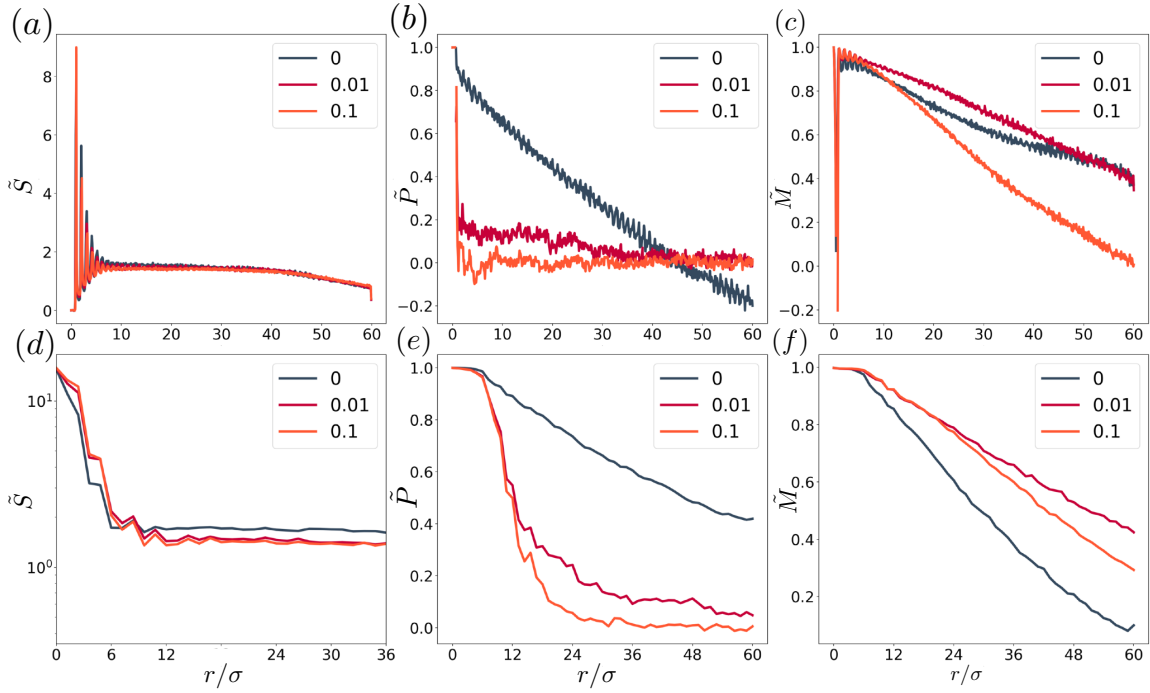
Figure 6.12 – *Order parameter correlation in particle reference frame in normal (a-c) and tangential (d-f) direction. Panels (a,d) density correlation, Panels(b,e) polarization correlation, Panels(c,f) nematic orientational correlation for aspect ratio 32 at different reversal rate.*

observe a clear transition from a disordered to ordered state, and the system starts to self-aggregate 6.13. We notice that at a lower aspect ratio, there is a nematic-smectic transition as well which can be seen in Figure 6.13. b. There is a short-range positional order of filaments in the tangential direction in addition to its normal direction. With increasing aspect ratio there is an increase of polar clusters in the systems due to the effective velocity alignment. These polar clusters can become large and even percolate the system, forming the so-called polar bands. Within the bands, the filaments are densely packed and point in the same direction which can be seen in the mean-field representation of the system in the figure 6.14.
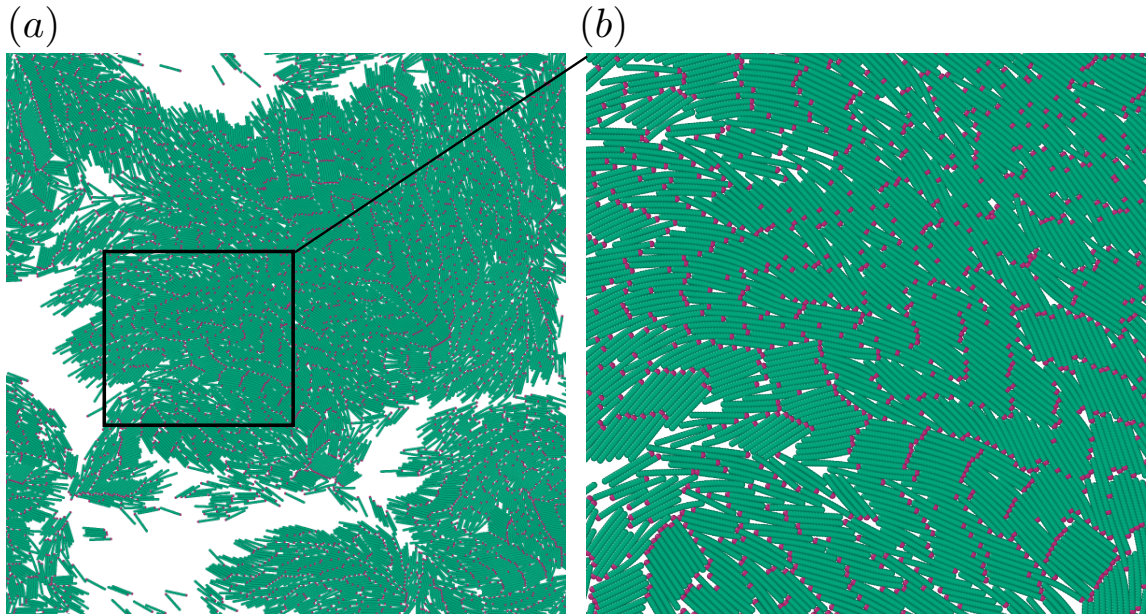
Figure 6.13 – *Snapshot of the configuration of filaments with an aspect ratio of $a = 10$. Panel (a) Filaments develop a short-range positional order in the tangential direction in addition to the normal direction. Panel (b) Magnified view of the snapshot. (Purple illustrates the head of the filament, the direction of filament motion.)*

6.6.3.1 Mean field analysis

We first look at the polar order parameter profiles across the system for different reversal rates and also for different aspect ratios of the filaments. Figure 6.14 shows that polar order (same density as before, $\rho = 0.7$) tends to decrease with an increase in reversal rate and one can also observe the presence of lane-like structure when both reversal rate and aspect ratio are high. In the case of non-reversed direction, the average polarization increases with increasing aspect ratio. A high polarization in the system also means the formation of large bands that point in the same direction and move together. In the presence of direction reversal dynamics, the polar bands shrink due to the stochastic switching of the direction of the filaments, and do not remain as densely packed as in the non-reversing case. At a fixed reversal rate, the local lane structures are more pronounced with increasing aspect ratio and there are weak polar bands that move in the opposite direction (lane-like structure). We first
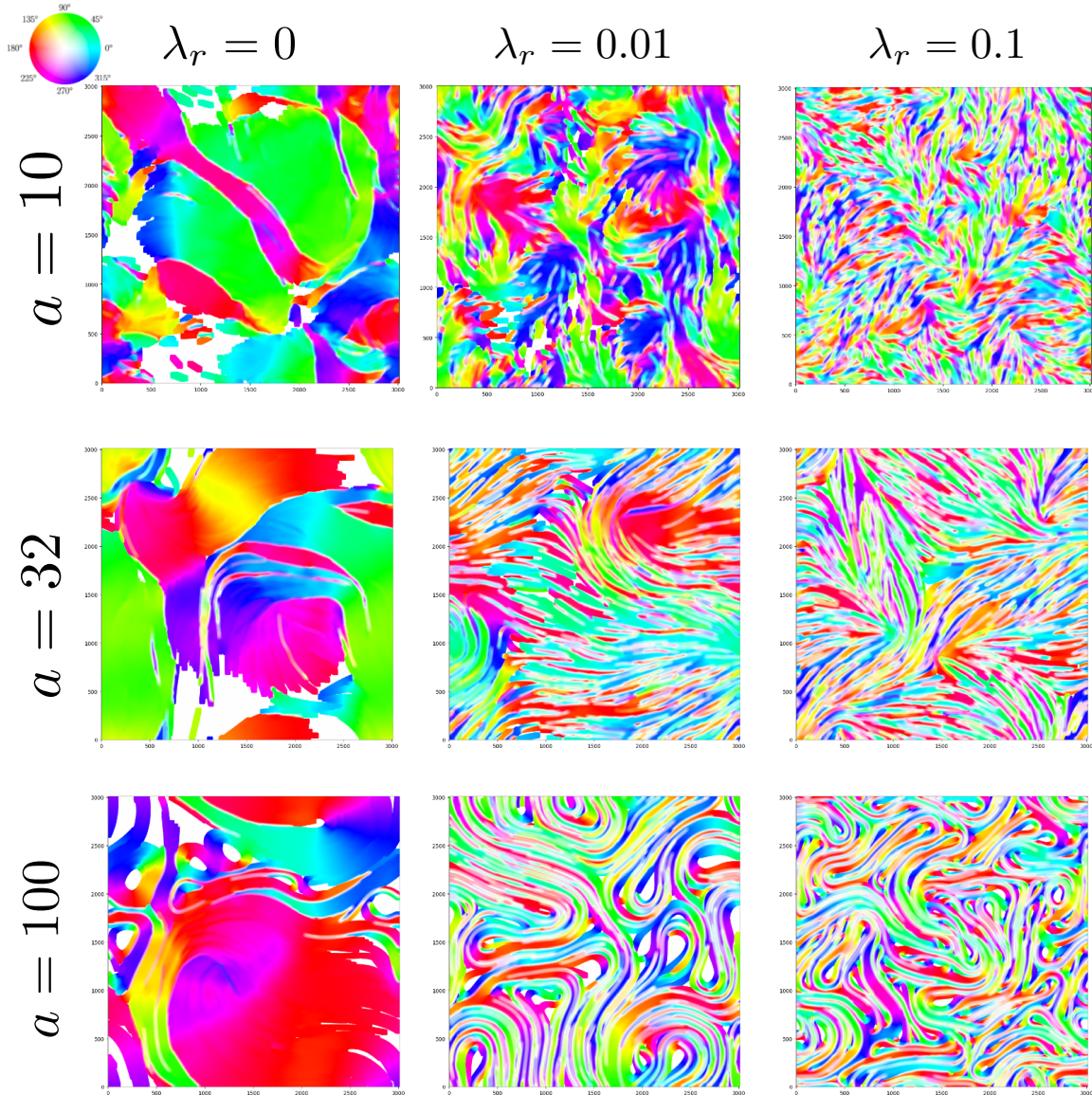
Figure 6.14 – *Polar order has been explored by colouring the particles according to their orientation at different reversal direction rates for different aspect ratios of the filaments. The plots show polar order tends to decrease with an increase in reversal rate and one can also observe the presence of lane-like structure when both reversal rate and aspect ratio are high.*

observe that nematic order tends to increase strongly with an increase in reversal rate for a small aspect ratio. For the intermediate aspect ratio, $a = 32$, the mean nematicity increases with increasing reversal rate. The run length for higher reversal rate becomes smaller ($L_{run} \sim \frac{f_{act}}{\lambda_r \gamma}, \rightarrow L_{run} \sim 1/\lambda$), therefore they often move forward and backward
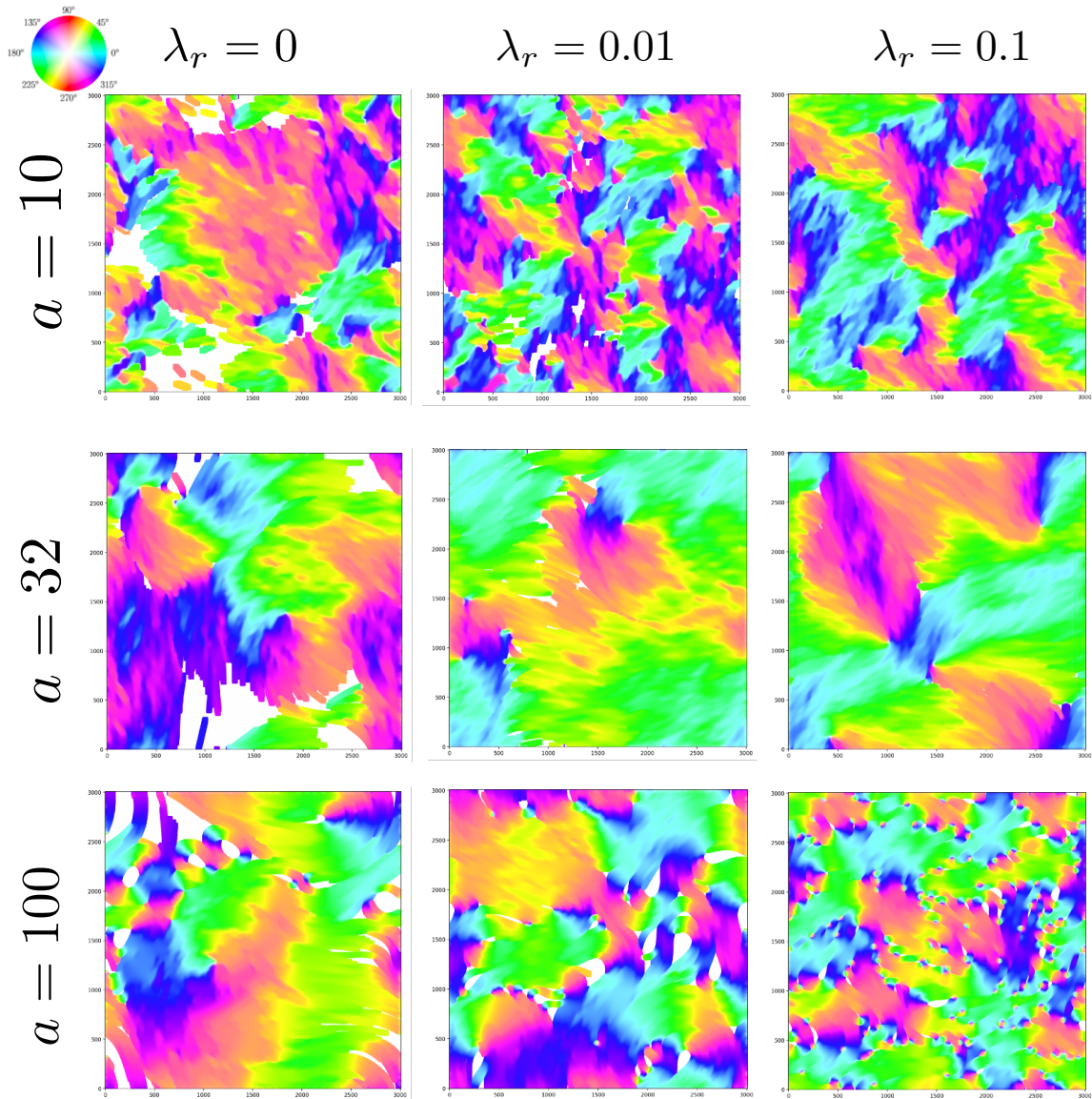
Figure 6.15 – *Presence of nematic order has been demonstrated by colouring the angle of the director at different reversal direction rates for different aspect ratios of the filaments. The plots indicate nematic order tends to increase strongly with an increase in reversal rate and this trend is quite opposite to the polar order. At a high aspect ratio density of topological defects also seems to increase with an increase in reversal rate.*

in coordinated fashion. Collision makes their direction more parallel (or antiparallel), resulting in higher local nematic order. On the other hand, for a higher aspect ratio, *e.g.* $a = 100$, nematic order decreases with increasing reversal rate. In short, the mean nematic order becomes more localized as the run length of the filaments decreases due

Figure 6.16 – *Correlation of polar order parameter is plotted as a function of distance r for the whole range of angles between 0 and 2π. The plot shows the correlation is strong mostly against the monomers of the same filament along the tangential direction (i.e. along 0 and π). Nearest neighbors have small tendency to glide in the same direction and the tendency rapidly decreases with increasing reversal rate.*

to a higher reversal rate (Figure 6.15 lower right panel).

6.6.3.2 The order parameter correlation in the local frame of reference

Figure 6.17 indicates that in the absence of direction reversal dynamics, strong polar order exists for all different aspect ratios we have studied. Moreover, the order becomes

stronger with aspect ratio. In other words, with increasing aspect ratio, polar bands in the system grow wider and move together more coherently. This can also be concluded from the analysis of the correlation of the polar order parameter. As it can be seen in figure 6.16, the polar correlations, in both normal and tangential directions, increase with increasing aspect ratio in the absence of reversals. However, with increasing reversal rate, the polar order seems to weaken significantly and is limited to the scale of a few filaments. Increasing aspect ratio amplifies the polar and nematic correlation in the system. However, as the reversal rate increases, the steady-state polar bands in the system shrink in width in comparison to the bands for the non-reversal case.

In Figure 6.18 (b,c), we observe an abrupt change in the polar correlation in the normal direction when the direction reversal dynamics is applied. As the reversal rate increases, the polar correlation decreases for all aspect ratios and it is mostly limited to just a few filaments. In comparison to the normal direction, the change in the tangential direction is smooth and it decays gradually compared to the non-reversing case (see figure 6.18 (e,f)). Surprisingly, the trend with increasing aspect ratio is non-monotonic and for aspect ratio $a = 32$ which is the critical aspect ratio for self-buckling we get the highest correlation in the tangential direction.

The nematic correlation in the normal direction (see figure 6.19 (b,c)) also increases with increasing aspect ratio in the absence of direction reversal dynamics. In the tangential direction (see figure 6.19 (e,f)), there is an increase from aspect ratio 10 to aspect ratio 32 and it remains almost unchanged from aspect ratio 32 to 100. Compared to the polar correlation, applying reversal direction doesn't have an abrupt decrease in the nematic correlation rather there is a signature of increasing correlation, most visible for the critical aspect ratio $a = 32$.

To explore the applicability of our result we also compare our observations with the experimental system developed in Dr. Stefan Karpitschka's lab at the Max Planck
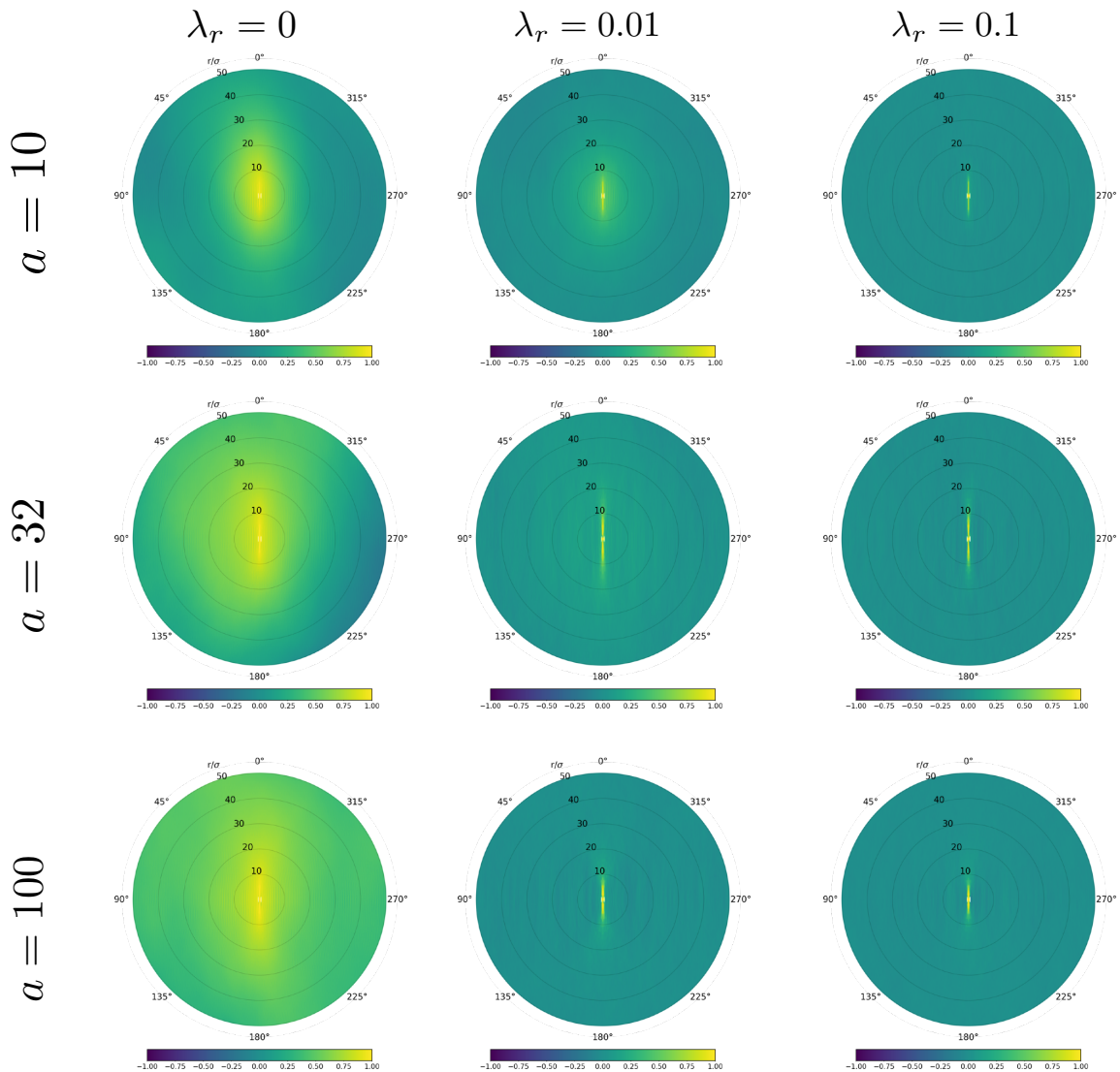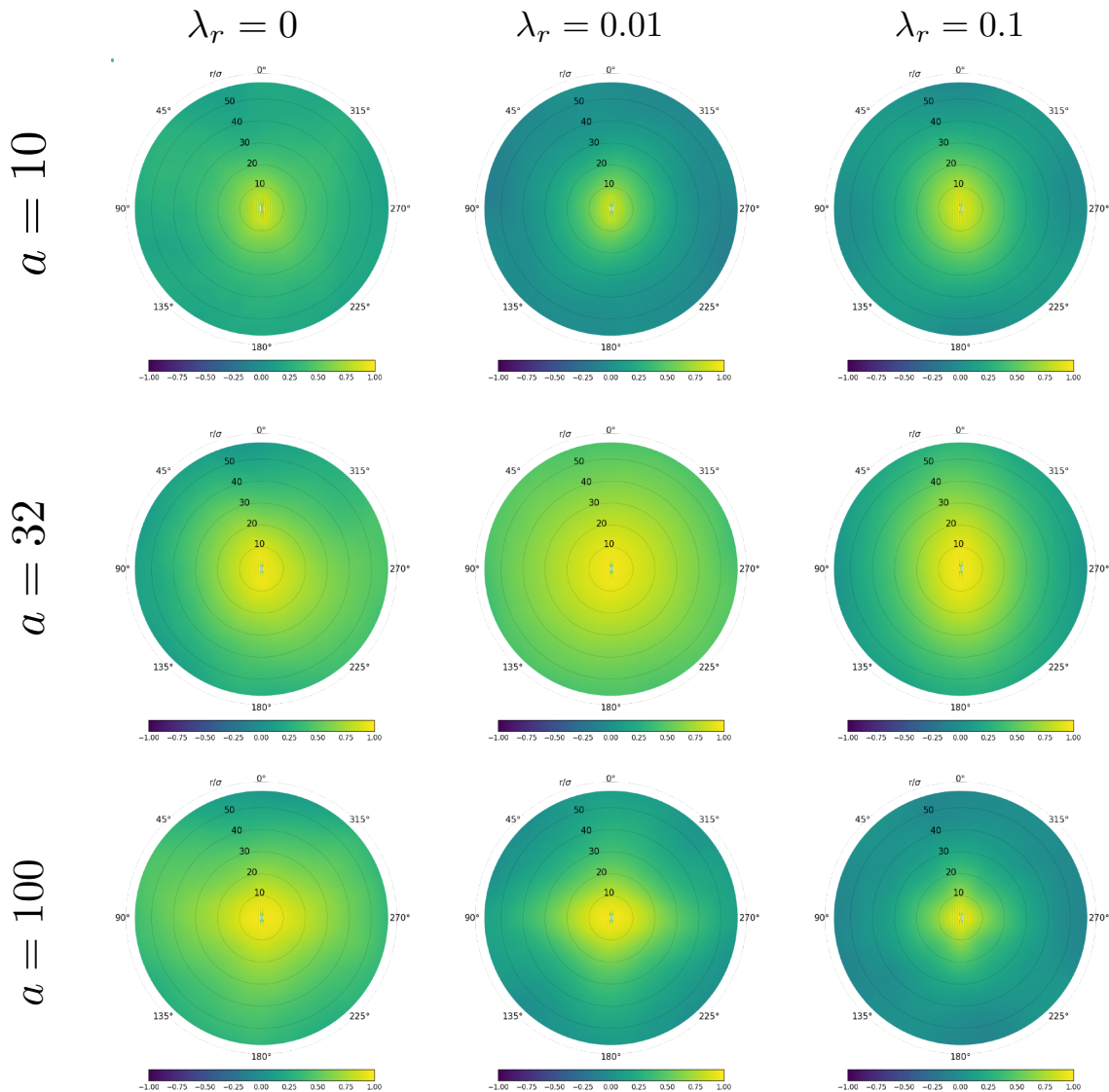
Figure 6.17 – *Correlation of nematic order parameter is plotted as a function of distance r for the whole range of angles between 0 and 2π. The figure shows the correlation increases with increasing aspect ratio. The correlation seems to increase (especially for critical aspect ratio) with increasing reversal rate and this is in stark contrast to the trends we observed for polar order parameter.*

Institute for Dynamics and Self-Organization. We will discuss in the next section the analysis of order parameters and other relevant quantities from the experimental data. All the plots are taken from a preliminary draft with the permission of Dr. Stefan Karpitschka.
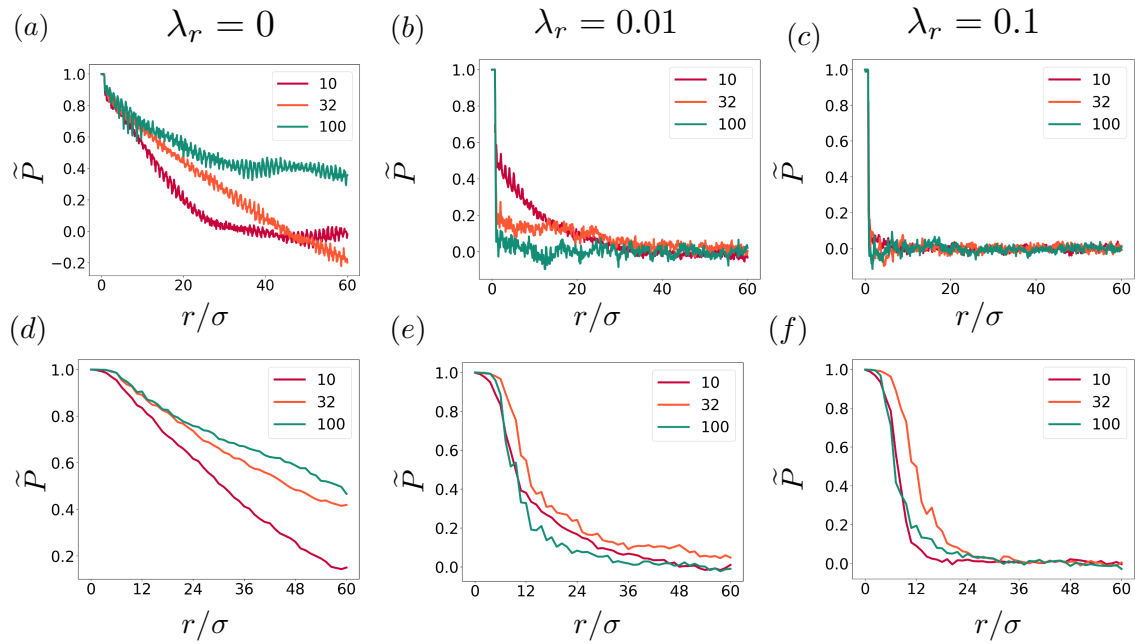
Figure 6.18 – *Polar correlation in the reference frame of monomer in normal (a-c) and tangential (d-f) direction at different aspect ratio and reversal rate. The colors encode different aspect ratios and the corresponding reversal rate for each set is written at the top of the respective column.*

6.7 Evaluation of order parameters and mean fields from experiments

Figure 6.20.a shows a snapshot of a monolayer experiment with *Kamptonema animale* using brightfield transmission microscopy imaging technique. Panel 6.20.b shows the filament velocity prediction for panel 6.20.a compared to the next frame, one second later, where the colors indicate the orientation of the velocity vector. From the color code, one can see that there is polar ordering where filaments in the polar bands move collectively and coherently (Figure 6.21.b). The polar bands also move opposite to each other and form lane-like structures that we also observed in the simulation, as represented in figure 6.14.

As evident in the mean field analysis in figure 6.21 (c), the nematic order is everywhere in the band. In the band structure, the mean density is nonzero and it
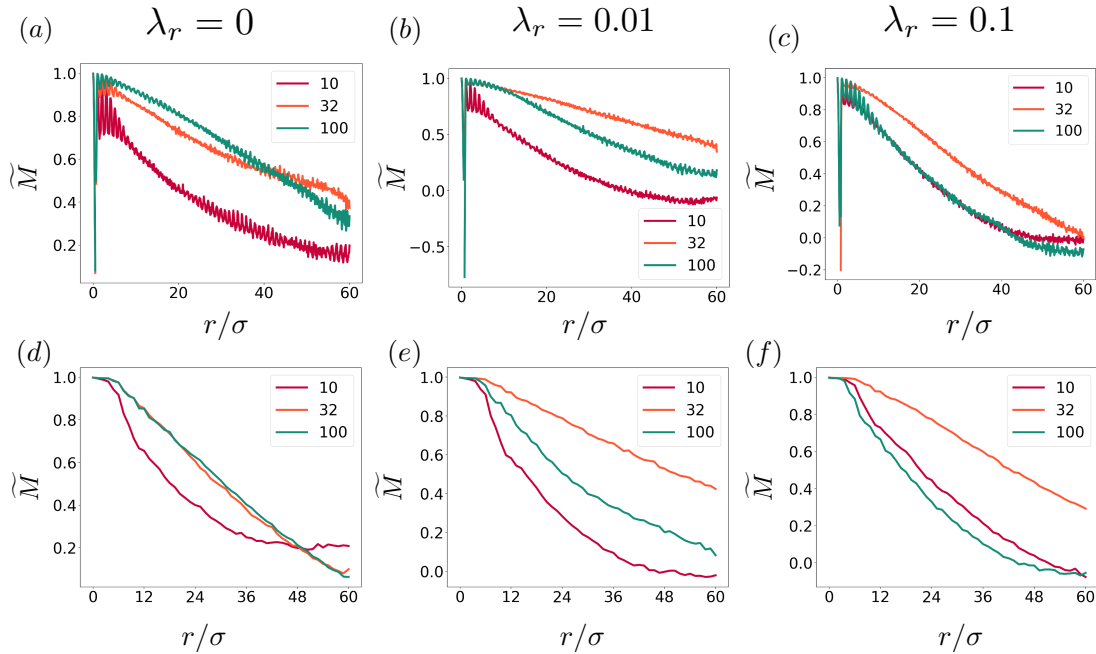
Figure 6.19 – *Nematic correlation in particle reference frame in normal (a-c) and tangential (d-f) directions at different aspect ratios and reversal rates. The colors encode the aspect ratio and the corresponding reversal rate for each chart at the top of the respective column.*

varies locally(Figure 6.21 (a)).

Figure 6.22 shows the correlation of the order parameters in the local contour frame. Panel 6.22.a indicates that a crystalline order in the normal direction is formed by the filaments. Panel 6.22.a demonstrates a strong polar correlation along the contour of a filament which is the evidence for the strong correlation of a filament with itself. This is similar to the polar correlation observed in the simulations of the case with direction reversals (figure 6.14). This observation is associated with the capability of the filamentous *Cyanobacteria* to do reversals which makes them form distinct polar bands compared to the non-reversing bacteria. Remarkably, this shows that in *Cyanobacteria*, in addition to their systematic movement, there is also a stochastic reversal of direction.

The nematic correlation is also strong in the normal direction of the filaments,
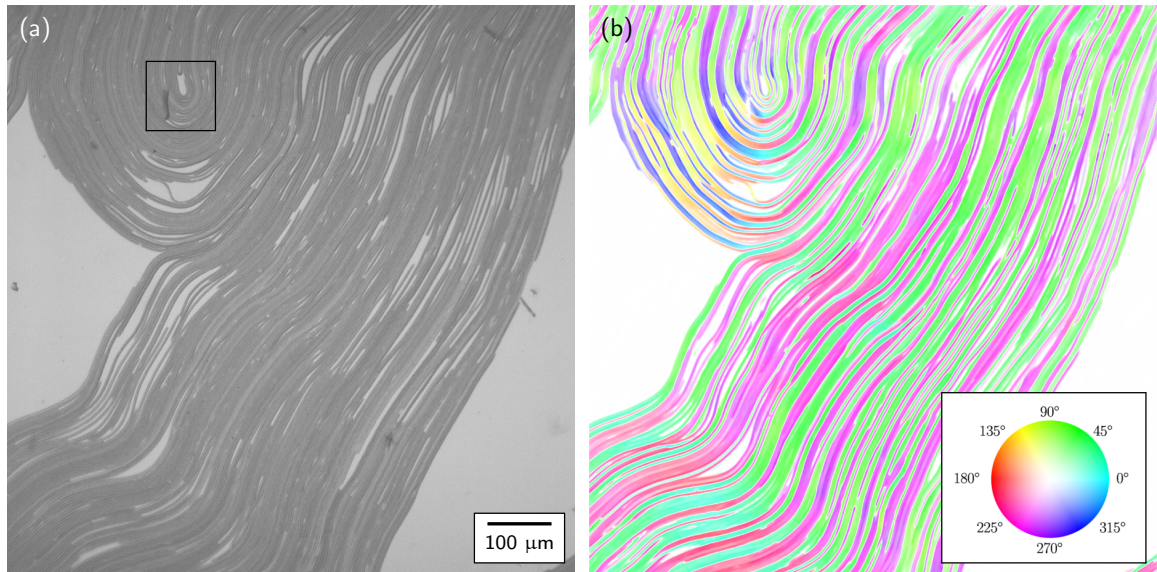
Figure 6.20 – *a) Brightfield transmission micrograph of an experiment with Kamptonema animale. b) Filament velocity prediction, color coded orientation, and the magnitude of the velocity is represented by the saturation (full saturation corresponds to $3.5\mu m/s$). The plots are taken from a preliminary draft of a paper, which is part of the experimental data with permission from Dr. Karpitschka.*
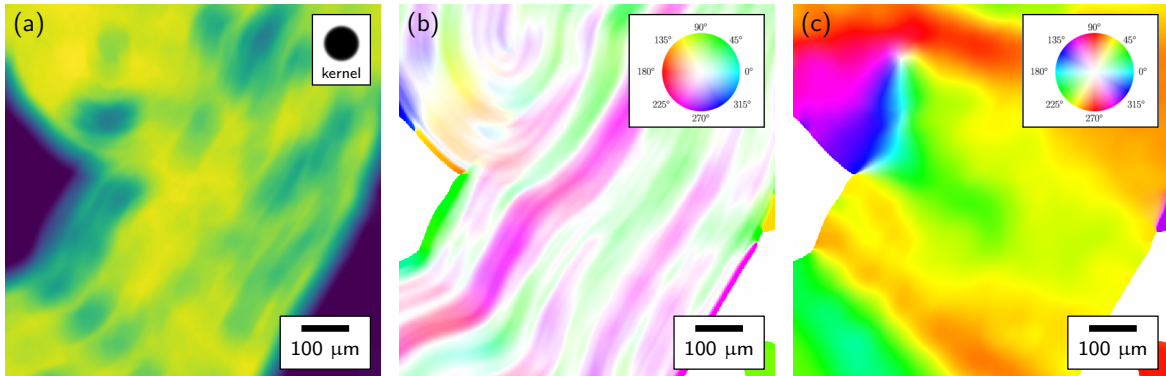
Figure 6.21 – *Mean fields of an experiment with Kamptonema animale. a) Mean density. The kernel for averaging is given on the top-left inset. b) Mean polarization. The color indicates the orientation of the individual monomers on the filamenet, the saturation of this color shows the strength of the polarization. The color code is given on the top-left inset. c) Mean nematicity, analogous to (b). The plots are taken from a preliminary draft of a paper, which is part of the experimental data with permission from Dr. Karpitschka.*

indicating that the filaments are mostly in parallel and antiparallel orientations, forming a monolayer.

Figure 6.23 shows the correlation length in the normal and tangential directions. The

131
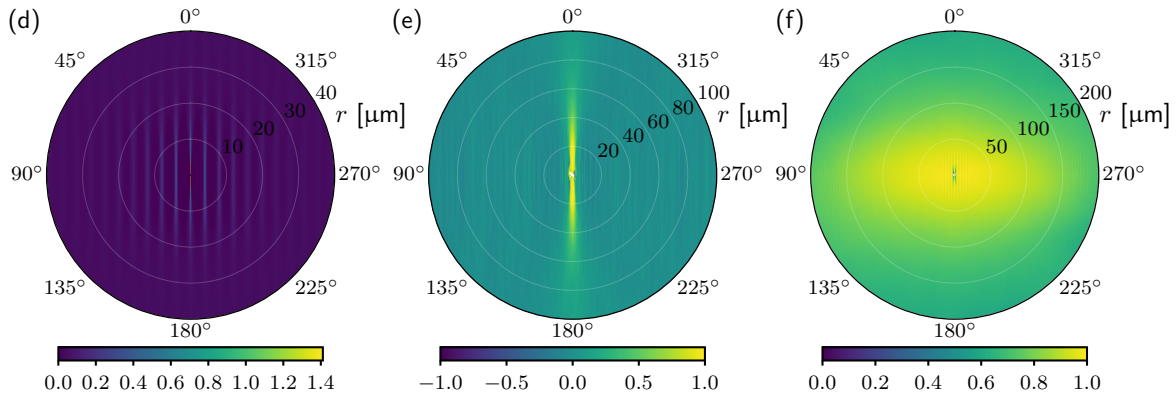
Figure 6.22 – *Order parameter correlations in the local contour frame of reference for an experiment with Kamptonema animale. The tangent vector in gliding direction is oriented to the north (0^{deg}) in the plots. a) Density correlation $\widetilde{S}_{local}$, showing crystalline order in normal direction within ~ 20 neighboring filaments. b) Polar orientation correlation p_{local}, showing strong correlation of gliding direction only between a filament and itself. c) Nematic orientation correlation m_{local}, showing the long-range nematic order of the structure. The plots are taken from a preliminary draft of a paper , which is part of the experimental data with permission from Dr. Karpitschka.*

nematic correlation length (Figure 6.23.c) is larger in the normal direction compared to the tangential direction in Figure 6.23.d.

Moreover, the polar order in Figure 6.23.b drops abruptly to zero in the normal direction, in contrast to the tangential direction (Figure 6.23).e), which decreases gradually to zero. This shows that the polar correlation in the system is strongly limited to a filament. This is a consequence of the reversals of the direction of motion. The filaments align through collisions, but this alignment strengthens their nematic correlation rather than their polar correlation because of their random backward and forward motion, which leads to the loss of polar order after alignment.

6.8 Conclusion

In summary, we employed an overdamped Brownian dynamics simulation to study the pattern formation in a system of self-propelled semi-flexible filaments that mimic *Cyanobacteria* colonies studied in the experiment. To attain a better understanding of
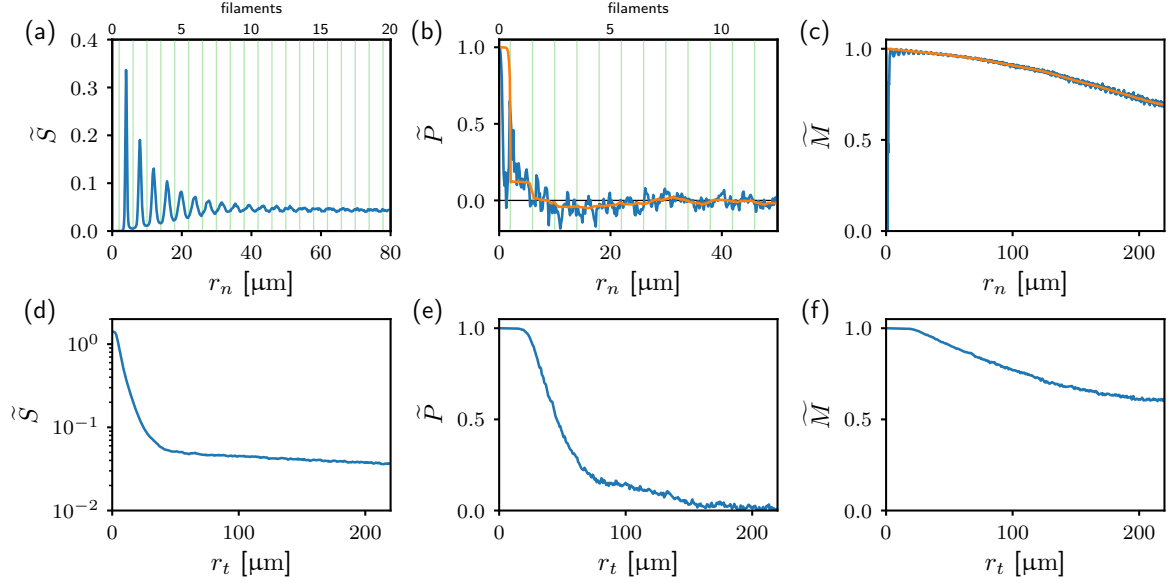
Figure 6.23 – *Order parameter correlations in the local contour frame of reference for an experiment with Kamptonema animale, in normal (a-c) and tangential (d-f) directions. (a,d): density correlation. (b,e): polarization correlation. (c,f): nematic orientational correlation. Orange lines in (b) and (c) are the moving mean with a window that corresponds to the width of one filament. The plots are taken from a preliminary draft of a paper , which is part of the experimental data with permission from Dr. Karpitschka.*

the pattern formation, we first simulated a dense assembly of active (self-propelled) filaments with parameters that are obtained by the experiments: the critical aspect ratio for self-buckling, the self-propulsion force, the friction coefficient, and also the bending stiffness. The simulations were performed at a relatively high density where steric interactions become important. We also include a stochastic direction reversal mechanism which is one of the unique dynamical characteristics of *Cyanobacteria* and can typically be observed due to local changes in the light intensity in the environment.

In the absence of the direction reversal dynamics, we first described different aspects of the static and dynamical features observed in the steady-state. The steady-state shows the appearance of spectacular giant polar clusters within which one can observe densely packed filaments (with a highly periodic structure) that point towards the same direction and move coherently. We also analyzed the nematic order along with the polar order and showed that the system possesses a strong nematic order in the

steady-state. We investigated the spatial correlation of the above-mentioned order parameters in the $r - \theta$ plane.

We then examined the effects of the velocity reversal dynamics by analyzing similar variables of interest. As the velocity reversal rate increases, the polar bands shrink in width and lane-like structures start to form locally. The polar correlation decays more rapidly as a function of space with an increasing reversal rate, but quite surprisingly the nematic order tends to increase with the faster reversal. To explore the role of the filament structure we examined the effects of aspect ratio on such structural order in a steady state. At a lower aspect ratio ($a = 10$), we observed a smectic phase. As the aspect ratio increases, both the polar correlation and the nematic correlation grow and the effect can be observed in both normal and tangential directions. In the presence of direction reversal dynamics, the polar correlation decreases abruptly in the normal direction of the filaments, whereas it decreases slowly and non-monotonically in the tangential direction. The aspect ratio $a = 32$ (which is also the critical aspect ratio for the filaments) displayed the largest correlation length compared to the other two ($a = 10, 100$) in each reversal rate. The nematic correlation decays slowly and nonmonotonically in both the normal and the tangential directions, and like the polar correlation, the aspect ratio $a = 32$ has the largest nematic correlation length.

Finally, we compared our results with experimental data obtained from Dr. Karpitschka's lab and observe excellent qualitative agreement for colonies of active filaments with direction reversal dynamics. Similar to the simulations, there is an abrupt drop in polar correlation in the normal direction and a slow decay in the tangential direction in the experiments. Moreover, the existence of a large nematic correlation length has also been confirmed in the simulations in the presence of reversal dynamics.

Chapter 7

Discussion and Conclusions

In this thesis we have discussed a special class of out-of equilibrium system, known as *active matter* that mimics systems in the biological world around us from a statistical mechanical point of view. We discussed in details a few models of such active matter systems with the aim to describe the spectacular dynamics and self organisation that can be observed in such model systems. Below I discuss the key points and ideas that we explored in a chapter wise format.

Non-equilibrium statistical mechanics has opened a new door to approach the fascinating world of living matter physics. Despite remarkable advances in the physics of living matter in recent decades, collective dynamics and emergent complex behaviour of most biological systems still remains elusive. In the Introduction chapter I have discussed the most popular models of active matter system, their classification and characterisation. The dazzling and enigmatic nature of living systems has provoked tremendous enthusiasm among scientists to endeavor to shed light on the mechanism behind their collective behaviour such as swarming or motility induced phase separation.

In chapter 2, we have studied the diffusive motion of a "tracer" particle in a system of using a simple (hexagonal) lattice model where the tracer is being pushed by active particles and this leads to enhanced diffusion. We have shown that the degree to which

this diffusion is enhanced depends crucially on two factors: (a) activity of the crowders (b) density of the crowders. The change with respect to the density of the crowders is non-monotonic. This non-monotonic response can be attributed to the formation of clusters of active particles in the system which is revealed through analysis of the cluster statistics. To put it simply, initially the diffusion constant of the tracer increases as the tracer is subject to stronger fluctuations in the presence of a higher density of pushing active particles, but at large density decreases again, as the formation of clusters of active particles induces 'caging' of the tracer in the clusters and slows down the dynamics outside the clusters. Overall our findings point to the intricate interplay of fluctuations and crowding, both controlled by the density of active crowders and reproduces an 'enhanced diffusion with crowding' scenario in a simple lattice based model.

In chapter 3, we employed a Brownian dynamics simulation in continuous space to explore the strong velocity correlation in a mixture of active and passive particles. Caprini *et al.* [59] and Henkes *et al.* [60] have reported very recently that there is a 'hidden' strong velocity correlation (in the absence of alignment interaction) in a dense active-solid or liquid like system. Note that such systems do not show long range polar order of the propulsion forces in the absence of alignment. The correlation length reported in [59–61] scale with the square root of the persistence time of the particles in the system. This motivated us to explore the question whether such correlations can be induced in a dense passive system by a small fraction of active particles. This study can potentially decouple the effect caused by high density of the medium from the one caused by the persistent activity of the self-propelled particles. Surprisingly, our results show that even a very tiny fraction of active particles in a dense medium (which consists of a sufficiently high density of passive particles) plays a significant role in forming domains with strong velocity-correlation of the particles. Moreover, the size

of this domain grows with increasing area fraction of passive particles in the system and finally saturates at the maximum length-scale available in the system *i.e.* the system size. In addition to that, we have explored the effects of activity parameters, *i.e.* (i) the self-propulsion force and (ii) the persistence time on such strong velocity correlations generated in the passive system by introducing a tiny fraction of active dopants. Incredibly,our results showed that the correlation length scales with the square root of the persistence time of the active particles in the system, which is consistent with other studies for purely active systems [59–61].

In chapter 4, we have tried to extend our understanding of pattern formation in an active matter system by considering an assembly of anisotropic self-propelled objects such as active polymers. We used an overdamped Brownian dynamic simulation to explore the various dynamical states in the system. It has been demonstrated that their self propulsion ability (f_a) and bending stiffness (κ_b) are the key players controlling the size and shape of the emergent clusters and the dynamical steady states in the system. We also analysed the cluster size and spiral ratio and show how these variables depend on the relevant parameters. Later, we added a direction reversal mechanism to the polymers to mimic the stochastic direction switching motion of filaments. The stochastic direction reversal rate is another key parameter that controls the emergence of clusters and spirals in the system. Using extensive numerical simulations we have shown that the reversal dynamics overall decreases both clustering and spiraling tendencies.

In chapter 5, we explored the physics of buckling for individual self-propelled filament to make a comparison with experimental data and theoretical model developed in Dr. Stefan Karpitschka's lab at the Max Planck Institute for Dynamics and Self-Organization. We extracted parameters from this study to investigate the pattern formation of filamentous *Cyanobacteria* in the next chapter.

In chapter 6, similar to the previous chapter, we have employed a Brownian dynamics simulation of active polymers at a high density and study the nematic and polar order in the system. We also extracted relevant parameters for simulation from experiments using the colonies of *Cyanobacteria*. We first confirmed that a critical length of *Cyanobacteria* is required to for buckling of them. Using this critical length as well as a length below and above this critical length, the polar and nematic long-range order in the system is then investigated. The active filaments without stochastic direction reversal show a longer-range orientation order compared to that in the presence of reversals. Increasing the reversal rate lowers the polar order in the system. Remarkably, filaments with an aspect ratio above the critical aspect ratio for buckling show a stronger polar and nematic order in the system, compared to the aspect ratio that is below it.

In conclusion, we have employed different models to explore the dynamics and self-organization of isotropic active Brownian particles as well as rod-shaped active filaments. We have reported a rich collective behavior and dynamics in each system as a function of activity parameters and density. Considering all the works that we have done in this thesis, my scientific curiosity has piqued my interest and passion to understand more this bewildering field to leave no stone unturned to extend these works.

Indeed several extensions of the work done in this thesis have already been initiated. In this regard, using the hexagonal lattice model in chapter 2, we have already implemented an aligning interaction between the active particles, similar to the Vicsek model. We will study the effects of aligned active particles at different densities on the dynamics of the passive particles in the system.

To deepen our understanding of strong velocity correlation in a dense passive system generated by active dopants in chapter 3, we plan to construct a theoretical analysis

in collaboration with Prof. Dr. Peter Sollich's group at the Institute for Theoretical Physics to see whether the velocity correlation function can be written as a function of ϕ_a, ϕ_p, etc. It would be of tremendous interest to obtain experimental evidence of such velocity correlations as well. An ideal system could be mixtures of equally sized active and passive colloidal particles, with the active particles coated with a carbon layer by sputtering from one side (Janus particles) [120, 180].

To acquire more insight into the captivating life of *Cyanobacteria*, we plan to perform further analyses to identify and track the topological defects that emerge in dense colonies of *Cyanobacteria*, to explore key parameters for controlling them and to understand the potential role of these defects in the dynamics of bacterial colonies.

References

[1]   A. A. Hyman and E. Karsenti. "Morphogenetic properties of microtubules and mitotic spindle assembly". In: *Cell* 84.3 (1996), pp. 401–410. DOI: 10.1016/s0092-8674(00)81285-4.

[2]   F. Ndlec, T. Surrey, A. C. Maggs, and S. Leibler. "Self-organization of microtubules and motors". In: *Nature* 389.6648 (1997), pp. 305–308. DOI: 10.1038/38532.

[3]   T. Surrey, F. Nédélec, S. Leibler, and E. Karsenti. "Physical properties determining self-organization of motors and microtubules". In: *Science* 292.5519 (2001), pp. 1167–1171. DOI: 10.1126/science.1059758.

[4]   N. H. Mendelson, A. Bourque, K. Wilkening, K. R. Anderson, and J. C. Watkins. "Organized Cell Swimming Motions in Bacillus subtilis Colonies: Patterns of Short-Lived Whirls and Jets". In: *American Society for Microbiology Journals* 181.2 (1999), pp. 600–609. DOI: 10.1128/JB.181.2.600-609.1999.

[5]   J. K. Parrish, S. V. Viscido, and D. Grunbaum. "Self-organized fish schools: an examination of emergent properties". In: *The biological bulletin* 202.3 (2002), pp. 296–305. DOI: 10.2307/1543482.

[6]   C. Dombrowski, L. Cisneros, S. Chatkaew, R. E. Goldstein, and J. O. Kessler. "Self-Concentration and Large-Scale Coherence in Bacterial Dynamics". In: *Phys. Rev. Lett.* 93 (9 Aug. 2004), p. 098103. DOI: 10.1103/PhysRevLett.93.098103.

[7]   A. Cavagna, A. Cimarelli, I. Giardina, G. Parisi, R. Santagati, F. Stefanini, and M. Viale. "Scale-free correlations in starling flocks". In: *Proceedings of the National Academy of Sciences* 107.26 (2010), pp. 11865–11870. DOI: 10.1073/pnas.1005766107. eprint: https://www.pnas.org/content/107/26/11865.full.pdf.

[8]   W. Bialek, A. Cavagna, I. Giardina, T. Mora, E. Silvestri, M. Viale, and A. M. Walczak. "Statistical mechanics for natural flocks of birds". In: *Proceedings of the National Academy of Sciences* 109.13 (2012), pp. 4786–4791. DOI: 10.1073/pnas.1118633109. eprint: https://www.pnas.org/content/109/13/4786.full.pdf.

[9]   A. Cavagna and I. Giardina. "Bird Flocks as Condensed Matter". In: *Annual Review of Condensed Matter Physics* 5.1 (2014), pp. 183–207. DOI: 10.1146/annurev-conmatphys-031113-133834. eprint: https://doi.org/10.1146/annurev-conmatphys-031113-133834.

[10]   M. C. Marchetti, J. F. Joanny, S. Ramaswamy, T. B. Liverpool, J. Prost, M. Rao, and R. A. Simha. "Hydrodynamics of soft active matter". In: *Rev. Mod. Phys.* 85 (3 July 2013), pp. 1143–1189. DOI: 10.1103/RevModPhys.85.1143.

[11] M. E. Cates and J. Tailleur. "Motility-Induced Phase Separation". In: *Annual Review of Condensed Matter Physics* 6.1 (2015), pp. 219–244. DOI: 10.1146/annurev-conmatphys-031214-014710. eprint: https://doi.org/10.1146/annurev-conmatphys-031214-014710.

[12] C. Bechinger, R. Di Leonardo, H. Löwen, C. Reichhardt, G. Volpe, and G. Volpe. "Active particles in complex and crowded environments". In: *Rev. Mod. Phys.* 88 (4 Nov. 2016), p. 045006. DOI: 10.1103/RevModPhys.88.045006.

[13] K. D. Nnetu, M. Knorr, D. Strehle, M. Zink, and J. A. Käs. "Directed persistent motion maintains sheet integrity during multi-cellular spreading and migration". In: *Soft Matter* 8 (26 2012), pp. 6913–6921. DOI: 10.1039/C2SM07208D.

[14] L. Petitjean, M. Reffay, E. Grasland-Mongrain, M. Poujade, B. Ladoux, A. Buguin, and P. Silberzan. "Velocity Fields in a Collectively Migrating Epithelium". In: *Biophysical Journal* 98.9 (2010), pp. 1790–1800. DOI: https://doi.org/10.1016/j.bpj.2010.01.030.

[15] B. Liebchen and H. Löwen. "Synthetic Chemotaxis and Collective Behavior in Active Matter". In: *Accounts of Chemical Research* 51.12 (2018), pp. 2982–2990. DOI: 10.1021/acs.accounts.8b00215. eprint: https://doi.org/10.1021/acs.accounts.8b00215.

[16] H. Chaté and B. Mahault. *Dry, aligning, dilute, active matter: A synthetic and self-contained overview.* 2019. arXiv: 1906.05542 [cond-mat.stat-mech].

[17] R. Golestanian, T. Liverpool, and A. Ajdari. "Designing phoretic micro-and nano-swimmers". In: *New Journal of Physics* 9.5 (2007), p. 126.

[18] R. Golestanian. "Anomalous diffusion of symmetric and asymmetric active colloids". In: *Physical review letters* 102.18 (2009), p. 188305.

[19] J. L. Moran and J. D. Posner. "Phoretic self-propulsion". In: *Annual Review of Fluid Mechanics* 49 (2017), pp. 511–540.

[20] Y. Wang, R. M. Hernandez, D. J. Bartlett, J. M. Bingham, T. R. Kline, A. Sen, and T. E. Mallouk. "Bipolar electrochemical mechanism for the propulsion of catalytic nanomotors in hydrogen peroxide solutions". In: *Langmuir* 22.25 (2006), pp. 10451–10456. DOI: https://doi.org/10.1021/la0615950.

[21] H. Su, C.-A. Hurd Price, L. Jing, Q. Tian, J. Liu, and K. Qian. "Janus particles: design, preparation, and biomedical applications". In: *Materials Today Bio* 4 (2019), p. 100033. DOI: https://doi.org/10.1016/j.mtbio.2019.100033.

[22] J. Katuri, X. Ma, M. M. Stanton, and S. Sánchez. "Designing micro-and nanoswimmers for specific applications". In: *Accounts of chemical research* 50.1 (2017), pp. 2–11.

[23] J. Wang. *Nanomachines: fundamentals and applications.* John Wiley & Sons, 2013.

[24] A. Ghosh, W. Xu, N. Gupta, and D. H. Gracias. "Active matter therapeutics". In: *Nano Today* 31 (2020), p. 100836. DOI: https://doi.org/10.1016/j.nantod.2019.100836.

[25] S. Saad and G. Natale. "Diffusiophoresis of active colloids in viscoelastic media". In: *Soft Matter* 15 (48 2019), pp. 9909–9919. DOI: 10.1039/C9SM01801H.

[26]   M. Schliwa and G. Woehlke. "Molecular motors". In: *Nature* 422.6933 (2003), pp. 759–765.

[27]   A. Doostmohammadi, M. F. Adamer, S. P. Thampi, and J. M. Yeomans. "Stabilization of active matter by flow-vortex lattices and defect ordering". In: *Nature communications* 7.1 (2016), pp. 1–9.

[28]   W.-C. Yang, C.-Y. Xia, H.-B. Zeng, and H.-Q. Zhang. "Phase separation and exotic vortex phases in a two-species holographic superfluid". In: *The European Physical Journal C* 81.1 (2021), pp. 1–9.

[29]   S. Shankar, A. Souslov, M. J. Bowick, M. C. Marchetti, and V. Vitelli. *Topological active matter*. 2021. arXiv: 2010.00364 [cond-mat.soft].

[30]   A. Amiri, R. Mueller, and A. Doostmohammadi. *Half-integer and full-integer topological defects in polar active matter: Emergence, crossover, and coexistence.* 2021. arXiv: 2106.03144 [cond-mat.soft].

[31]   K. Copenhagen, R. Alert, N. S. Wingreen, and J. W. Shaevitz. "Topological defects promote layer formation in Myxococcus xanthus colonies". In: *Nature Physics* 17.2 (2021), pp. 211–215.

[32]   T. Vicsek, A. Czirók, E. Ben-Jacob, I. Cohen, and O. Shochet. "Novel Type of Phase Transition in a System of Self-Driven Particles". In: *Phys. Rev. Lett.* 75 (6 Aug. 1995), pp. 1226–1229. DOI: 10.1103/PhysRevLett.75.1226.

[33]   D. Volfson, A. Kudrolli, and L. S. Tsimring. "Anisotropy-driven dynamics in vibrated granular rods". In: *Phys. Rev. E* 70 (5 Nov. 2004), p. 051312. DOI: 10.1103/PhysRevE.70.051312.

[34]   D. L. Blair, T. Neicu, and A. Kudrolli. "Vortices in vibrated granular rods". In: *Phys. Rev. E* 67 (3 Mar. 2003), p. 031303. DOI: 10.1103/PhysRevE.67.031303.

[35]   M. González-Pinto, F. Borondo, Y. Martínez-Ratón, and E. Velasco. "Clustering in vibrated monolayers of granular rods". In: *Soft Matter* 13 (14 2017), pp. 2571–2582. DOI: 10.1039/C7SM00102A.

[36]   R. Wittkowski and H. Löwen. "Dynamical density functional theory for colloidal particles with arbitrary shape". In: *Molecular Physics* 109.23-24 (2011), pp. 2935–2943.

[37]   B. V. Hokmabad, K. A. Baldwin, C. Krüger, C. Bahr, and C. C. Maass. "Topological Stabilization and Dynamics of Self-Propelling Nematic Shells". In: *Phys. Rev. Lett.* 123 (17 Oct. 2019), p. 178003. DOI: 10.1103/PhysRevLett.123.178003.

[38]   B. V. Hokmabad, R. Dey, M. Jalaal, D. Mohanty, M. Almukambetova, K. A. Baldwin, D. Lohse, and C. C. Maass. "Emergence of Bimodal Motility in Active Droplets". In: *Phys. Rev. X* 11 (1 Mar. 2021), p. 011043. DOI: 10.1103/PhysRevX.11.011043.

[39]   L. Abbaspour and S. Klumpp. "Enhanced diffusion of a tracer particle in a lattice model of a crowded active system". In: *Phys. Rev. E* 103 (5 Apr. 2021), p. 052601. DOI: 10.1103/PhysRevE.103.052601.

[40] J. R. Howse, R. A. L. Jones, A. J. Ryan, T. Gough, R. Vafabakhsh, and R. Golestanian. "Self-Motile Colloidal Particles: From Directed Propulsion to Random Walk". In: *Phys. Rev. Lett.* 99 (4 July 2007), p. 048102. DOI: 10.1103/PhysRevLett.99.048102.

[41] J.-P. Hansen and I. R. McDonald. *Theory of simple liquids.* Elsevier, 1990.

[42] S. Roorda, T. van Dillen, A. Polman, C. Graf, A. van Blaaderen, and B. J. Kooi. "Aligned gold nanorods in silica made by ion irradiation of core–shell colloidal particles". In: *Advanced Materials* 16.3 (2004), pp. 235–237.

[43] Y. Han, A. M. Alsayed, M. Nobili, J. Zhang, T. C. Lubensky, and A. G. Yodh. "Brownian motion of an ellipsoid". In: *Science* 314.5799 (2006), pp. 626–630.

[44] J. Tavares, B. Holder, and M. T. da Gama. "Structure and phase diagram of self-assembled rigid rods: Equilibrium polydispersity and nematic ordering in two dimensions". In: *Physical Review E* 79.2 (2009), p. 021505.

[45] M. Abkenar, K. Marx, T. Auth, and G. Gompper. "Collective behavior of penetrable self-propelled rods in two dimensions". In: *Phys. Rev. E* 88 (6 Dec. 2013), p. 062314. DOI: 10.1103/PhysRevE.88.062314.

[46] R. E. Isele-Holder, J. Elgeti, and G. Gompper. "Self-propelled worm-like filaments: spontaneous spiral formation structure and dynamics". In: *Soft Matter* 11 (36 2015), pp. 7181–7190. DOI: 10.1039/C5SM01683E.

[47] Ö. Duman, R. E. Isele-Holder, J. Elgeti, and G. Gompper. "Collective dynamics of self-propelled semiflexible filaments". In: *Soft Matter* 14 (22 2018), pp. 4483–4494. DOI: 10.1039/C8SM00282G.

[48] M. Doi, S. F. Edwards, and S. F. Edwards. *The theory of polymer dynamics.* Vol. 73. oxford university press, 1988.

[49] I. Sevonkaev, D. V. Goia, and E. Matijević. "Formation and structure of cubic particles of sodium magnesium fluoride (neighborite)". In: *Journal of colloid and interface science* 317.1 (2008), pp. 130–136.

[50] A. Haji-Akbari, M. Engel, A. S. Keys, X. Zheng, R. G. Petschek, P. Palffy-Muhoray, and S. C. Glotzer. "Disordered, quasicrystalline and crystalline phases of densely packed tetrahedra". In: *Nature* 462.7274 (2009), pp. 773–777.

[51] H. C. Andersen, J. D. Weeks, and D. Chandler. "Relationship between the hard-sphere fluid and fluids with realistic repulsive forces". In: *Physical Review A* 4.4 (1971), p. 1597.

[52] O. Bénichou, P. Illien, G. Oshanin, A. Sarracino, and R. Voituriez. "Tracer diffusion in crowded narrow channels". In: *Journal of Physics: Condensed Matter* 30.44 (2018), p. 443001.

[53] C. Mejia-Monasterio, S. Nechaev, G. Oshanin, and O. Vasilyev. "Tracer diffusion on a crowded random Manhattan lattice". In: *New Journal of Physics* 22.3 (2020), p. 033024.

[54] S. K. Ghosh, A. G. Cherstvy, and R. Metzler. "Non-universal tracer diffusion in crowded media of non-inert obstacles". In: *Physical Chemistry Chemical Physics* 17.3 (2015), pp. 1847–1858.

[55] A. Rabani, G. Ariel, and A. Be'er. "Collective motion of spherical bacteria". In: *PloS one* 8.12 (2013), e83760. DOI: https://doi.org/10.1371/journal.pone. 0083760.

[56] J. Toner and Y. Tu. "Flocks, herds, and schools: A quantitative theory of flocking". In: *Phys. Rev. E* 58 (4 Oct. 1998), pp. 4828–4858. DOI: 10.1103/ PhysRevE.58.4828.

[57] T. Vicsek and A. Zafeiris. "Collective motion". In: *Physics Reports* 517.3 (2012). Collective motion, pp. 71–140. DOI: https://doi.org/10.1016/j.physrep.2012.03. 004.

[58] J. Tailleur and M. E. Cates. "Statistical Mechanics of Interacting Run-and-Tumble Bacteria". In: *Phys. Rev. Lett.* 100 (21 Apr. 2008), p. 218103. DOI: 10.1103/PhysRevLett.100.218103.

[59] L. Caprini, U. Marini Bettolo Marconi, and A. Puglisi. "Spontaneous Velocity Alignment in Motility-Induced Phase Separation". In: *Phys. Rev. Lett.* 124 (7 Feb. 2020), p. 078001. DOI: 10.1103/PhysRevLett.124.078001.

[60] S. Henkes, K. Kostanjevec, J. M. Collinson, R. Sknepnek, and E. Bertin. "Dense active matter model of motion patterns in confluent cell monolayers". In: *Nature communications* 11.1 (2020), pp. 1–9.

[61] G. Szamel and E. Flenner. "Long-ranged velocity correlations in dense systems of self-propelled particles". In: *EPL (Europhysics Letters)* 133.6 (2021), p. 60002.

[62] H. H. Wensink, J. Dunkel, S. Heidenreich, K. Drescher, R. E. Goldstein, H. Löwen, and J. M. Yeomans. "Meso-scale turbulence in living fluids". In: *Proceedings of the National Academy of Sciences* 109.36 (2012), pp. 14308–14313. DOI: 10.1073/pnas.1202032109.

[63] R. J. Ellis. "Macromolecular crowding: obvious but underappreciated". In: *Trends in biochemical sciences* 26.10 (2001), pp. 597–604. DOI: https://doi.org/ 10.1016/S0968-0004(01)01938-7.

[64] J. A. Dix and A. Verkman. "Crowding Effects on Diffusion in Solutions and Cells". In: *Annual Review of Biophysics* 37.1 (2008), pp. 247–263. DOI: 10.1146/ annurev.biophys.37.032807.125824.

[65] C. Bechinger, R. Di Leonardo, H. Löwen, C. Reichhardt, G. Volpe, and G. Volpe. "Active particles in complex and crowded environments". In: *Rev. Mod. Phys.* 88 (4 Nov. 2016), p. 045006. DOI: 10.1103/RevModPhys.88.045006.

[66] S. Klumpp, W. Bode, and P. Puri. "Life in crowded conditions". In: *The European Physical Journal Special Topics* 227 (2019), pp. 2315–2328. DOI: 10.1140/epjst/e2018-800088-6.

[67] S. B. Zimmerman and A. P. Minton. "Macromolecular Crowding: Biochemical, Biophysical, and Physiological Consequences". In: *Annual Review of Biophysics and Biomolecular Structure* 22.1 (1993), pp. 27–65. DOI: 10.1146/annurev.bb.22. 060193.000331.

[68] L. Hall-Stoodley, J. W. Costerton, and P. Stoodley. "Bacterial biofilms: from the natural environment to infectious diseases". In: *Nature reviews microbiology* 2.2 (2004), pp. 95–108. DOI: 10.1038/nrmicro821.

[69] G. Salbreux and F. Jülicher. "Mechanics of active surfaces". In: *Phys. Rev. E* 96 (3 Sept. 2017), p. 032404. DOI: 10.1103/PhysRevE.96.032404.

[70] D. Mizuno, C. Tardin, C. F. Schmidt, and F. C. MacKintosh. "Nonequilibrium mechanics of active cytoskeletal networks". In: *Science* 315.5810 (2007), pp. 370–373. DOI: 10.1126/science.1134404.

[71] M. J. I. Muller, S. Klumpp, and R. Lipowsky. "Tug-of-war as a cooperative mechanism for bidirectional cargo transport by molecular motors". In: *Proceedings of the National Academy of Sciences* 105.12 (Mar. 2008), pp. 4609–4614. DOI: 10.1073/pnas.0706825105.

[72] C. B. Korn, S. Klumpp, R. Lipowsky, and U. S. Schwarz. "Stochastic simulations of cargo transport by processive molecular motors". In: *The Journal of Chemical Physics* 131.24 (2009), p. 245107. DOI: 10.1063/1.3279305. eprint: https://doi.org/10.1063/1.3279305.

[73] X. Zhao, K. K. Dey, S. Jeganathan, P. J. Butler, U. M. Córdova-Figueroa, and A. Sen. "Enhanced diffusion of passive tracers in active enzyme solutions". In: *Nano letters* 17.8 (2017), pp. 4807–4812.

[74] A. Sokolov and I. S. Aranson. "Physical Properties of Collective Motion in Suspensions of Bacteria". In: *Phys. Rev. Lett.* 109 (24 Nov. 2012), p. 248109. DOI: 10.1103/PhysRevLett.109.248109.

[75] J. Dunkel, S. Heidenreich, K. Drescher, H. H. Wensink, M. Bär, and R. E. Goldstein. "Fluid Dynamics of Bacterial Turbulence". In: *Phys. Rev. Lett.* 110 (22 Apr. 2013), p. 228102. DOI: 10.1103/PhysRevLett.110.228102.

[76] M. C. Konopka, K. A. Sochacki, B. P. Bratton, I. A. Shkel, M. T. Record, and J. C. Weisshaar. "Cytoplasmic protein mobility in osmotically stressed Escherichia coli". In: *Journal of bacteriology* 191.1 (2009), pp. 231–237.

[77] B. R. Parry, I. V. Surovtsev, M. T. Cabeen, C. S. O'Hern, E. R. Dufresne, and C. Jacobs-Wagner. "The bacterial cytoplasm has glass-like properties and is fluidized by metabolic activity". In: *Cell* 156.1-2 (2014), pp. 183–194.

[78] A. J. Boersma, I. S. Zuhorn, and B. Poolman. "A sensor for quantification of macromolecular crowding in living cells". In: *Nature methods* 12.3 (2015), p. 227.

[79] D. Gnutt, M. Gao, O. Brylski, M. Heyden, and S. Ebbinghaus. "Excluded-Volume Effects in Living Cells". In: *Angewandte Chemie International Edition* 54.8 (2015), pp. 2548–2551.

[80] D. L. Koch and J. F. Brady. "Anomalous diffusion in heterogeneous porous media". In: *The Physics of fluids* 31.5 (1988), pp. 965–973.

[81] S. K. Ghosh, A. G. Cherstvy, D. S. Grebenkov, and R. Metzler. "Anomalous, non-Gaussian tracer diffusion in crowded two-dimensional environments". In: *New Journal of Physics* 18.1 (Jan. 2016), p. 013027. DOI: 10.1088/1367-2630/18/1/013027.

[82] X.-L. Wu and A. Libchaber. "Particle Diffusion in a Quasi-Two-Dimensional Bacterial Bath". In: *Phys. Rev. Lett.* 84 (13 Mar. 2000), pp. 3017–3020. DOI: 10.1103/PhysRevLett.84.3017.

[83] G. Grégoire, H. Chaté, and Y. Tu. "Active and passive particles: Modeling beads in a bacterial bath". In: *Phys. Rev. E* 64 (1 June 2001), p. 011902. DOI: 10.1103/PhysRevE.64.011902.

[84] I. M. Zaid, J. Dunkel, and J. M. Yeomans. "Lévy fluctuations and mixing in dilute suspensions of algae and bacteria". In: *Journal of The Royal Society Interface* 8.62 (2011), pp. 1314–1331.

[85] C. Valeriani, M. Li, J. Novosel, J. Arlt, and D. Marenduzzo. "Colloids in a bacterial bath: simulations and experiments". In: *Soft Matter* 7 (11 2011), pp. 5228–5238. DOI: 10.1039/C1SM05260H.

[86] D. O. Pushkin and J. M. Yeomans. "Fluid Mixing by Curved Trajectories of Microswimmers". In: *Phys. Rev. Lett.* 111 (18 Oct. 2013), p. 188101. DOI: 10.1103/PhysRevLett.111.188101.

[87] R. Soto and R. Golestanian. "Run-and-tumble dynamics in a crowded environment: Persistent exclusion process for swimmers". In: *Phys. Rev. E* 89 (1 Jan. 2014), p. 012706. DOI: 10.1103/PhysRevE.89.012706.

[88] T. Kasyap, D. L. Koch, and M. Wu. "Hydrodynamic tracer diffusion in suspensions of swimming bacteria". In: *Physics of Fluids* 26.8 (2014), p. 081901. eprint: https://doi.org/10.1063/1.4891570.

[89] A. Morozov and D. Marenduzzo. "Enhanced diffusion of tracer particles in dilute bacterial suspensions". In: *Soft Matter* 10 (16 2014), pp. 2748–2758. DOI: 10.1039/C3SM52201F.

[90] Y. Yang and M. A. Bevan. "Cargo capture and transport by colloidal swarms". In: *Science Advances* 6.4 (2020). DOI: 10.1126/sciadv.aay7679.

[91] A. Caspi, R. Granek, and M. Elbaum. "Enhanced Diffusion in Active Intracellular Transport". In: *Phys. Rev. Lett.* 85 (26 Nov. 2000), pp. 5655–5658. DOI: 10.1103/PhysRevLett.85.5655.

[92] M. J. Kim and K. S. Breuer. "Enhanced diffusion due to motile bacteria". In: *Physics of Fluids* 16.9 (2004), pp. L78–L81. DOI: 10.1063/1.1787527. eprint: https://doi.org/10.1063/1.1787527.

[93] K. C. Leptos, J. S. Guasto, J. P. Gollub, A. I. Pesci, and R. E. Goldstein. "Dynamics of Enhanced Tracer Diffusion in Suspensions of Swimming Eukaryotic Microorganisms". In: *Phys. Rev. Lett.* 103 (19 Oct. 2009), p. 198103. DOI: 10.1103/PhysRevLett.103.198103.

[94] G. Miño, T. E. Mallouk, T. Darnige, M. Hoyos, J. Dauchet, J. Dunstan, R. Soto, Y. Wang, A. Rousselet, and E. Clement. "Enhanced Diffusion due to Active Swimmers at a Solid Surface". In: *Phys. Rev. Lett.* 106 (4 Jan. 2011), p. 048102. DOI: 10.1103/PhysRevLett.106.048102.

[95] G. Mino, J. Dunstan, A. Rousselet, E. Clément, and R. Soto. "Induced diffusion of tracers in a bacterial suspension: theory and experiments". In: *Journal of Fluid Mechanics* 729 (2013), pp. 423–444. DOI: 10.1017/jfm.2013.304.

[96] A. Jepson, V. A. Martinez, J. Schwarz-Linek, A. Morozov, and W. C. K. Poon. "Enhanced diffusion of nonswimmers in a three-dimensional bath of motile bacteria". In: *Phys. Rev. E* 88 (4 Oct. 2013), p. 041002. DOI: 10.1103/PhysRevE.88.041002.

[97] N. Koumakis, A. Lepore, C. Maggi, and R. Di Leonardo. "Targeted delivery of colloids by swimming bacteria". In: *Nature communications* 4.1 (2013), pp. 1–6. eprint: https://doi.org/10.1038/ncomms3588.

[98] L. Angelani, C. Maggi, M. L. Bernardini, A. Rizzo, and R. Di Leonardo. "Effective Interactions between Colloidal Particles Suspended in a Bath of Swimming Cells". In: *Phys. Rev. Lett.* 107 (13 Sept. 2011), p. 138302. DOI: 10.1103/PhysRevLett.107.138302.

[99] E. W. Burkholder and J. F. Brady. "Tracer diffusion in active suspensions". In: *Phys. Rev. E* 95 (5 May 2017), p. 052605. DOI: 10.1103/PhysRevE.95.052605.

[100] J. T. Siebert, F. Dittrich, F. Schmid, K. Binder, T. Speck, and P. Virnau. "Critical behavior of active Brownian particles". In: *Physical Review E* 98.3 (2018), p. 030601.

[101] S. Whitelam, K. Klymko, and D. Mandal. "Phase separation and large deviations of lattice active matter". In: *The Journal of chemical physics* 148.15 (2018), p. 154902.

[102] S. Darjani, J. Koplik, S. Banerjee, and V. Pauchard. "Liquid-hexatic-solid phase transition of a hard-core lattice gas with third neighbor exclusion". In: *The Journal of chemical physics* 151.10 (2019), p. 104702.

[103] B. Partridge and C. F. Lee. "Critical Motility-Induced Phase Separation Belongs to the Ising Universality Class". In: *Phys. Rev. Lett.* 123 (6 Aug. 2019), p. 068002. DOI: 10.1103/PhysRevLett.123.068002.

[104] O. M. Braun and C. A. Sholl. "Diffusion in generalized lattice-gas models". In: *Phys. Rev. B* 58 (22 Dec. 1998), pp. 14870–14879. DOI: 10.1103/PhysRevB.58. 14870.

[105] V. Ramasubramani, B. D. Dice, E. S. Harper, M. P. Spellings, J. A. Anderson, and S. C. Glotzer. "freud: A Software Suite for High Throughput Analysis of Particle Simulation Data". In: *Computer Physics Communications* 254 (2020), p. 107275. DOI: https://doi.org/10.1016/j.cpc.2020.107275.

[106] A. Mozaffari, N. Sharifi-Mood, J. Koplik, and C. Maldarelli. "Self-propelled colloidal particle near a planar wall: A Brownian dynamics study". In: *Physical Review Fluids* 3.1 (2018), p. 014104.

[107] K. Schaar, A. Zöttl, and H. Stark. "Detention Times of Microswimmers Close to Surfaces: Influence of Hydrodynamic Interactions and Noise". In: *Phys. Rev. Lett.* 115 (3 July 2015), p. 038101. DOI: 10.1103/PhysRevLett.115.038101.

[108] A. Mozaffari, N. Sharifi-Mood, J. Koplik, and C. Maldarelli. "Self-diffusiophoretic colloidal propulsion near a solid boundary". In: *Physics of Fluids* 28.5 (2016), p. 053107.

[109] A. Zöttl and H. Stark. "Emergent behavior in active colloids". In: *Journal of Physics: Condensed Matter* 28.25 (2016), p. 253001.

[110] J. K. Parrish and W. M. Hamner. *Animal groups in three dimensions: how species aggregate.* Cambridge University Press, 1997.

[111] N. D. Mermin and H. Wagner. "Absence of Ferromagnetism or Antiferromagnetism in One- or Two-Dimensional Isotropic Heisenberg Models". In: *Phys. Rev. Lett.* 17 (22 Nov. 1966), pp. 1133–1136. DOI: 10.1103/PhysRevLett.17.1133.

[112] P. C. Hohenberg. "Existence of Long-Range Order in One and Two Dimensions". In: *Phys. Rev.* 158 (2 June 1967), pp. 383–386. DOI: 10.1103/PhysRev.158.383.

[113] G. Gonnella, D. Marenduzzo, A. Suma, and A. Tiribocchi. "Motility-induced phase separation and coarsening in active matter". In: *Comptes Rendus Physique* 16.3 (2015). Coarsening dynamics / Dynamique de coarsening, pp. 316–331. DOI: https://doi.org/10.1016/j.crhy.2015.05.001.

[114] L. Caprini and U. Marini Bettolo Marconi. "Spatial velocity correlations in inertial systems of active Brownian particles". In: *Soft Matter* 17 (15 2021), pp. 4109–4121. DOI: 10.1039/D0SM02273J.

[115] S. Dikshit and S. Mishra. *Activity Driven Phase Separation and Ordering Kinetics of Passive Particles*. 2021. arXiv: 2108.08921 [cond-mat.soft].

[116] R. Mandal, P. J. Bhuyan, M. Rao, and C. Dasgupta. "Active fluidization in dense glassy systems". In: *Soft Matter* 12 (29 2016), pp. 6268–6276. DOI: 10.1039/C5SM02950C.

[117] R. Ni, M. A. Cohen Stuart, and P. G. Bolhuis. "Tunable Long Range Forces Mediated by Self-Propelled Colloidal Hard Spheres". In: *Phys. Rev. Lett.* 114 (1 Jan. 2015), p. 018302. DOI: 10.1103/PhysRevLett.114.018302.

[118] H. Tanaka, A. A. Lee, and M. P. Brenner. "Hot particles attract in a cold bath". In: *Phys. Rev. Fluids* 2 (4 Apr. 2017), p. 043103. DOI: 10.1103/PhysRevFluids.2.043103.

[119] R. Ni, M. A. Cohen Stuart, M. Dijkstra, and P. G. Bolhuis. "Crystallizing hard-sphere glasses by doping with active particles". In: *Soft Matter* 10 (35 2014), pp. 6609–6613. DOI: 10.1039/C4SM01015A.

[120] F. Kümmel, P. Shabestari, C. Lozano, G. Volpe, and C. Bechinger. "Formation, compression and surface melting of colloidal clusters by active particles". In: *Soft Matter* 11 (31 2015), pp. 6187–6191. DOI: 10.1039/C5SM00827A.

[121] D. F. Hinz, A. Panchenko, T.-Y. Kim, and E. Fried. "Motility versus fluctuations in mixtures of self-motile and passive agents". In: *Soft Matter* 10 (45 2014), pp. 9082–9089. DOI: 10.1039/C4SM01562B.

[122] J. P. Banerjee, R. Mandal, D. S. Banerjee, S. Thutupalli, and M. Rao. *Active ploughing through a compressible viscoelastic fluid: Unjamming and emergent nonreciprocity*. 2021. arXiv: 2109.10438 [cond-mat.soft].

[123] S. Nilsson and G. Volpe. "Metastable clusters and channels formed by active particles with aligning interactions". In: *New Journal of Physics* 19.11 (Nov. 2017), p. 115008. DOI: 10.1088/1367-2630/aa9516.

[124] J. M. Moore, T. N. Thompson, M. A. Glaser, and M. D. Betterton. "Collective motion of driven semiflexible filaments tuned by soft repulsion and stiffness". In: *Soft Matter* 16 (41 2020), pp. 9436–9442. DOI: 10.1039/D0SM01036G.

[125] A. Joshi, E. Putzig, A. Baskaran, and M. F. Hagan. "The interplay between activity and filament flexibility determines the emergent properties of active nematics". In: *Soft Matter* 15.1 (2019), pp. 94–101. DOI: 10.1039/C8SM02202J.

[126] M. Bär, R. Großmann, S. Heidenreich, and F. Peruani. "Self-Propelled Rods: Insights and Perspectives for Active Matter". In: *Annual Review of Condensed Matter Physics* 11.1 (2020), pp. 441–466. DOI: 10.1146/annurev-conmatphys-031119-050611.

[127] K. R. Prathyusha, S. Henkes, and R. Sknepnek. "Dynamically generated patterns in dense suspensions of active filaments". In: *Phys. Rev. E* 97 (2 Feb. 2018), p. 022606. DOI: 10.1103/PhysRevE.97.022606.

[128] X.-q. Shi and H. Chaté. *Self-Propelled Rods: Linking Alignment-Dominated and Repulsion-Dominated Active Matter*. 2018. arXiv: 1807.00294 [cond-mat.soft].

[129] Y.-K. Wang, C.-J. Lo, and W.-C. Lo. "Formation of spiral coils among self-propelled chains". In: *Phys. Rev. E* 98 (6 Dec. 2018), p. 062613. DOI: 10.1103/PhysRevE.98.062613.

[130] R. Großmann, F. Peruani, and M. Bär. "Mesoscale pattern formation of self-propelled rods with velocity reversal". In: *Phys. Rev. E* 94 (5 Nov. 2016), p. 050602. DOI: 10.1103/PhysRevE.94.050602.

[131] S. Weitz, A. Deutsch, and F. Peruani. "Self-propelled rods exhibit a phase-separated state characterized by the presence of active stresses and the ejection of polar clusters". In: *Phys. Rev. E* 92 (1 July 2015), p. 012322. DOI: 10.1103/PhysRevE.92.012322.

[132] R. Balagam and O. A. Igoshin. "Mechanism for collective cell alignment in Myxococcus xanthus bacteria". In: *PLoS computational biology* 11.8 (2015), e1004474. DOI: https://doi.org/10.1371/journal.pcbi.1004474.

[133] H. H. Wensink and H. Löwen. "Emergent states in dense systems of active rods: from swarming to turbulence". In: *Journal of Physics: Condensed Matter* 24.46 (Oct. 2012), p. 464130. DOI: 10.1088/0953-8984/24/46/464130.

[134] H. H. Wensink and H. Löwen. "Aggregation of self-propelled colloidal rods near confining walls". In: *Phys. Rev. E* 78 (3 Sept. 2008), p. 031409. DOI: 10.1103/PhysRevE.78.031409.

[135] U. Börner, A. Deutsch, H. Reichenbach, and M. Bär. "Rippling Patterns in Aggregates of Myxobacteria Arise from Cell-Cell Collisions". In: *Phys. Rev. Lett.* 89 (7 July 2002), p. 078101. DOI: 10.1103/PhysRevLett.89.078101.

[136] Y. Sumino, K. H. Nagai, Y. Shitaka, D. Tanaka, K. Yoshikawa, H. Chaté, and K. Oiwa. "Large-scale vortex lattice emerging from collectively moving microtubules". In: *Nature* 483.7390 (2012), pp. 448–452. DOI: https://doi.org/10.1038/nature10874.

[137] F. Peruani, J. Starruß, V. Jakovljevic, L. Søgaard-Andersen, A. Deutsch, and M. Bär. "Collective Motion and Nonequilibrium Cluster Formation in Colonies of Gliding Bacteria". In: *Phys. Rev. Lett.* 108 (9 Feb. 2012), p. 098102. DOI: 10.1103/PhysRevLett.108.098102.

[138] A. Be'er, S. K. Strain, R. A. Hernández, E. Ben-Jacob, and E.-L. Florin. "Periodic Reversals in Paenibacillus dendritiformis Swarming". In: *Journal of Bacteriology* 195.12 (2013), pp. 2709–2717. DOI: 10.1128/JB.00080-13.

[139] D. Nishiguchi, K. H. Nagai, H. Chaté, and M. Sano. "Long-range nematic order and anomalous fluctuations in suspensions of swimming filamentous bacteria". In: *Phys. Rev. E* 95 (2 Feb. 2017), p. 020601. DOI: 10.1103/PhysRevE.95.020601.

[140] L. Huber, R. Suzuki, T. Krüger, E. Frey, and A. Bausch. "Emergence of coexisting ordered states in active matter systems". In: *Science* 361.6399 (2018), pp. 255–258. DOI: 10.1126/science.aao5434.

[141] T. Mirfakhrai, J. D. Madden, and R. H. Baughman. "Polymer artificial muscles". In: *Materials Today* 10.4 (2007), pp. 30–38. DOI: https://doi.org/10.1016/S1369-7021(07)70048-2.

[142] L. Turner, W. S. Ryu, and H. C. Berg. "Real-Time Imaging of Fluorescent Flagellar Filaments". In: *Journal of Bacteriology* 182.10 (2000), pp. 2793–2801. DOI: 10.1128/JB.182.10.2793-2801.2000.

[143] R. Großmann, F. Peruani, and M. Bär. "Diffusion properties of active particles with directional reversal". In: *New Journal of Physics* 18.4 (Apr. 2016), p. 043009. DOI: 10.1088/1367-2630/18/4/043009.

[144] I. Santra, U. Basu, and S. Sabhapandit. "Active Brownian motion with directional reversals". In: *Phys. Rev. E* 104 (1 July 2021), p. L012601. DOI: 10.1103/PhysRevE.104.L012601.

[145] Z. Zhang, O. A. Igoshin, C. R. Cotter, and L. J. Shimkets. "Agent-based modeling reveals possible mechanisms for observed aggregation cell behaviors". In: *Biophysical journal* 115.12 (2018), pp. 2499–2511. DOI: https://dx.doi.org/10.1016\%2Fj.bpj.2018.11.005.

[146] C. Kurzthaler, S. Mandal, T. Bhattacharjee, H. Löwen, S. S. Datta, and H. A. Stone. "A geometric criterion for the optimal spreading of active polymers in porous media". In: *Nature Communications* 12.1 (2021), pp. 1–10. DOI: https://doi.org/10.1038/s41467-021-26942-0.

[147] M. J. McBride. "Bacterial gliding motility: multiple mechanisms for cell movement over surfaces". In: *Annual Reviews in Microbiology* 55.1 (2001), pp. 49–75. DOI: https://doi.org/10.1146/annurev.micro.55.1.49.

[148] D. Tam and A. E. Hosoi. "Optimal feeding and swimming gaits of biflagellated organisms". In: *Proceedings of the National Academy of Sciences* 108.3 (Jan. 2011), pp. 1001–1006. DOI: 10.1073/pnas.1011185108.

[149] J. Taktikos, H. Stark, and V. Zaburdaev. "How the motility pattern of bacteria affects their dispersal and chemotaxis". In: *PloS one* 8.12 (2013), e81936.

[150] D.-P. Häder and U. Burkart. "Enhanced model for photophobic responses of the blue-green alga, Phormidium uncinatum". In: *Plant and cell physiology* 23.8 (1982), pp. 1391–1400.

[151] D. Häder. "Photosensory behavior in procaryotes". In: *Microbiological reviews* 51.1 (1987), pp. 1–21.

[152] C. Tamulonis, M. Postma, and J. Kaandorp. "Modeling filamentous cyanobacteria reveals the advantages of long and fast trichomes for optimizing light exposure". In: *PLoS One* 6.7 (2011), e22084. DOI: https://doi.org/10.1371/journal.pone.0022084.

[153] J. A. Anderson, J. Glaser, and S. C. Glotzer. "HOOMD-blue: A Python package for high-performance molecular dynamics and hard particle Monte Carlo simulations". In: *Computational Materials Science* 173 (2020), p. 109363. DOI: https://doi.org/10.1016/j.commatsci.2019.109363.

[154] K. Sekimoto, N. Mori, K. Tawada, and Y. Y. Toyoshima. "Symmetry Breaking Instabilities of an In Vitro Biological System". In: *Phys. Rev. Lett.* 75 (1 July 1995), pp. 172–175. DOI: 10.1103/PhysRevLett.75.172.

[155] R. G. Winkler, J. Elgeti, and G. Gompper. "Active Polymers — Emergent Conformational and Dynamical Properties: A Brief Review". In: *Journal of the Physical Society of Japan* 86.10 (2017), p. 101014. DOI: 10.7566/JPSJ.86.101014. eprint: https://doi.org/10.7566/JPSJ.86.101014.

[156] R. W. Style, R. Boltyanskiy, G. K. German, C. Hyland, C. W. MacMinn, A. F. Mertz, L. A. Wilen, Y. Xu, and E. R. Dufresne. "Traction force microscopy in physics and biology". In: *Soft matter* 10.23 (2014), pp. 4047–4055. DOI: https://doi.org/10.1039/C4SM00264D.

[157] F. J. Giessibl. "Advances in atomic force microscopy". In: *Rev. Mod. Phys.* 75 (3 July 2003), pp. 949–983. DOI: 10.1103/RevModPhys.75.949.

[158] A. S. Utada, E. Lorenceau, D. R. Link, P. D. Kaplan, H. A. Stone, and D. A. Weitz. "Monodisperse Double Emulsions Generated from a Microcapillary Device". In: *Science* 308.5721 (2005), pp. 537–541. DOI: 10.1126/science.1109164. eprint: https://www.science.org/doi/pdf/10.1126/science.1109164.

[159] I. Elishakoff. "A closed-form solution for the generalized Euler problem". In: *Proc. R. Soc. Lond. A* 456.2002 (2000), pp. 2409–2417. DOI: 10.1098/rspa.2000.0618.

[160] T. Fujii. "PDMS-based microfluidic devices for biomedical applications". In: *Microelectronic Engineering* 61-62 (2002). Micro- and Nano-Engineering 2001, pp. 907–914. DOI: https://doi.org/10.1016/S0167-9317(02)00494-X.

[161] H. Coupin. "Some remarks on the locomotion of the Oscillaries". In: *CR Acad. Sci* 176 (1923), pp. 1491–1493.

[162] P. R. Burkholder. "Movement in the Cyanophyceae". In: *The Quarterly Review of Biology* 9.4 (1934), pp. 438–459.

[163] K. H. Keller, M. Grady, and M. Dworkin. "Surface tension gradients: feasible model for gliding motility of Myxococcus xanthus". In: *Journal of Bacteriology* 155.3 (1983), pp. 1358–1366. DOI: 10.1128/jb.155.3.1358-1366.1983. eprint: https://journals.asm.org/doi/pdf/10.1128/jb.155.3.1358-1366.1983.

[164] M. Dworkin, K. Keller, and D. Weisberg. "Experimental observations consistent with a surface tension model of gliding motility of Myxococcus xanthus". In: *Journal of bacteriology* 155.3 (1983), pp. 1367–1371.

[165] C. Wolgemuth, E. Hoiczyk, D. Kaiser, and G. Oster. "How Myxobacteria Glide". In: *Current Biology* 12.5 (2002), pp. 369–377. DOI: https://doi.org/10.1016/S0960-9822(02)00716-9.

[166] S. E. Spagnolie and E. Lauga. "Jet propulsion without inertia". In: *Physics of Fluids* 22.8 (2010), p. 369.

[167]   A. Ducret, M.-P. Valignat, F. Mouhamar, T. Mignot, and O. Theodoly. "Wet-surface–enhanced ellipsometric contrast microscopy identifies slime as a major adhesion factor during bacterial surface motility". In: *Proceedings of the National Academy of Sciences* 109.25 (2012), pp. 10036–10041. DOI: 10.1073/pnas.1120979109. eprint: https://www.pnas.org/content/109/25/10036.full.pdf.

[168]   K. M. Ehlers, A. Samuel, H. C. Berg, and R. Montgomery. "Do cyanobacteria swim using traveling surface waves?" In: *Proceedings of the National Academy of Sciences* 93.16 (1996), pp. 8340–8343.

[169]   R. O'Brien. "The gliding motion of a bacterium: Flexibacter strain BH3". In: *The ANZIAM Journal* 23.1 (1981), pp. 2–16.

[170]   A. Siddiqui, R. Burchard, and W. Schwarz. "An undulating surface model for the motility of bacteria gliding on a layer of non-Newtonian slime". In: *International Journal of Non-Linear Mechanics* 36.5 (2001), pp. 743–761. DOI: https://doi.org/10.1016/S0020-7462(00)00028-7.

[171]   Y. Wang, T. Hayat, and A. M. Siddiqui. "Gliding motion of bacteria on power-law slime". In: *Mathematical methods in the applied sciences* 28.3 (2005), pp. 329–347.

[172]   N. Ali, Z. Asghar, O. A. Bég, and M. Sajid. "Bacterial gliding fluid dynamics on a layer of non-Newtonian slime: Perturbation and numerical study". In: *Journal of theoretical biology* 397 (2016), pp. 22–32.

[173]   J. Tchoufag, P. Ghosh, C. B. Pogue, B. Nan, and K. K. Mandadapu. "Mechanisms for bacterial gliding motility on soft substrates". In: *Proceedings of the National Academy of Sciences* 116.50 (2019), pp. 25087–25096.

[174]   R. Balagam, D. B. Litwin, F. Czerwinski, M. Sun, H. B. Kaplan, J. W. Shaevitz, and O. A. Igoshin. "Myxococcus xanthus gliding motors are elastically coupled to the substrate as predicted by the focal adhesion model of gliding motility". In: *PLoS computational biology* 10.5 (2014), e1003619.

[175]   W. Nultsch. "THE INFLUENCE OF LIGHT ON THE MOVEMENT OF THE CYANOPHYCEEN: III. Communication: PHOTOPHOBOTAXIS OF PHORMIDIUM UNCINATUM". In: *Planta* 58.6. H (1962), pp. 647–663.

[176]   W. Nultsch, H. Schuchart, and M. Höhl. "Investigations on the phototactic orientation of Anabaena variabilis". In: *Archives of Microbiology* 122.1 (1979), pp. 85–91.

[177]   S. Ramaswamy, R. A. Simha, and J. Toner. "Active nematics on a substrate: Giant number fluctuations and long-time tails". In: *Europhysics Letters (EPL)* 62.2 (Apr. 2003), pp. 196–202. DOI: 10.1209/epl/i2003-00346-7.

[178]   A. Doostmohammadi, J. Ignés-Mullol, J. M. Yeomans, and F. Sagués. "Active nematics". In: *Nature communications* 9.1 (2018), pp. 1–13.

[179]   T. Sanchez, D. T. Chen, S. J. DeCamp, M. Heymann, and Z. Dogic. "Spontaneous motion in hierarchically assembled active matter". In: *Nature* 491.7424 (2012), pp. 431–434.

[180]   M. Mijalkov, A. McDaniel, J. Wehr, and G. Volpe. "Engineering Sensorial Delay to Control Phototaxis and Emergent Collective Behaviors". In: *Phys. Rev. X* 6 (1 Jan. 2016), p. 011008. DOI: 10.1103/PhysRevX.6.011008.

Acknowledgements

I am extremely grateful to the Max Planck School Matter to Life for giving me the opportunity to pursue my Ph.D.

I would like to express my deepest gratitude to my supervisor Prof. Dr. Stefan Klumpp for his noble guidance, support with full encouragement, and enthusiasm. This would not have been possible without your guidance, which enabled me to develop an understanding of the subject. Your advice for both my research and my career has been invaluable.

I would like to extend my sincere thanks to my thesis committee members, Prof. Dr . Ramin Golestanian and Prof. Dr. Marcus Müller, for your encouraging words and insightful comments and suggestions. I am very thankful to the members of my defense committee, for accepting to be in my examination board, and special thanks to Prof. Dr. Ramin Golestanian for reviewing my thesis.

I would like to offer my special thanks to Dr. Stefan Karpitschka, the meetings and conversations had inspired me to think deeply and sparked my interest, motivation, and enthusiasm.

I would like to express my sincere gratitude to all of my collages and groupmates. In particular to my dearest friend Dr. Rituparno Mandal for the all constructive discussions and scientific inputs. I appreciate Babak Vajdi for his suggestions and comments.

I would like to extend my heartfelt thanks to all of my incredible friends who have

provided me with many wonderful memories during my doctoral studies.

Most importantly, I am indebted to my family's unconditional, unequivocal, and loving support. I wish I could have all of you on my side during this chapter of my life. Amir, thanks for being my best friend and mate for life.